The Dissertation Committee for Alma Delia Castaneda Certifies that this is the approved version of the following dissertation:

Detection of microRNA by Electrocatalytically Amplified Nanoparticle Collisions

Committee:

Richard M. Crooks, Supervisor

Jason B. Shear

Livia Schiavinato Eberlin

Lauren J. Webb

David W. Hoffman

Detection of microRNA by Electrocatalytically Amplified Nanoparticle Collisions

by

Alma Delia Castaneda, B.S. Chemistry

Dissertation

Presented to the Faculty of the Graduate School of

The University of Texas at Austin

in Partial Fulfillment

of the Requirements

for the Degree of

Doctor of Philosophy

The University of Texas at Austin

May 2017

Dedication

This dissertation is dedicated to my family. To my father, J. Dolores Castañeda, who taught me that nothing worth having comes easy. To my mother, Maria Guadalupe Castañeda, mi mejor amiga en todo el mundo, te agradezco todo tu apoyo y tu paciencia. To my brother, Jose Dolores Castañeda, my partner-in-crime during all-nighters and impromptu pho trips. To my fiancé, Jairo Andres Zapata: my inspiration, my rock, my shining star. Thank you for all of your love and support throughout this incredible journey.

In loving memory of Paul DeGregory. You are missed, my friend.

Acknowledgements

I would like to thank my advisor, Richard M. Crooks, for all of the guidance and mentoring throughout these past few years. You have cultivated my growth as a scientist, and for that, I am forever grateful. I would also like to thank my collaborators, Allen J. Bard, Bo Zhang, and Keith J. Stevenson, as well as my co-workers on this project, Timothy Alligrant and Donald Robinson. Thank you to my lovely colleagues: Nevena, Eunsoo, Aliya, Morgan, Xiang, Nick, Jim, Stephen. Thank you to my coffee buddy, Molly. Finally, thank you to my dear girls who always offered kind words and encouragement: Candice, Lynne, Alice, Ashley.

Detection of microRNA by Electrocatalytically Amplified Nanoparticle Collisions

Alma Delia Castaneda, Ph. D.

The University of Texas at Austin, 2017

Supervisor: Richard M. Crooks

We report a new and general approach that will be useful for adapting the method of electrocatalytic amplification (ECA) to biosensing applications. In ECA, individual collisions of catalytic nanoparticles with a noncatalytic electrode surface lead to bursts of current. In this dissertation, the current arises from catalytic electrooxidation of N_2H_4 at the surface of platinum nanoparticles (PtNPs). As described in Chapter 1, the problem with using ECA for biosensing applications heretofore, is that it is necessary to immobilize a receptor, such as DNA (as in the case here) or an antibody on the PtNP surface. This inactivates the colliding NP, however, and leads to very small collision signatures. In this work, we show that oligonucleotides bound on the PtNP surface can be detected using ECA following enzymatic digestion.

Chapter 2 demonstrates the proof-of-concept of this general approach using ssDNA-modified PtNPs and Exonuclease

I (Exo I), an enzyme specific to ssDNA. After PtNPs were passivated with ssDNA, we show that the presence of this DNA can be detected by selectively removing a fraction via enzymatic cleavage. About half of the electrocatalytic current is recovered from the PtNPs on both Au and Hg microelectrodes.

In Chapter 3, we show the application of this enzyme approach for the specific detection of microRNA (miRNA). The targets are miRNA-203 and miRNA-21, miRNAs of interest for cancer biomarker detection. PtNPs were modified with ssDNA complementary to the target, incubated with the miRNA, and the ssDNA was cleaved by Duplex Specific Nuclease (DSN). This exposes the PtNP surface for ECA, and the signal frequency is correlated to concentration of miRNA.

Chapter 4 introduces a technique whereby ECA signals are manipulated via electrostatic interactions by modifying the surface of Au microelectrodes with polyelectrolyte multilayer films (PEMs). We demonstrate that it is possible to control the frequency of the collisions by manipulating the net electrostatic charge on the outer surface of the PEM film, and that electrons are able to tunnel from the PtNPs to the electrode through films of thicknesses up to 5 nm. These results set the stage for future sensing applications.

Table of Contents

List of Tables xi

List of Figures xii

List of Illustrations xxix

Chapter 1: Introduction 1

1.1 Electrochemical Detection of Particle Collisions 1

1.2 Electrocatalytic Amplification of Nanoparticle Collisions 2

1.3 Developments in Mass Transport of Particles .. 5

1.4 Electrode Materials 8

1.5 Fundamental Studies of Metallic Nanoparticle Impacts 11

1.6 Electrochemical Detection of Soft Particles . 13

1.7 Detection of Biological Targets 14

1.8 ECA Sensors for DNA Detection 16

1.9 DNA Surface Modification Studies of ECA 18

1.10 Research Summary and Dissertation Overview . 20

1.11 Accomplishments 22

Chapter 2: Electrocatalytic amplification of DNA-modified nanoparticle collisions via enzymatic digestion . 23

Introduction 23

Experimental 27

Chemicals and Materials 27

Synthesis and Characterization of PtNPs 28

Preparation of PtNP@ssDNA Conjugates 30

Enzymatic Digestion of PtNP@ssDNA 31

UME Preparation 31
Electrochemistry 32
Nanoparticle Tracking Analysis 33
Results and Discussion 33
Synthesis and Characterzation of PtNP@ssDNA . 33
ECA of PtNP@ssDNA at Au UMEs prior to Exo I Digestion 38
Colloidal Stability during Enzymatic Reactions42
ECA of PtNP@ssDNA at Au UMEs after Exo I Digestion 45
ECA of PtNP@ssDNA at Hg UMEs 50
Summary and Conclusions 54
Chapter 3: Detection of microRNA by Electrocatalytic Amplification 57
Introduction 57
Experimental 62
Chemicals and Materials 62
Synthesis and Characterization of PtNPs 64
Preparation of PtNP@ssDNA:miRNA Conjugates .. 65
DSN Cleavage of the PtNP@ssDNA:miRNA Conjugates66
Fluorescence Analysis 66
UME Preparation 67
Electrochemistry 67
Nanoparticle Tracking Analysis 68
Results and Discussion 69
Synthesis and Characterzation of PtNP@ssDNA and PtNP@ssDNA:miRNA 69
Fluorescence Detection of miRNA-203 74
ECA Analysis on Au UMEs 75
ECA Analysis on Au/Hg UMEs 79

Detection of miRNA-21 85
Summary and Conclusions 87
Chapter 4: Electrocatalytic Amplification of Nanoparticle Collisions at Electrodes Modified with Polyelectrolyte Multilayer Films 90
Introduction 90
Experimental 93
Chemicals and Materials 93
Synthesis of PtNPs 94
Electrode Modification with MUA 96
LbL Deposition of PEM Films 97
Electrochemistry 97
Results and Discussion 98
UME Modification 98
SAM-Modified Au UMEs 99
Characterization of PEM Films 104
PtNP Collisions at pLL-Modified Au UMEs 106
PtNP Collisions at MUA-pLL-pGA-Modified Au UMEs 116
PtNP Collisions at pLL-pGA-pLL-Modified Au UMEs 120
Summary and Conclusions 124
Chapter 5: Conclusions and Outlook 126
References 128

List of Tables

Table 2.1: Naked PtNP and PtNP@ssDNA sizes in Taq buffer and Taq buffer components 45

Table 2.2: Collision frequency of post-Exo I PtNP@ssDNA conjugates at Au and Hg UMEs as a function of concentration 54

List of Figures

Figure 2.1: Analysis of PtNPs by transmission electron microscopy. (a) Representative TEM micrograph of the PtNPs used in this study and (b) Histogram indicating the size of the PtNPs: 22 ± 4 nm.29

Figure 2.2: Fluorescence calibration curve used to determine the coverage of ssDNA for the PtNP@ssDNA materials. The DNA coverage per PtNP was estimated to be ~35 DNAs per PtNP. This value applies to all experiments discussed in the main text except those associated with **Figure 2.4**. 35

Figure 2.3: Representative size-distribution histograms, derived from nanoparticle tracking analysis, for the PtNPs used in this study. The types of PtNPs corresponding to each histogram are shown in the legend. The concentrations of PtNPs were: naked PtNPs, 0.57 pM; PtNP@ssDNA, 0.89 pM; and PtNP@ssDNA post-Exo I, 0.46 pM. Measurements were obtained in (a) 50 mM phosphate buffer (PB, pH 7), (b) 50 mM PB (pH 7) + 10 mM N_2H_4, and (c) Taq buffer. To account for the differences in NP concentration, the histograms are normalized to the highest concentration observed for each species. 37

Figure 2.4: ECA results obtained using a Au UME and a solution containing 50 mM PB (pH 7) + 10.0 mM N_2H_4. (a) *i-t* curves obtained at E = −50.0 mV. The types of PtNPs used for each trace are shown in the legend. (b) Histogram showing the distribution of collision currents for the indicated ratios of PtNP:ssDNA. In all cases the indicated ratios refer to the PtNP:ssDNA ratio of the solution used to modify the PtNPs (not the actual surface concentrations of ssDNA on the PtNPs). 40

Figure 2.5: ECA results for collisions of naked PtNPs with an Au UME. The solutions contained 50 mM PB + 10 mM N_2H_4 (pH 7). (a) *i-t* traces in the absence (black trace) and presence (colored traces) of 11.7 pM PtNPs. The average collision frequency for the three trials was 0.048 ± 0.006 Hz. (b) Histogram showing the frequency of collisions as a function of current. The average collision current was 51 ± 41 pA. 41

Figure 2.6: Nanoparticle tracking analysis showing the normalized concentration of PtNPs as a function of their diameter for naked PtNPs (black traces) and PtNP@ssDNA (red traces) in (a) Taq buffer, (b) 20 mM $(NH_4)_2SO_4$, (c) 2.0 mM $MgCl_2$, (d) 75 mM Tris-HCl (pH 8.8), and (e) 0.01% Tween 20. (f) Histogram showing the average PtNP diameter in Taq buffer and the individual buffer components. 44

Figure 2.7: (a) *i-t* curves obtained at E = −50.0 mV for 11.7 pM PtNP@ssDNA before (black) and after (red) ssDNA digestion by Exo I. The inset shows an expanded view of the *i-t* trace before treatment with Exo I. (b) Expanded view of post-Exo I trace in frame a showing the step-shaped profile. (c) Histogram showing the distribution of currents for collisions of PtNP@ssDNA post-Exo I.(d) Plot of collision frequency as a function of the concentration of PtNP@ssDNA post-Exo I. 47

Figure 2.8: ECA results for collisions of PtNP@ssDNA modified with the thiol linkage on the 3’ end, post-Exo I digestion on Au (a) and Hg (b) UMEs. The solutions contained 50 mM PB + 10 mM N_2H_4 (pH 7). *i-t* traces in the absence (black traces) and presence (red traces) of 4 pM PtNPs@ssDNA, post-Exo I. No significant collision events were observed for either electrode material. 49

Figure 2.9: (a) *i-t* curves obtained at E = 5.0 mV for 1.17 pM PtNP@ssDNA before (black) and after (red) digestion by Exo I. The inset shows an expanded view of the i-t trace before treatment with Exo I. (b) Expanded view of post-Exo I trace in frame a showing the spike-shaped profile. (c) Histogram showing the distribution of charges for collisions of PtNP@ssDNA post-Exo I (d) Plot of collision frequency as a function of the concentration of PtNP@ssDNA post-Exo I.52

Figure 3.1: Transmission electron microscopy of PtNPs. (a) Representative TEM micrograph of the PtNPs used for the experiments described in Chapter 3. (b) Histogram showing that the size distribution of the PtNPs is 23 ± 2 nm. 65

Figure 3.2: Fluorescence calibration curve for estimation of ssDNA coverage. Calibration solutions of ssDNA-TAMRA were prepared in Taq buffer at concentrations ranging from 0.05 - 0.59 μM. After PtNP@ssDNA-TAMRA conjugates were prepared, the fluorescence of the supernatant was measured, and linear regression was used to calculate the concentration of unbound ssDNA. The DNA coverage per PtNP was estimated to be ~10^3 DNA per PtNP..... 70

Figure 3.3: (a) Nanoparticle tracking analysis (NTA) showing the normalized concentration of PtNPs as a function of their diameter for naked PtNPs in water (black), naked PtNPs in Taq buffer (red), and PtNP@ssDNA in Taq buffer (blue). (b) NTA showing the normalized concentration of PtNP@ssDNA:miRNA-203 as a function of their diameter before exposure to DSN in Taq buffer (black), after exposure to DSN in Taq buffer (red), after exposure to DSN and then resuspension in DI water (blue), and after exposure to DSN in 10 mM N_2H_4 + 50 mM PB (green). (c) Fluorescence emission recorded at 579 nm for PtNP@ssDNA:miRNA-203 assay for TAMRA-labeled PtNP@ssDNA before (red) and after (blue) incubation with DSN. 73

Figure 3.4: Au UMEs: (a) Current response before addition of PtNPs (black), after addition of 10.0 pM naked PtNPs (red), after addition of 10 pM PtNP@ssDNA (blue), and after addition of 10 pM PtNP@ssDNA that were incubated with DSN (green). (b) Current responses for 10 pM PtNP@ssDNA:miRNA-203 before (black) and after digestion by DSN (red). The PtNP@ssDNA:miRNA-203 conjugate was prepared using 1.0 µM miRNA-203. Digestion was carried out in Taq buffer at 42 °C for 4 h. (c) Expanded view of a section of the red trace in (b). The inset shows an even more expanded section. 77

Figure 3.5: Hg UMEs: (a) Current response prior to the addition of PtNPs (black) and after addition of 10.0 pM PtNP@ssDNA:miRNA-203 after digestion with DSN (red). The PtNP@ssDNA:miRNA-203 conjugate was prepared by incubating PtNP@ssDNA with 10.0 nM miRNA-203. Digestion was carried out in Taq buffer at 42°C for 4 h. (b) Expanded view of a section of the red trace in (a). (c) Plot of collision frequency as a function of the concentration of miRNA-203 used to prepare the PtNP@ssDNA:miRNA-203 conjugate. All experiments were carried out after digestion of the conjugate with DSN using the same conditions as in (a). The inset is an expanded view of the linear part of this plot. 81

Figure 3.6: ECA results for miRNA-203 mismatch studies. The concentration of the mismatch strands used for conjugation to PtNP@ssDNA was 10 nM. The *i-t* curves were obtained at 0 mV using a Au/Hg UME in a solution containing 50 mM PB + 10 mM N_2H_4. Current responses for (a) one mismatch (GUG AAA UGU UUU GGA CCA CUA G) and (b) five mismatches (GUG AAA UGU AAU CCA CCA CUA G) following exposure of the conjugates to DSN. No collisions are observed. 85

Figure 3.7: ECA results (*i*–*t* plots) obtained using Au/Hg UMEs and a solution containing 50 mM PB + 10 mM N_2H_4. The electrode potential was set to 0 mV. The data were obtained for the PtNP@ssDNA:miRNA-21 conjugate after digestion with DSN. The conjugate was prepared by incubating PtNP@ssDNA with miRNA-21, followed by digestion in Taq buffer with 4 U DSN at 42 °C. (a) Current responses obtained for the PtNP@ssDNA:miRNA-21 prepared by incubation with 10 nM miRNA-21 followed by DSN digestion. (b) Plot of collision frequency as a function of the concentration of miRNA-21 used to prepare the conjugate. The error bars represent the standard deviation from the mean for current transients obtained from three independent experiments at each concentration. Note that the range of concentrations here is more limited than in **Figure 3.5c**. 86

Figure 4.1: (a) Representative TEM image of the citrate-capped Pt NPs used in this study. (b) Histogram showing the size distribution of the Pt NPs. The average size is 57 ± 10 nm. 95

Figure 4.2: Histogram showing the zeta potential of the PtNPs as determined by Nanosight particle tracking analysis (Nanosight Model NS500, Malvern Instruments Ltd., United Kingdom). The average zeta potential is -59 ± 20 mV. The measurement was obtained in an aqueous solution containing ~1.28 pM PtNPs. 96

Figure 4.3: (a) CVs showing N_2H_4 oxidation at naked (black) and MUA-modified (red) 12.5 µm Au UMEs (no PtNPs present). The inset shows an expanded view of the limiting current at the MUA-modified UME. CVs recorded at 50 mV s^{-1}; 10.0 mM N_2H_4 in 50 mM PB (pH 7). (b) Square wave voltammetry (SWV) characteristic of electrochemical removal of MUA from the electrode surface. SWV parameters: 0.5 M KOH, 390 Hz frequency, 5.0 mV step increments, and 50 mV amplitude. (c) *i-t* curves obtained at +400 mV for a MUA-modified UME recorded in a solution containing 10.0 mM N_2H_4 and 50 mM PB (pH 7) in the absence (black) and presence (red) of 2.5 pM PtNPs. 101

Figure 4.4: *i-t* traces showing current transients resulting from collisions between Pt NPs and MUA-modified UMEs. The solution contained 10.0 mM N_2H_4 and 50 mM PB (pH 7). Plots show the change in current in the absence (black) and presence (red) of (a) 2.5 (a), 5 (b), 7.5 (c), 10 (d), and 12.5 (e) pM PtNPs. 104

Figure 4.5: Ellipsometric thicknesses of the PEM films obtained using MUA-modified Au-on-glass slides. These thicknesses do not include MUA, which has a height of ~1.7 nm on Au. (a) Individual thicknesses of PEM films terminated in either pLL (black) or pGA (red). (b) Total thicknesses of the films with increasing *n*. 106

Figure 4.6: Electrochemical results obtained using a pLL-modified Au UME. For all experiments, the solution contained 10.0 mM N_2H_4 and 50 mM PB (pH 7). (a) CVs for a pLL-modified UME before (black) and after (red) a 600 s collision experiment using 5.0 pM PtNPs. (b) *i-t* curves recorded at +400 mV in the absence (black) and presence (red) of 5.0 pM PtNPs. The inset shows an expanded view of a current transient exhibiting a step-like profile. (c) Histogram showing the distribution of current amplitudes for individual collisions. The average collision size is 140 ± 200 pA. (d) Plot of current-transient frequency (steps and peaks) as a function of the concentration of PtNPs. The error bars represent the standard deviation of current signals obtained from three separate experiments at each concentration. 108

Figure 4.7: *i-t* traces showing current transients resulting from collisions between PtNPs and pLL-modified UMEs. The solution contained 10.0mM N_2H_4 and 50 mM PB (pH 7). Plots show the change in current in the absence (black) and presence (red) of (a) 2.5, (b) 5.0, (c) 7.5, (d) 10.0, and (e) 12.5 pM PtNPs. 109

Figure 4.8: CVs obtained using pLL-modified Au UMEs. (a) before (black trace) and after (red trace) introduction of 5.0pM PtNPs in a solution containing 10 mM N_2H_4 and 50 mM PB (pH 7). Immediately after a CV of the pLL-modified UME was taken, PtNPs were introduced into solution, and an *i-t* curve was recorded for 600 s at +400 mV. Subsequently, the UME was rinsed and re-immersed in fresh N_2H_4 solution, and the red trace was obtained. (b) CVs obtained before (black trace) and after (red trace) incubation of the pLL-modified UME in a solution containing 128 pM PtNPs for 20 min. Scan rate = 50 mV/s.112

Figure 4.9: (a) SEM image of the pLL-modified Au UME surface after exposure to 12.5 pM PtNPs for 10 min. Arrows designate the adsorption of single PtNPs. (b) Higher magnification SEM image of the same electrode. The circle indicates the presence of NP aggregates on the film. 113

Figure 4.10: (a) Plot of average collision current for each pLL-modified Au UME versus the limiting current for N_2H_4 oxidation. The experiments were carried out in solutions containing 10.0 mM N_2H_4 and 50 mM PB (pH 7). The limiting current was determined from CVs obtained immediately after UME modification but prior to recording *i-t* curves in the presence of PtNPs. (b) Scatterplot of collision frequency versus the limiting current for N_2H_4 oxidation for each pLL-modified Au UME. The limiting current was determined from CVs obtained immediately after UME modification but prior to recording *i-t* curves in the presence of PtNPs. Three individual experiments are shown for each of five PtNP concentrations: 2.5 (black), 5.0 (green), 7.5 (orange), 10.0 (blue), and 12.5 (red) pM. 115

Figure 4.11: Electrochemical results obtained using a Au UME coated with a pLL-pGA PEM film. (a-e) *i-t* plots obtained at +400 mV in the absence (black) and presence (red) of Pt NPs at the indicated concentrations. (f) CVs obtained before (black) and after (red) a 600 s collision experiment using a 5.0 pM Pt NP solution. Scan rate: 50 $mV\,s^{-1}$. Solutions for all experiments contained 10.0 mM N_2H_4 and 50 mM PB (pH 7). 118

Figure 4.12: Electrochemical results obtained using a pLL-pGA-pLL-modified Au UME. For all experiments, the solution contained 10.0 mM N_2H_4 and 50 mM PB (pH 7). (a) *i-t* curves obtained at +400 mV recorded in the absence (black) and presence (red) of 5.0 pM PtNPs. (b) Histogram showing the distribution of current amplitudes for individual collisions. The average collision amplitude is 157 ± 114 pA. (c) Plot of the frequency of current transients (steps and peaks) as a function of the concentration of PtNPs. The error bars represent the standard deviation of current signals obtained from three separate experiments at each concentration. (d) CVs for a pLL-pGA-pLL-modified UME before (black) and after (red) a 600 s collision experiment using 5.0 pM PtNPs. 121

Figure 4.13: *i-t* traces showing current transients resulting from collisions between PtNPs and pLL-pGA-pLL-modified UMEs. The solution contained 10.0 mM N_2H_4 and 50 mM PB (pH 7). Plots show the change in current in the absence (black) and presence (red) of (a) 2.5, (b) 5.0, (c) 7.5, (d) 10.0, and (e) 12.5 pM PtNPs. 122

Figure 4.14: (a) Plot of average collision size for each pLL-pGA-pLL-modified UME versus the limiting oxidative current for collision experiments performed in 10.0 mM N_2H_4 + 50 mM PB (pH 7). The limiting current was determined from CVs obtained immediately after UME modification and prior to recording *i-t* curves. There is no correlation between collision size and limiting current. (b) Scatterplot of frequency of collision events as a function of the limiting oxidative current of each pLL-pGA-pLL-modified electrode. The limiting current was determined from CVs obtained immediately after UME modification and prior to recording *i-t* curves. Three experiments at five concentrations of PtNPs are shown: 2.5 (black), 5.0 (green), 7.5 (orange), 10.0 (blue), and 12.5 (red) pM. There is no correlation between frequency and limiting current. 124

List of Illustrations

Illustration 1.1: Electrode blocking by microbead collisions 1

Illustration 1.2: Electrocatalytic Amplification on Au and C UMEs and resulting current response. 3

Illustration 1.3: Scheme showing experimental setup for correlated electrochemical and optical tracking of microbead collisions 7

Illustration 1.4: ECA Collisions on Hg-modified Pt UMEs and resulting current response 10

Illustration 1.5: Detection of Individual DNA Hybridization Events in a Microfluidic Device[69] 17

Illustration 1.6: Scheme showing the effects of modifying electrode and PtNP surface with ssDNA 19

Illustration 2.1: Scheme of PtNP@ssDNA Digestion via Exo I 24

Illustration 3.1: Scheme demonstrating miRNA detection via ECA and DSN Cleavage 58

Illustration 4.1: Scheme showing ECA on PEM-modified Au UMEs 93

Chapter 1: Introduction

1.1 Electrochemical Detection of Particle Collisions

The study of observing and characterizing the chemical behavior of individual nanometer-sized particles on a surface is relatively recent, less than 30 years old,[1,2] and the bulk of the work since then has been carried out using spectroscopy and scanning probe microscopy.[3] It is only within the last 15 years that electrochemical work has been published, the first study being that of liposome particles colliding with Hg electrodes in 2002 by Scholz.[4-6] Two years later Lemay and coworkers observed collisions between individual micron-scale, carboxylated latex spheres and an electrode surface arising from partial masking of the electroactive area of the electrode by the insulating spheres.[7] The general scheme of their experiment is shown in **Illustration 1.1.**

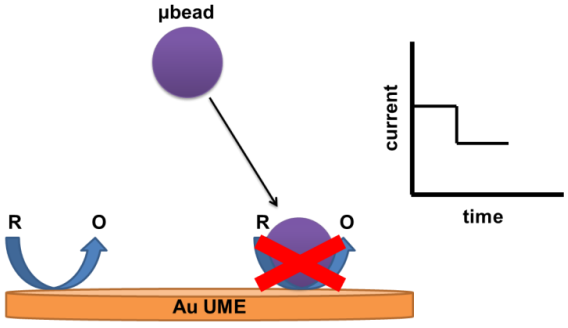

Illustration 1.1: Electrode blocking by microbead collisions

In this experiment, they poised the potential of an Au microelectrode at the steady-state oxidation of FcMeOH and recorded the current as a function of time (*i*-*t*). When the beads struck the electrode, they blocked a portion of the working electrode, causing a decrease in current in the *i*-*t* trace in the form of ''steps''. The group also noted that bead flux, or the amplitude of these ''steps'', was proportional to the limiting current. Using this technique, individual bead collision events at an electrode interface could be detected in real-time.

1.2 Electrocatalytic Amplification of Nanoparticle Collisions

An alternative technique, which is the focus of this dissertation, involves purely electrochemical means of detecting single catalytic metal nanoparticles as they collide with an inert electrode. This approach, named electrocatalytic amplification (ECA), was first pioneered by the Bard group.[8] They have extensively studied the fundamental science of this real-time particle detection system.[3,8-21] The basic principle behind these experiments involves poising a micro-scale ultramicroelectrode (UME) at a potential at which little faradaic current flows when recording a chronoamperometric trace (*i*-*t*). Typically, there is a redox probe in solution, chosen such that the electrode material

is inert for the particular reaction. When nanoparticles (NPs) that exhibit catalytic activity for the reaction are introduced into solution, they collide with the electrode and facilitate electrode transfer through the interface, driving the redox reaction on the surface of the NP. These bursts of current are detected on the *i-t* trace as individual current transients. **Illustration 1.2** shows a scheme of this system.

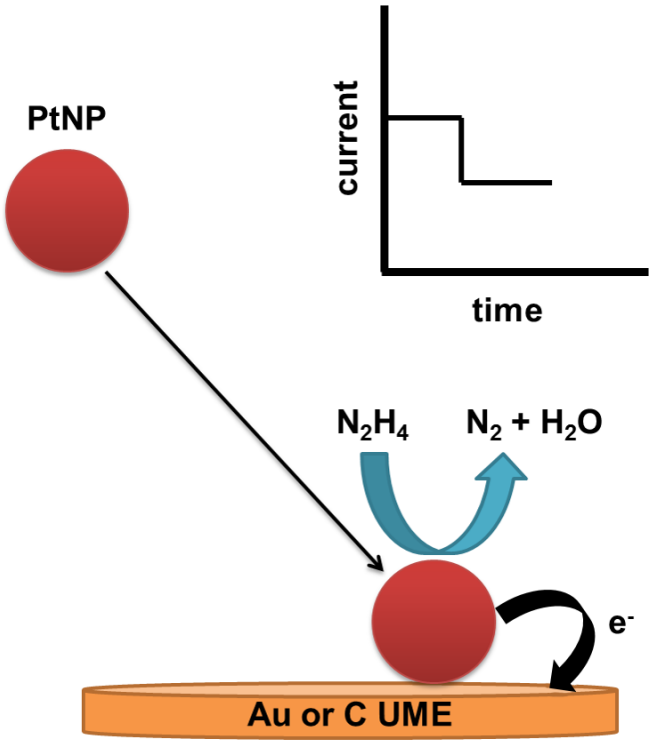

Illustration 1.2: Electrocatalytic Amplification on Au and C UMEs and resulting current response

In particular, this work will focus on developing the ECA platform for sensor applications with N_2H_4 oxidation as the redox probe, PtNPs as the catalytic NPs, and Au and Hg-

modified UMEs as our inert electrodes. **Illustration 1.2** shows the typical current response when PtNPs strike the electrode. The PtNP adsorbs onto the surface, producing a ''step''-like current transient. These collision events are characterized by the amplitude of the step. The theoretical current amplitude generated by spherical NPs at a planar electrode is given by **equation 1.1.**[9]

$$I=4\pi(\ln 2)nFDCr \quad (1.1)$$

Where D is the diffusion coefficient of the redox molecule at concentration C, n is the number of electrons participating in the redox reaction, F is Faraday's constant, and r is the radius of a single NP. This current is proportional to the size of the NPs, and thus, by compiling the sizes of collision events observed, ECA has proved to be an effective technique for rapid size screening of NP samples. Additionally, the technique is sensitive. Metal NPs can easily be detected at pico-, femto-, and even attomolar concentrations. Another unique advantage of this technique is that NPs can be detected in real-time, providing valuable information about their mass transport.

In addition to the Au UME/Pt NP/N_2H_4 system, a number of other combinations of redox species (N_2H_4, BH_4^-, H_2O (oxidation), H_2O_2, and H^+), and electrode materials (C, Au, Pt, Pt-O) have been identified that yield signatures of collisions.[3] The Unwin group has shown that collisions can be

observed on surface oxide-covered Au UMEs with Au NPs, either by direct oxidation of the NPs, or with an ECA setup.[22]

The Compton group has also published numerous works studying NP collisions.[23-33] Their research focus has been primarily to demonstrate and obtain an understanding of NP collisions using direct electrodeposition[24,30] and electrodissolution[32] of metals. Notably, they developed a technique in which AgNPs were directly oxidized into ions, yielding sharp current transients corresponding to direct faradaic current.[32] They have also tagged NP surfaces with redox probes, and studied the impacts that result from these electroactive groups to gain information such as NP porosity.[33] The Wolfrum group[34] developed an on-chip sensor for detection of AgNPs at subpicomolar concentrations using a microelectrode array. The AgNP direct oxidation system also has the advantage of being viable under non-aqueous conditions, such as in ionic liquid solutions.[35] Recent insight from the White group has suggested that these AgNP oxidations occur in several temporally resolved and discrete event, as evidenced by their analysis of multipeak behavior.[36]

1.3 Developments in Mass Transport of Particles

One of the main challenges in achieving low limits of detection via stochastic electrochemical particle detection

is transport of these particles to the electrode surface. In the pioneering work of Bard on metallic nanoparticles[8], the particles in the system were limited by diffusion-controlled mass transport. Studies on insulating bead experiments, however, first by Lemay[7] and later Bard,[37] showed that decreasing the concentration of electrolyte, and thus introducing electrophoretic migration into the transport dynamics, increased the frequency of bead collisions. This is because in both studies, the beads carried an overall net negative charge on the surface. The Bard group also used COMSOL modeling to confirm their experimental results. We later expanded on these studies by demonstrating correlated electrochemical and optical tracking of these bead collision events.[38] We found that larger collision signals are produced when beads adsorb nearer to the edge of the electrode, rather than the center. This is because the diffusive flux of the redox probe, FcDM, is blocked at the edges of the UME, because a disk UME is not uniformly accessible. **Illustration 1.3a** shows the setup for this experiment, where an electrochemical cell is positioned atop a microscope objective that is focused on the surface of the electrode. When a fluorescent bead strikes the electrode, it adsorbs and blocks an active site (**Illustration 1.3b**) and causes a step-like decrease in current (**Illustration 1.3c**).

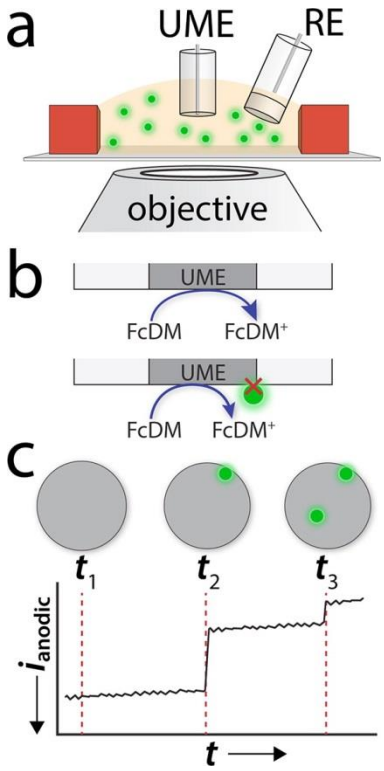

Illustration 1.3: Scheme showing experimental setup for correlated electrochemical and optical tracking of microbead collisions

Electromigration is also a viable form of mass transport for conductive PtNPs, with collision frequencies increasing as negatively-charged citrate-capped PtNPs are attracted to the electrode via electric field.[12]

Another method of increasing the rate of mass transport is the use of magnetism. Using magnetic iron oxide microbeads to block oxidation of ferrocenedimethanol, we demonstrated a higher frequency of collision events in a microfluidic device by positioning a magnet beneath the working electrode.[39] Using this setup, we achieved sub-attomolar levels of detection,

four orders magnitude lower than previous reports. We then extended this system to detect composites consisting of magnetic microbeads conjugated to AgNPs via hybridized DNA strands at a magnetized Ni microelectrode.[40] Notably, this work was based on detecting the dissolution of AgNPs rather than the blocking nature of insulating beads.

The link between magnetic enrichment of microparticles and that of NPs was further established by the development of hybrid magnetic/catalytic NPs by the Stevenson and Crooks groups.[41] Here, they synthetic protocol that incorporated a magnetic core (Fe_3O_4 nanoparticles) decorated with catalytic Pt on the surface. These hybrid Fe_3O_4/Pt NPs exhibited catalytic activity for ECA using the N_2H_4 indicator reaction, as well as higher frequencies due to magnetic enrichment in a microfluidic device.

1.4 Electrode Materials

As discussed previously, the first ECA experiments used Au and C UMEs as the working electrode. We chose to use Au UMEs to conduct our studies because Au UMEs were found to be more reproducible and simpler to electrochemically clean via voltammetric cycling when compared to C UMEs. When PtNPs collide with the Au surface, they adsorb and form a ''staircase'' like response: the overall current in the *i-t*

trace increases with successive oxidation events, and each collision event yields a step-like current transient.[3] We have found, however, that introducing PtNPs to DNA-based assays yields collision signals that are difficult to resolve, with signals superimposed on each other and shifting baselines.[42]

To address this challenge, experiments were also performed on Hg-modified UMEs. The use of this type of electrode material for ECA collisions was first demonstrated by the Stevenson group.[43-45] They demonstrated PtNP collisions due to N_2H_4 oxidation on Hg-modified Pt UMEs (Hg/Pt UMEs). When PtNPs come in contact with the Hg surface, Hg poisons Pt, deactivating the catalytic activity of the Pt for N_2H_4 oxidation. As a result, the current transients from these collision events yield a sharp, ''spike''-like response. These transients also decay rapidly to a steady baseline, suppressing the background current by two orders of magnitude when compared to Au UMEs. They also yielded increased signal-to-noise ratio for individual collisions. The scheme for this system, along with the typical current response showing ''spike-like'' transients, is shown in **Illustration 1.4**.

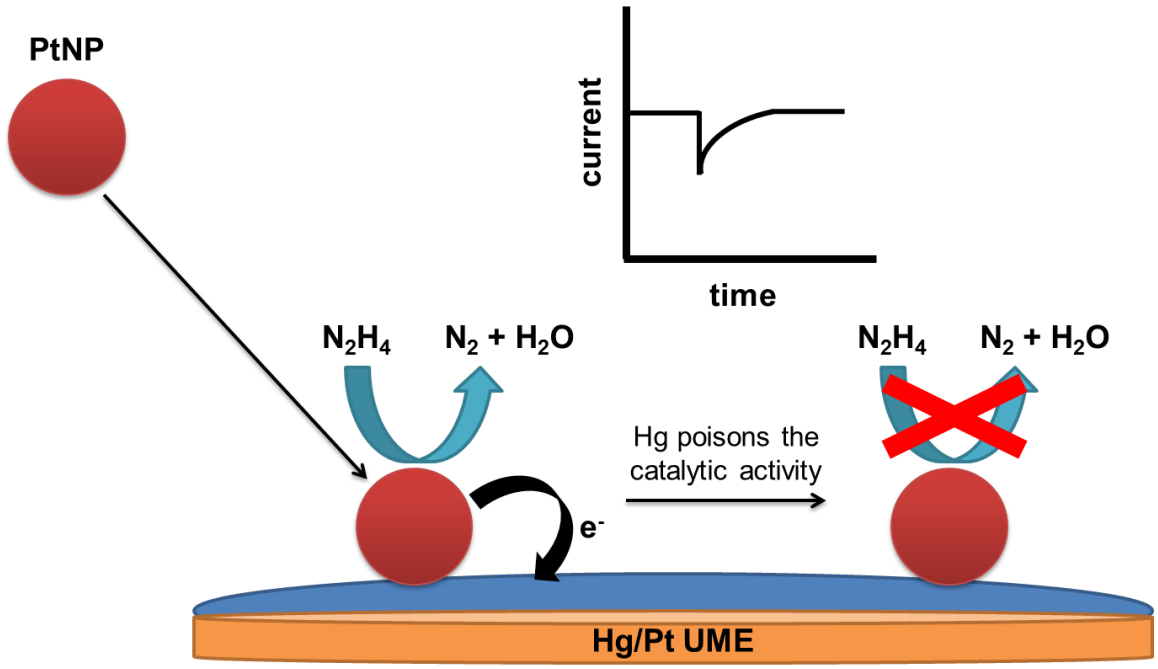

Illustration 1.4: ECA Collisions on Hg-modified Pt UMEs and resulting current response

Interestingly, both types of current responses have been observed on Ni UMEs.[46] The current response was dependent on the applied potential, with ''staircase'' collisions occurring at 0 V (vs Ag/AgCl), and the deactivating ''blip'' collisions occurring at 0.1 V. Although the exact mechanism of PtNP deactivation is not yet known, these studies suggest that it may be caused by a reaction product.

Recently, nanoelectrodes have also been investigated for their functionality as ECA electrodes.[47,48] Nanoelectrodes offer the advantage of extremely low background current, as well as the ability to immobilize and study the electrocatalytic behavior of a single nanoparticle.

An alternative method of lowering the background current of an electrode is to modify the surface with a passivating film. A technique which involves modifying Au UMEs with a self-assembled monolayer (SAM) and polyelectrolyte multilayer films will be discussed in this dissertation, in Chapter 4. Immobilizing an insulating layer on conductive UMEs allows researchers to fine-tune the surface for specific properties, such as charge, as well as the electron transfer kinetics. The Bard group first reported passivating Pt UMEs with TiO_2 films.[18] The thickness of their films varied between 1.0 and 2.2 nm, so any PtNPs that collide atop the film undergo electron transfer via tunneling. They used ferricyanide reduction as their redox indicator. The Unwin[49] group has also investigated the impact of surface chemistry on nanoparticle collisions using ferrocyanide oxidation. Au UMEs were modified with SAMs having different terminating groups: OH^-, COO^-, and CH_3. They found that using citrate capped AuNPs with a net negative charge yields a repulsion effect on electrodes modified with COO^--terminated alkanethiols.

1.5 Fundamental Studies of Metallic Nanoparticle Impacts

The capability of being able to investigate nanoparticles ‘‘one-at-a-time’’ is a powerful tool for

fundamental studies, especially in the understanding of reaction mechanisms and kinetics. The Compton group, for example, conducted a comprehensive study on the kinetics of the hydrogen oxidation reaction, both on ensembles of dropcasted PtNPs and via PtNP collision experiments.[50] They found that the kinetic rate constant obtained from collision events is faster than that at ensemble PtNPs. They also used this technique to study the lithium ion transfer kinetics in $LiMn_2O_4$ nanoparticles,[51] something of valuable importance to the development of improved and safer lithium ion batteries. They determined that the rate-determining step at high overpotentials is the transfer of the cation at the NP-electrolyte interface.

One of the most exciting, state-of-the-art techniques to couple with amperometric detection of catalytic nanoparticles is that of fast scan cyclic voltammetry (FSCV) by the Zhang group.[52,53] This technique enables one to obtain a transient voltammetric response for every individual collision event, providing rich information on catalytic activity. They employed this technique to extract kinetic constants for hydrazine oxidation on both Pt and AuNPs and also concluded that the capping agent on the NPs could play more of a part on reaction kinetics than crystallinity or surface orientation.

1.6 Electrochemical Detection of Soft Particles

''Soft'' particles, or particles of organic composition rather than metallic, are attractive targets for their ability to encapsulate redox-active targets and small biological molecules. Several platforms have been reported in the literature for collision-based electrochemical tracking of micelles,[54] liposomes,[55,56] emulsion droplets,[57-60] and polymer[61,62] particles. The first report was Compton in 2014, who reported nanoimpact experiments for C_{60} fullerene particles.[62] This was also the first report to incorporate non-aqueous conditions for collision experiments. By poising an Au UME at the oxidative potential for fullerene, they were able to fully oxidize fullerene molecules diffusing to the electrode surface, yielding sharp ''spike'' signals corresponding to dissolution of the carbonaceous NPs. These findings were closely followed by a report investigating drug-encapsulating liposomes.[56] Liposomes are attractive as effective delivery vehicles with a bilayer structure. To demonstrate their proof-of-concept model, they encapsulated vitamin C in liposomes and held C UMEs at the potential for vitamin C oxidation. They confirmed that the resulting current spikes were due to random collisions of the liposomes with the electrode surface. These liposomes then release vitamin C, which is then electro-oxidized.

It is also possible to characterize and detect emulsion droplets, as shown by the Bard group.[58,59] Rapid size characterization of these particles are of interest in many industrial applications, and the size of these particles affects the stability of the emulsion, optical properties, and rheology. They prepared emulsion particles containing hydrophobic redox molecules, such as ferrocene, and an ionic liquid, which can then collide with the hydrophilic UME surface to form a continuous aqueous phase. After these emulsion droplets collide, the redox molecules are electrolyzed, and a spike-type current profile is observed. The Chang group further expanded on this concept, presenting a platform in which they generated the emulsion droplets and electrochemically tracked their behavior in situ.[60]

1.7 Detection of Biological Targets

As a sensing platform, impact experiments offer the possibility of detecting one target in solution, an advantage unique to the technique. In addition to high sensitivity, these experiments are simple and able to generate a signal in a matter of seconds. Therefore, there has been a great deal of recent interest in the development of collision-based biosensors.

One of the first biosensors was reported by the Compton group,[63] in which they labeled AgNPs with *E. coli* bacteria, forming agglomerates of multiple AgNPs on a single bacteria, and detected the presence of bacteria by tracking the oxidation of AgNPs. They did not begin recording *i-t* curves until 10 min after injection of AgNPs, ensuring that only the larger AgNP-*E. coli* agglomerates produced signal. They also extended this approach for the detection of influenza viruses,[64] where they labeled single viruses with a high coverage of AgNPs. Compton also demonstrated direct detection of red blood cells using single entity electrochemistry, allowing for the ''counting'' of cells.[65] The method relies on the catalytic activity of red blood cells towards the decomposition of hydrogen peroxide as well as surface-induced haemolysis. Each cellular collision event is expressed as a sharp increase in current that decays back to baseline within a few seconds.

The Bard group has also published a number of papers demonstrating sensor platforms for biological targets using collision experiments.[66-68] They first demonstrated that much like insulating microbeads, biomolecules such as proteins, antibodies, and DNA macromolecules effectively block active sites on an electrode.[66] By holding the electrode at the limiting current for oxidation of ferrocyanide, they showed that these molecules also produce the characteristic

''stairstep'' response associated with insulating beads of a similar size. This approach was then adapted to detection of single viruses.[67,68]

1.8 ECA Sensors for DNA Detection

There has also been interest to adapt the ECA platform for sensing of oligonucleotides. The first report demonstrating the applicability of the N_2H_4/Au UME/PtNP system for biomolecule sensing was done by the Bard group.[16] They developed a DNA sensor in which the Au surface was modified with a probe strand, PtNPs were modified with a detection DNA strand, and both of these strands were complementary to the target strand of interest. After the UME was incubated with the probe DNA, it was then incubated with target DNA, and finally, incubated with DNA-modified PtNPs. They demonstrated that by placing this UME in N_2H_4 solution and recording the chronoamperometry, ECA collisions due to the presence of PtNPs could be observed. Using this approach, they were able to observe target DNA down to a level of 10 pM.

The Crooks group has also demonstrated the DNA sensor capabilities of the ECA platform on a microfluidic device.[69] In this work, we reported the development of a real-time ECA chip sensor for the detection of individual DNA hybridization events. As shown in **Illustration 1.5**, a

microfluidic device with an Au microband and a poly(dimethylsiloxane) channel was constructed using microfabrication methods.

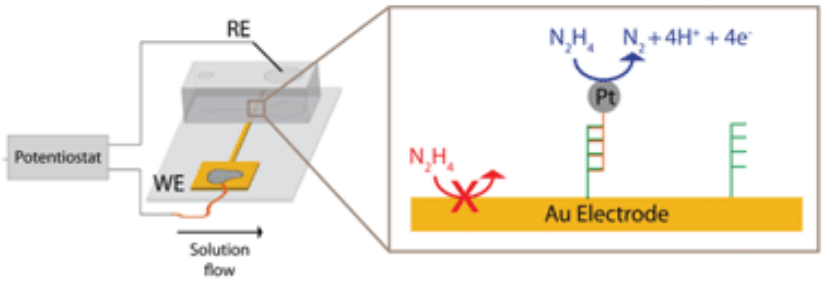

Illustration 1.5: Detection of Individual DNA Hybridization Events in a Microfluidic Device

The surface of the Au electrode was modified with a 25-base probe strand, and PtNPs were modified with the complementary strand. We found that in the presence of N_2H_4, when DNA-modified PtNPs were flowed in at a rate of 50 nL min^{-1}, current transients corresponding to individual DNA hybridization events could be observed on *i-t* traces. At the same flow rate, no collision events were observed when DNA-modified PtNPs were flowed down the channel without the DNA monolayer on the electrode. Similarly, when PtNPs were modified with a non-complementary strand containing a 5 base mismatch and introduced into the channel with the DNA monolayer on the electrode, no significant collisions were observed on the *i-t* trace. This demonstrated that the sensor was specific only to fully complementary DNA hybridization

events, and that these events could be detected in real-time. Using this sensor, we were able to detect the hybridization of individual DNA-modified PtNPs at concentrations as low as 25 pM.

1.9 DNA Surface Modification Studies of ECA

Shortly after the development of our DNA hybridization sensor, the Crooks group conducted various experiments to study the effects of modifying UME and NP surfaces with DNA.[70] The purpose of these experiments was to gain a fundamental understanding of the system for future sensor applications. Previous studies by the Bard group had examined the effects of carboxylic-acid-terminated *n*-alkanethiol monolayers on UME and NP surfaces on ECA collisions.[14] They reported that as the length of the *n*-alkanethiol increased on both NPs and UME surfaces from 3 to 16 carbons, the collision frequency and size of current transients decreased. In addition, they found that higher coverages of the *n*-alkanethiols also lead to lower frequencies and collision sizes.

In our study, we evaluated both ssDNA-modified and bare Au and Hg UMEs using both bare and ssDNA-modified PtNPs (PtNP@ssDNA) for N_2H_4 ECA collisions. A scheme of these experiments is shown in **Illustration 1.6**.

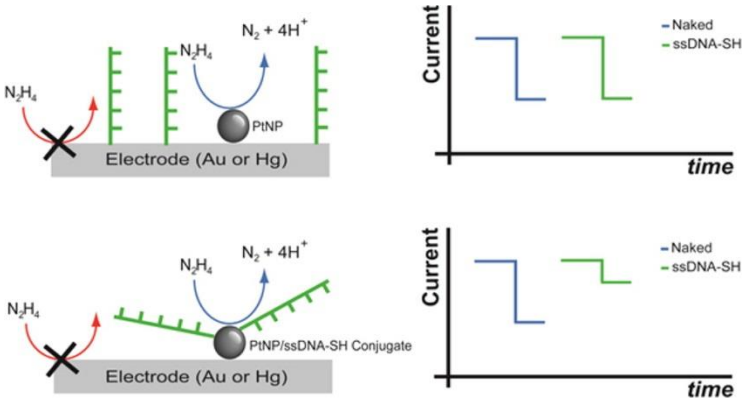

Illustration 1.6: Scheme showing the effects of modifying electrode and PtNP surface with ssDNA

Two different lengths of ssDNA were studied: a 5-base strand and a longer 25-base strand. We found that modification of the electrode surfaces with monolayers of either strand had little effect on the size and frequency of collision events. When we tested collisions of PtNP@ssDNA on bare Au and Hg, however, we observed significant decreases in the frequency and size of collision events. We found that this effect was correlated with higher modification ratios of ssDNA-to-PtNPs: that is, PtNP@ssDNA modified at a 50:1 ssDNA:PtNP ratio showed more profound passivation of ECA collisions than PtNP@ssDNA modified at a 5:1 ssDNA:PtNP ratio. Lastly, this deactivation effect also depended on the length of the ssDNA strand, with the 25-base strands showing a more rapid decrease in size and frequency at lower ssDNA:PtNP modification ratios.

This leads to a serious challenge in using the N_2H_4/PtNP ECA system for sensing applications, and the aim of this dissertation is to address this problem with a solution involving enzymatic cleavage of ssDNA on PtNPs.

1.10 Research Summary and Dissertation Overview

This dissertation focuses on addressing the challenge of adapting the ECA PtNP collision platform for specific detection of oligonucleotides. The challenge of reactivating DNA-passivated PtNPs by enzymatic digestion of the surface strands will be explored, as well as extending this general approach for the specific detection of microRNAs (miRNAs). The development of such a sensor offers the advantage of analyte detection in real-time, high sensitivity, high specificity, and ease-of-use.

Chapter 2 discusses the proof-of-concept experiments conducted to demonstrate reactivation of PtNP@ssDNA on Au and Hg/Pt UMEs. PtNPs were modified with a high surface coverage of ssDNA. Consistent with our earlier report,[70] these PtNP@ssDNA conjugates yielded few collision signals. This is due to DNA-restricted access of N_2H_4 to the catalytic PtNP surface. After incubation of PtNP@ssDNA with 30 U of Exo I, however, about 50% of the collision activity (compared to naked PtNPs) is recovered. Exo I, which is specific to

cleaving ssDNA with a free 3’-hydroxyl end and cuts nucleotides in a stepwise fashion, removes much of the ssDNA originally present on the PtNPs.

We then extend this general principle to demonstrate the specific detection of miRNAs in Chapter 3. PtNPs were modified with ssDNA complementary to the miRNA of interest, and subsequently incubated with the miRNA strands. Incubating these conjugates with Duplex Specific Nuclease, which is specific only to DNA in DNA/DNA or DNA/RNA duplexes, cleaves the ssDNA strands on the PtNP surface, leaving miRNA free to bind with another immobilized ssDNA. These conjugates are then used in ECA collision experiments, and the frequency of collision events on Hg/Au amalgam electrodes was found to be linearly related with concentration.

Chapter 4 discusses ECA tunneling collision studies conducted on Au UMEs modified with passivating, electrostatically assembled polyelectrolyte multilayer (PEM) films. The results from these studies showed that despite the thickness of the insulating PEM films, which range up to 5 nm, electrons are able to tunnel from the PtNPs to the electrode, resulting in N_2H_4 oxidative collisions at the PEM film/solution interface. Secondly, we demonstrate that it is possible to control the frequency of collision events by manipulating the net electrostatic charge present on the outer surface of the PEM films. These results provide

interesting insight into the tuning of ECA current transients.

1.11 Accomplishments

There are three major accomplishments that will be highlighted in this dissertation. The first is the development of a ‘‘turn-on’’ ECA biosensor, an experimental design which solves the problem of conjugation of biomolecules electrochemically passivating metallic NPs. The second is addressing the issue of PtNP aggregation during ECA experiments. As will be shown in Chapters 2 and 3, modifying PtNPs with a shell of ssDNA stabilizes the colloidal dispersion in the presence of relatively high ionic strength environments, even after enzymatic digestion at elevated temperatures. Lastly, Chapter 4 will demonstrate the ability to turn ECA collisions ‘‘on’’ and ‘‘off’’ by modifying the electrode surface with electrostatically charged polymers.

Chapter 2: Electrocatalytic amplification of DNA-modified nanoparticle collisions via enzymatic digestion[1]

INTRODUCTION

Here we report a new and general approach that will be useful for adapting the method of electrocatalytic amplification (ECA) to biosensing applications.[3] As shown in **Illustration 2.1a**, the original version of ECA occurs when a catalytically active nanoparticle (NP) strikes an appropriately poised inert electrode in the presence of a suitable redox molecule. In this case, significant current flow, arising from a redox indicator reaction, is only observed when the particle is in contact with the electrode. Therefore, it is possible to distinguish individual collisions between nanoparticles and the electrode surface.

[1] Castaneda, A. D.; Robinson, D. A.; Stevenson, K. J.; Crooks, R. M. *Chem. Sci*. **2016**, 7, 6450-6457. ADC was the primary author. DAR assisted with design of Hg experiments, and KJS was DAR's research advisor. RMC was the primary research advisor.

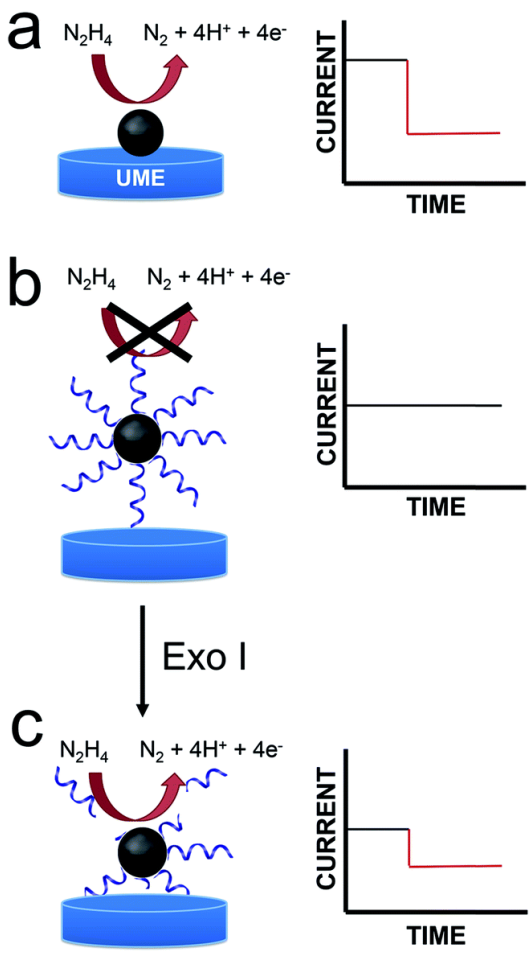

Illustration 2.1: Scheme of PtNP@ssDNA Digestion via Exo I

We are interested in using ECA to detect small numbers of biological molecules such as DNA. Previous work from our lab has shown, however, that when DNA is present on colliding NPs, very little current results.[70] This is, of course, a consequence of DNA-induced blocking of catalytically active sites on the NP surface. This finding presents a clear problem for integration of ECA into biosensing schemes: specifically, if a biological recognition element is immobilized on the

NPs, then little or no current will be observed upon impact. Here we present a strategy that at least partially addresses this difficulty. Specifically, we start with catalytically inactive DNA-modified NPs, and then detect the presence of DNA using an enzyme (an exonuclease) that degrades DNA sufficiently to reactivate the catalytic properties of the NPs. Importantly, the goal of the present work is to introduce a general methodology that could be useful for a range of future biosensing applications. At this early stage in our research, we do not intend to suggest that the metrics presented here are competitive with the many other DNA sensing methods that have been reported.

For the present study, we chose N_2H_4 oxidation as the redox indicator reaction, because this inner-sphere electron-transfer reaction is catalyzed by PtNPs but not by Au or Hg ultramicroelectrodes (UMEs).

$$N_2H_4 = N_2 + 4H^+ + 4e^- \quad (2.1)$$

Accordingly, when an appropriate interfacial potential is selected for the UME, no current due to **equation 2.1** is observed until a PtNP strikes the electrode surface. The current transients that result from these collisions are step-shaped for Au UMEs[9] and spike-shaped for Hg UMEs.[43-45] The rapid current decrease observed for Hg UMEs is due to deactivation of the PtNPs resulting from Hg poisoning.

Enzymes have heretofore not been integrated into ECA sensing schemes, but we were inspired by the surface-enzyme chemistry reported by Corn and coworkers[71,72] over the past several years, and we thought coupling the two methods could be quite powerful. This work focuses on the use of nucleases, which are a family of enzymes capable of hydrolyzing the phosphodiester bonds in DNA chains.[73] The difference between endo- and exonucleases lies in the way each class initiates hydrolysis. Endonucleases cleave phosphodiester bonds at a specific site within the middle section of the oligonucleotide, while exonucleases initiate cleavage at a free -OH group on either the 5′ or 3′ end.[74] The 5′ to 3′ exonucleases are commonly used in biology to remove RNA primers,[75,76] whereas 3′ to 5′ exonucleases are used to help repair DNA mismatches.[77] A number of analytical assays incorporate the use of nucleases for operating on nanoparticles conjugated with DNA. These include schemes involving detection via colorimetry,[78,79] fluorescence,[80] and electrochemistry.[81] For this study, we used Exonuclease I (Exo I), a nuclease extracted from E. coli, which is selective for denatured or single-strand DNA (ssDNA). Exo I initiates cleavage at a free 3′-hydroxyl end of ssDNA and cuts nucleotides in a stepwise fashion.[82]

In the present work, we modified 22 nm-diameter PtNPs with 25-mer ssDNA. Consistent with an earlier report from

our group,[70] these PtNP@ssDNA conjugates yield few collision signals (**Illustration 2.1b**), because DNA restricts access of N2H4 to the electrocatalytic PtNP surface. After incubation of PtNP@ssDNA with 30 U of Exo I, however, about 50% of the collision activity (compared to naked PtNPs) returns (**Illustration 2.1c**). This is because Exo I removes much of the ssDNA originally present on the PtNPs. The key result is that these findings point to a general approach for using ECA to detect small molecules, proteins, and DNA.

EXPERIMENTAL

Chemicals and Materials

$MgCl_2$, $(NH_4)_2SO_4$, 2-mercaptoethanol, Tris-HCl, $ZnCl_2$, glycerol, L-ascorbic acid, citric acid, $NaBH_4$, and $N_2H_4 \cdot H_2O$ were purchased from Sigma-Aldrich (St. Louis, MO). Sodium citrate and sodium phosphate monohydrate were purchased from EM Science (Billerica, MA). $H_2PtCl_6 \cdot 6H_2O$ (99.9%) was purchased from Strem Chemicals (Newburyport, MA). Tween 20 and NaCl were obtained from Fisher Scientific (Pittsburgh, PA). All reagents were used as received. The DNA conjugates, ssDNA (5′-(CH2)3-SH CAC GAC GTT GTA AAA CGA CGG CCA G-3′) and Cy3-ssDNA (5′-(CH2)3-SH CAC GAC GTT GTA AAA CGA CGG CCA G-Cy3-3′), were from Integrated DNA Technologies (Coralville, IA) and received as lyophilized pellets in microcentrifuge tubes.

The pellets were centrifuged to ensure no residue on the walls or cap remained, and then suspended in H_2O. Deionized (DI) water having a resistivity of 18.2 MΩ cm was used for all experiments (Milli-Q gradient water purification system, Millipore, Bedford, MA). Experiments were conducted at room temperature (23 ± 2 °C). Unless otherwise stated, the phosphate buffer was adjusted to pH 7.

Synthesis and Characterization of PtNPs

PtNPs were prepared following a previously reported seed-mediated synthesis.[83] Briefly, 7.76 mL of a 0.2% (w/v) solution of H_2PtCl_6 were added to 100 mL of gently boiling H_2O. After 1.0 min, 2.37 mL of a solution containing sodium citrate (1%, w/v) and citric acid (0.05%, w/v) were added and the solution was allowed to boil for an additional 30 s. Next, 1.18 mL of a solution containing $NaBH_4$ (0.08%, w/v), sodium citrate (1%, w/v), and citric acid (0.05%, w/v) were added, and boiling was continued for 10 min. After cooling to room temperature, 3-4 nm Pt seed NPs were obtained.

A 1.0 mL aliquot of the PtNP seed solution was added to 29.0 mL of H_2O at room temperature. With stirring, 0.023 mL of a 0.40 M H_2PtCl_6 solution and 0.50 mL of a solution containing 1% sodium citrate and 1.25% L-ascorbic acid was added. The solution was then heated to boiling at the rate

of 10 °C min^{-1}. The total reaction time was 30 min. After cooling to room temperature, the solution was transferred to a 35 mm dialysis sack (12 000 Da MWCO, Sigma-Aldrich) and submerged in 4 L of DI H_2O for 24 h to remove excess salts. The PtNPs were characterized by transmission electron microscopy (TEM, FEI Tecnai TEM), and found to have an average diameter of 22 ± 4 nm. A representative TEM image and a histogram showing the NP size distribution are shown in **Figure 2.1.**

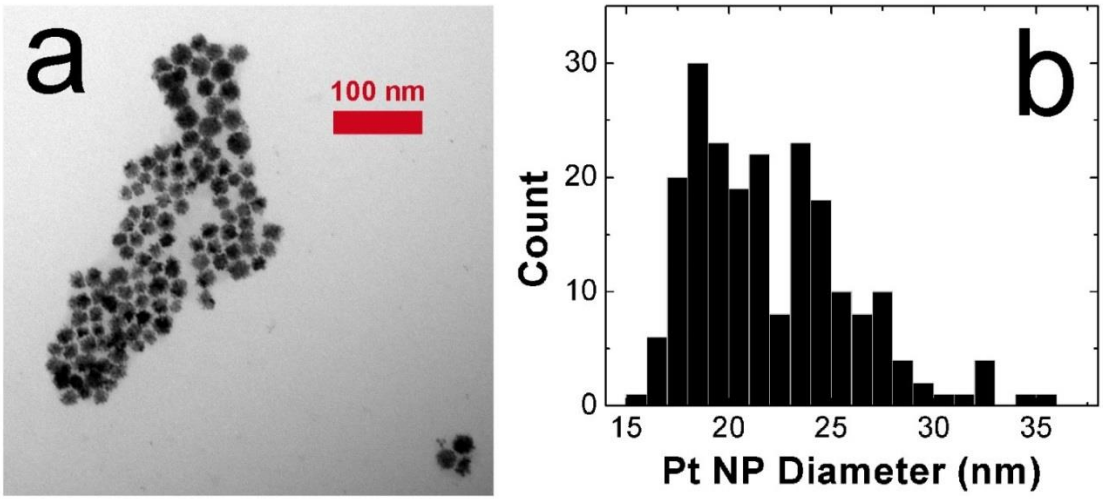

Figure 2.1: Analysis of PtNPs by transmission electron microscopy. (a) Representative TEM micrograph of the PtNPs used in this study and (b) Histogram indicating the size of the PtNPs: 22 ± 4 nm.

Preparation of PtNP@ssDNA Conjugates

PtNP@ssDNA conjugates were prepared using a modified version of a pH-assisted conjugation method previously reported for AuNPs and AgNPs.[84,85] Briefly, 400 µL of the 570 pM PtNP solution were mixed with 5.0 µL of 10.0 µM ssDNA (this yields a PtNP : ssDNA ratio of ~1:220). After 5 min, 25.0 µL of 100 mM citrate-HCl buffer (pH 3) were injected and mixed into the solution. After 5 min, an additional 25.0 µL of citrate-HCl buffer were added. After 25 min at room temperature, 400 µL of 100 mM HEPES buffer (pH 7.4) were added, and the solution was vortexed for ~5 s. The conjugates were then centrifuged at 16.6 G for 20 min, washed three times with DI water, and resuspended in Taq buffer (75 mM Tris-HCl (pH 8.8), 2 mM $MgCl_2$, 0.01% Tween 20, and 20 mM $(NH_4)_2SO_4$). For electrochemical measurements, a few tens of microliters of this resuspended solution was diluted in 5-10 mL of PB (pH 7) solution, so the final electrolyte solution contained a small percentage of Taq buffer.

These materials were used for all experiments reported herein, except for those relating to **Figure 2.4** where lower ratios of PtNP:ssDNA were used to gauge the effect of ssDNA surface concentration on ECA measurements. In those experiments the PtNP@ssDNA were resuspended in 50 mM PB (pH 7) rather than Taq buffer.

Enzymatic Digestion of PtNP@ssDNA

30 U of Exo I were combined with 400 µL of the PtNP@ssDNA solution in Taq buffer and immediately vortexed for 5 s. Subsequently, the solution was incubated at 37 °C for 1 h with gentle mixing at 200 rpm before immediate use.

UME Preparation

Au UMEs having a diameter of 12.5 µm and Pt UMEs having a diameter of 10 µm were purchased from CH Instruments (Austin, TX). Au UMEs were polished by wet sanding for 1 min. The Au UMEs were then submerged in piranha solution (1 : 3 30% H_2O_2/H_2SO_4) ***Caution!*** *Piranha solution can react violently with organic compounds and should be handled with care.* Next, they were electrochemically cleaned by immersing them in 0.1 M H_2SO_4 and cycling the applied potential between −0.35 and 1.35 V vs. Ag/AgCl (3.4 M KCl) for 25 cycles at 0.30 V s^{-1} (potentiostat model CH 700D, CH Instruments, Austin, TX). Before use, they were rinsed with H_2O and dried under a gentle stream of N_2.

Hg UMEs were prepared by electrodepositing Hg onto a Pt UME according to a previously reported method.[86] Briefly, the Pt UMEs were polished via wet sanding for 1 min. Hg was then electrodeposited (−0.10 V vs. Ag/AgCl, 3.4 M KCl) for 300 s from a solution containing 5.7 mM $Hg_2(NO_3)_2$, 0.5% conc. HNO_3,

and 1 M KNO_3. Finally, the Hg UMEs were rinsed with H_2O immediately before use.

Electrochemistry

Chronoamperometric (*i-t*) curves were obtained in a two-electrode cell using a Chem-Clamp voltammeter-amperometer (Dagan Corp., Minneapolis, MN) potentiostat coupled to a PAR 175 Universal Function Generator (Princeton Applied Research, Oak Ridge, TN) to apply the voltage. The potentiostat and function generator were interfaced to a Dell Optiplex 380 computer through a PCI-6251 data acquisition board (National Instruments, Austin, TX) using a BNC-2090A analog breakout accessory (National Instruments, Austin, TX). The electrochemistry data were obtained using a custom LabView program (National Instruments). The sampling time was 0.015 s. All electrochemistry experiments were shielded from environmental noise using a custom Faraday cage constructed from copper plate and mesh. For *i-t* experiments, the potential was held at –50 mV and 5 mV vs. Ag/AgCl for the Au and Hg UME experiments, respectively. Unless stated otherwise, all potentials are reported vs. a Ag/AgCl reference electrode (3.4 M KCl, model CH111, CH Instruments, Austin, TX) separated from the working electrode by a glass frit to minimize contamination.

Nanoparticle Tracking Analysis

The colloidal stability of PtNPs, PtNP@ssDNA, and PtNP@ssDNA post-Exo I was analyzed using nanoparticle tracking analysis (NTA, Malvern Instruments, Malvern, United Kingdom). NTA is a technique that utilizes light scattering and particle tracking to measure the size distribution and concentration of particles in a solution. Due to the narrow working concentration range of the instrument (<1 pM), NP solutions were diluted to a final concentration of 0.57 pM for PtNPs, 0.89 pM for PtNP@ssDNA, and 0.46 pM for PtNP@ssDNA post-Exo I.

Results and Discussion

Synthesis and Characterzation of PtNP@ssDNA

The PtNP@ssDNA conjugates were prepared using the fast, pH-assisted conjugation method discussed in the Experimental section. This procedure results in colloidally stable conjugates having a 22 nm-diameter Pt core and a ssDNA shell in under 1 h.[84]

To estimate the average number of ssDNAs per PtNP, a previously reported technique, which is based on fluorescence quenching by the PtNPs, was used.[84,87] For this purpose, the thiolated ssDNA was modified at the 3′ end with the

fluorescent dye Cy3 (ssDNA-Cy3), which has a maximum absorption wavelength at 550 nm and a maximum emission wavelength at 570 nm. Adsorption of ssDNA-Cy3 to the PtNP brings the dye sufficiently close to the NP surface to quench its fluorescence. Therefore, after modification of the PtNPs with Cy3-tagged ssDNA, residual fluorescence in solution will arise primarily from unbound ssDNA.

To carry out this analysis we first recorded a calibration curve for ssDNA-Cy3 in Taq buffer (**Figure 2.2**), and then measured the fluorescence of solutions containing PtNP@ssDNA-Cy3. By comparison of the residual fluorescence in the latter solution to the calibration curve, the concentration of bound DNA can be determined. Dividing this value by the concentration of PtNPs (determined by NTA) yields a rough estimate of the number of ssDNA-Cy3 per PtNP, which we find to be ~35. The conditions used to modify PtNPs with unlabeled DNA (e.g., PtNP@ssDNA) were the same as for PtNP@ssDNA-Cy3 to ensure similar coverages.

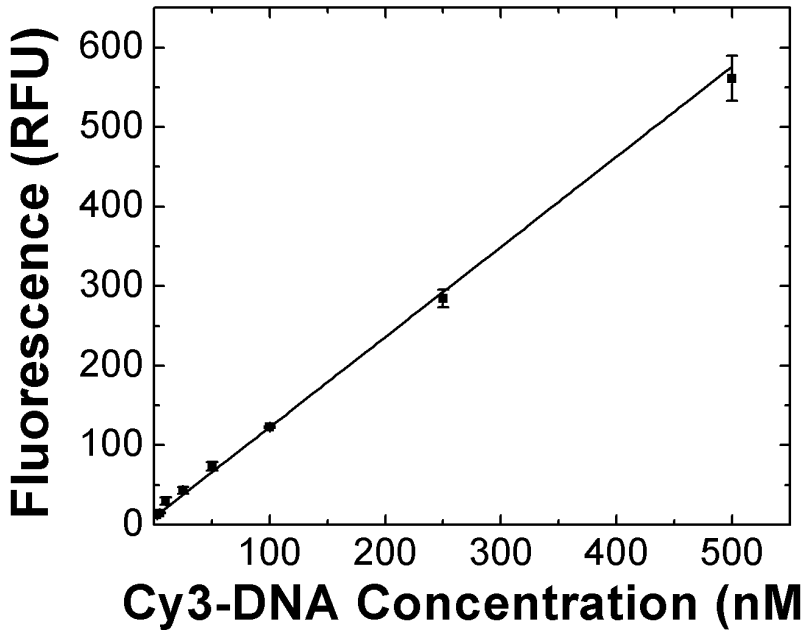

Figure 2.2: Fluorescence calibration curve used to determine the coverage of ssDNA for the PtNP@ssDNA materials. The DNA coverage per PtNP was estimated to be ~35 DNAs per PtNP. This value applies to all experiments discussed in the main text except those associated with **Figure 2.4.**

The poor colloidal stability of nanoparticles in ECA experiments is a very serious problem,[41,88,89] and therefore we evaluated this parameter for the PtNP conjugates used in this study prior to carrying out collision experiments. These NTA results (**Figure 2.3a**) indicate a size distribution of 46 ± 27 nm for nominally naked PtNPs (black trace) in 50 mM PB. This value can be compared to the size measured in water (no buffer): 28 ± 20 nm, indicating that the electrostatic shield effect of the buffer leads to some aggregation.[90,91] After

modification with ssDNA (PtNP@ssDNA), the size of the resulting conjugates in 50 mM PB is a little larger than the nominally naked PtNPs: 57 ± 31 nm (red trace) and 53 ± 29 nm (blue trace) before and after treatment with Exo I, respectively. Note that the aforementioned size distributions are the averages of three independent measurements.

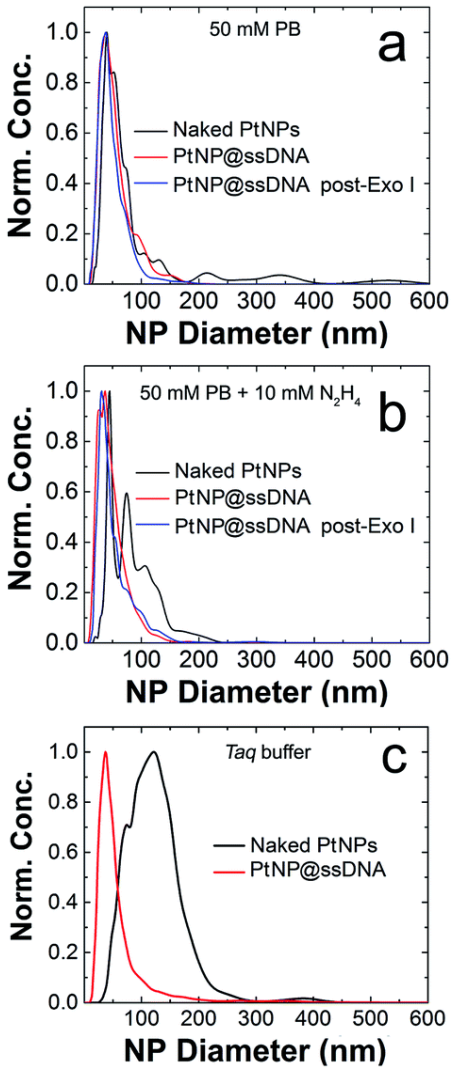

Figure 2.3: Representative size-distribution histograms, derived from nanoparticle tracking analysis, for the PtNPs used in this study. The types of PtNPs corresponding to each histogram are shown in the legend. The concentrations of PtNPs were: naked PtNPs, 0.57 pM; PtNP@ssDNA, 0.89 pM; and PtNP@ssDNA post-Exo I, 0.46 pM. Measurements were obtained in (a) 50 mM phosphate buffer (PB, pH 7), (b) 50 mM PB (pH 7) + 10 mM N_2H_4, and (c) Taq buffer. To account for the differences in NP concentration, the histograms are normalized to the highest concentration observed for each species.

It has previously been shown that the presence of N_2H_4 can increase the degree of aggregation of PtNPs,[88] and therefore we repeated the measurements shown in **Figure 2.3a** except included 10.0 mM N_2H_4 in the solutions (**Figure 2.3b**). The size distribution for naked PtNPs (black trace) in the presence of N_2H_4 confirms the earlier report. In this case the average PtNP diameter is 100 ± 45 nm. After addition of the ssDNA shell, however, the conjugates are stabilized, and the degree of N_2H_4-induced aggregation is reduced both before (PtNP@ssDNA, 52 ± 31 nm, red trace) and after (PtNP@ssDNA, 55 ± 35 nm, blue trace) exposure to Exo I. In other words, N_2H_4 has no significant effect on the colloidal stability of PtNP@ssDNA.

ECA of PtNP@ssDNA at Au UMEs prior to Exo I Digestion

We have previously reported that the presence of ssDNA on the surface of 4.6 nm PtNPs reduces both the magnitude and frequency of ECA collision signals arising from N_2H_4 oxidation on both Au and Hg UMEs.[70] To verify that this observation holds true even for the larger NPs used in the present study, we modified PtNPs using solutions containing the following ratios of PtNP : ssDNA——1:10, 1:25, 1:50, and 1:100, and then obtained ECA data using Au UMEs.

Figure 2.4a shows representative current-time (*i*-*t*) traces for N_2H_4 + 50 mM PB solutions in the absence of PtNPs (black trace), and in the presence of naked PtNPs (red trace), PtNP@ssDNA prepared using a PtNP : ssDNA ratio of 1:10 (blue trace), and PtNP@ssDNA prepared using a PtNP:ssDNA ratio of 1:100 (green trace). Obviously, no collisions are observed in the absence of PtNPs. Naked PtNPs produced an average ECA current transient frequency of 0.048 ± 0.006 Hz and current magnitude of 51 ± 41 pA (see **Figure 2.5** for additional *i*-*t* curves for collisions of nominally naked PtNPs with Au UMEs). This current is lower than that predicted by equation 1.1 (237 pA), which has previously been shown to yield reasonable agreement with experimental measurements involving smaller NPs (~3-4 nm).[3]

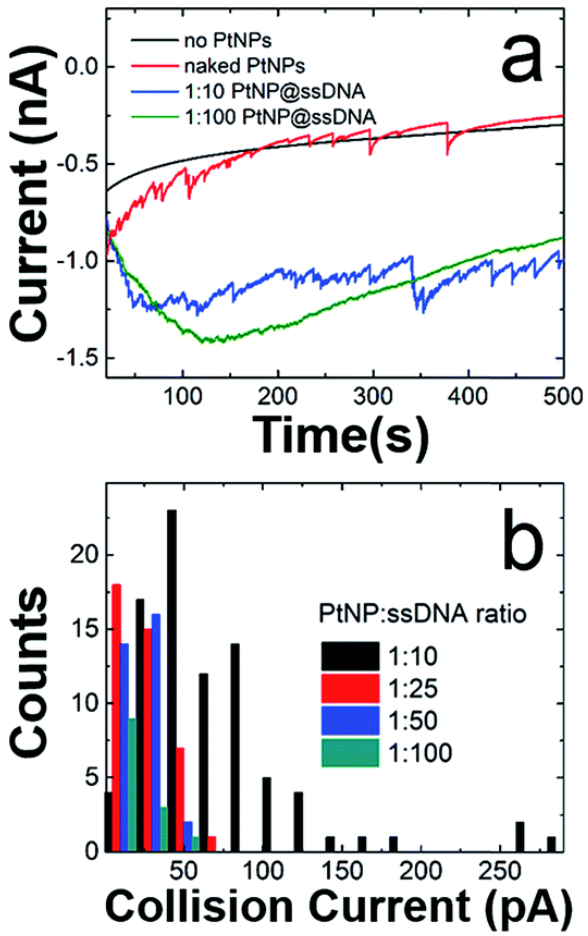

Figure 2.4: ECA results obtained using a Au UME and a solution containing 50 mM PB (pH 7) + 10.0 mM N_2H_4. (a) *i-t* curves obtained at E = −50.0 mV. The types of PtNPs used for each trace are shown in the legend. (b) Histogram showing the distribution of collision currents for the indicated ratios of PtNP:ssDNA. In all cases the indicated ratios refer to the PtNP:ssDNA ratio of the solution used to modify the PtNPs (not the actual surface concentrations of ssDNA on the PtNPs).

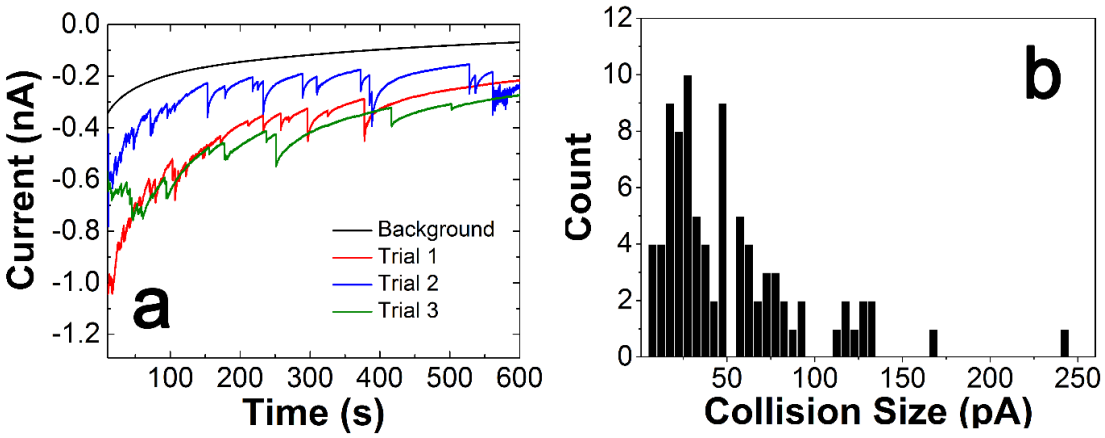

Figure 2.5: ECA results for collisions of naked PtNPs with an Au UME. The solutions contained 50 mM PB + 10 mM N_2H_4 (pH 7). (a) *i-t* traces in the absence (black trace) and presence (colored traces) of 11.7 pM PtNPs. The average collision frequency for the three trials was 0.048 ± 0.006 Hz. (b) Histogram showing the frequency of collisions as a function of current. The average collision current was 51 ± 41 pA.

In a previous study involving larger (57 nm) PtNPs, the predicted current was also larger than the experimental average.[92] In this case the calculated collision current was 613 pA, but the average measured current was only 185 ± 177 pA. We do not know why this calculation does not agree well with the experimental results for PtNPs larger than 3-4 nm, but one possibility is that the majority of collision signals arise from a relatively small subset of PtNPs residing at the low end of the size distribution. This in turn could be a consequence of the lower diffusion coefficients of larger PtNP aggregates. It is also known that N_2H_4 solutions

deactivate Pt electrodes (and by extension PtNPs), and this could also account for the lower-than-expected collision currents.[93]

The average ECA current and transient frequency resulting from collisions of PtNP@ssDNA (1:10), 51 ± 48 pA and 0.043 ± 0.006 Hz, respectively, were almost identical to those of the naked PtNPs. However, PtNPs with the highest ssDNA modification ratio revealed a much larger decrease in signal. Specifically, the average collision current for PtNP@ssDNA (1:100) was 17 ± 11 pA, a ~66% decrease relative to naked PtNPs. Additionally, the frequency decreased from 0.048 ± 0.006 Hz to 0.0072 ± 0.004 Hz.

Figure 2.4b is a histogram showing the distribution of ECA currents as a function of the PtNP:ssDNA solution ratio used to prepare the conjugates. These data reveal the quantitative attenuation in collision current as a function of increasing ssDNA coverage. Although not shown here, the collision frequency also decreases with increasing ssDNA coverage. This trend is consistent with data previously reported for 4.6 nm PtNPs.[70]

Colloidal Stability during Enzymatic Reactions

Enzymatic reactions with Exo I are commonly performed in an optimized reaction buffer consisting of 67 mM glycine-

KOH (pH 9.5), 6.7 mM $MgCl_2$, and 10 mM 2-mercaptoethanol. However, both naked PtNPs and PtNP@ssDNA precipitated in this reaction buffer within the required incubation period of 1 h. It is known, however, that Exo I also maintains 100% of its activity in a buffer optimized for the Taq polymerase: 75 mM Tris-HCl (pH 8.8), 2.0 mM $MgCl_2$, 0.01% Tween 20, and 20 mM $(NH_4)_2SO_4$.[94] Accordingly, we tested the colloidal stability of PtNPs in the Taq buffer and each of its components by carrying out NTA experiments.

Figure 2.3c presents normalized NTA data for both naked PtNPs (black trace) and PtNP@ssDNA (red trace). These data were obtained by resuspending the NPs in Taq buffer and incubating at room temperature for 1 h. An aliquot of the NP solution was then further diluted in Taq buffer to an appropriate concentration for NTA measurements (~0.5-1.0 pM). The important result is that the average size of naked PtNPs in the Taq buffer is 155 ± 119 nm compared to 44 ± 40 nm for those stabilized with ssDNA. The latter size can be compared to 57 ± 31 nm found for PtNP@ssDNA in 50 mM PB (**Figure 2.3a**). We conclude that PtNP@ssDNA are sufficiently stable in the Taq buffer to carry out the Exo I cleavage. NTA plots for the individual components of Taq buffer (75 mM Tris-HCl (pH 8.8), 2.0 mM $MgCl_2$, 0.01% Tween 20, and 20 mM $(NH_4)_2SO_4$) can be found in **Figure 2.6**. The tabulated results can be found in **Table 2.1**.

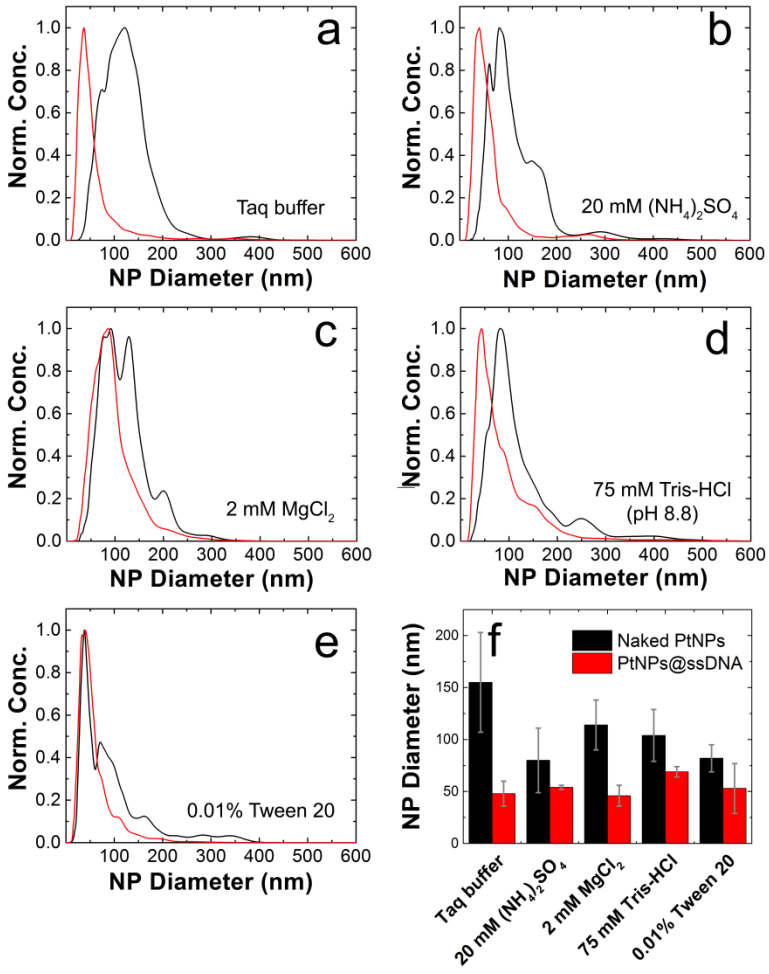

Figure 2.6: Nanoparticle tracking analysis showing the normalized concentration of PtNPs as a function of their diameter for naked PtNPs (black traces) and PtNP@ssDNA (red traces) in (a) Taq buffer, (b) 20 mM $(NH_4)_2SO_4$, (c) 2.0 mM $MgCl_2$, (d) 75 mM Tris-HCl (pH 8.8), and (e) 0.01% Tween 20. (f) Histogram showing the average PtNP diameter in Taq buffer and the individual buffer components.

Solution	Naked Pt NPs (nm)	PtNPs@ssDNA (nm)
Taq buffer	155 ± 119	44 ± 40
20 mM $(NH_4)_2SO_4$	80 ± 67	54 ± 52
2 mM $MgCl_2$	114 ± 99	46 ± 33
75 mM Tris-HCl	104 ± 75	69 ± 69
0.01% Tween 20	82 ± 78	60 ± 42

Table 2.1: Naked PtNP and PtNP@ssDNA sizes in Taq buffer and Taq buffer components

ECA of PtNP@ssDNA at Au UMEs after Exo I Digestion

We are interested in the catalytic properties of PtNP@ssDNA after exposure to Exo I, because (as discussed in the Introduction) reactivation of the NPs provides a means of using ECA for biosensing applications. Accordingly, PtNP@ssDNA was incubated with 30 U of Exo I for 1.0 h at 37 °C. **Figure 2.7a** shows ECA *i-t* traces for collisions of PtNP@ssDNA with a Au UME before (black trace) and after (red trace) Exo I digestion. Prior to digestion, the PtNP@ssDNA produced very small (~1-2 pA, **Figure 2.7a** inset) and infrequent collisions. Some experiments, typically those carried out at PtNP@ssDNA concentrations <1 pM, produced no collisions at all. After Exo I digestion, which removes a

fraction of the ssDNA from the PtNP surface, the anodic background current (red trace) increases with time and step-shaped current transients, corresponding to NP collisions, are observed. This is apparent in the expanded view (**Figure 2.7b**) of a 10 s section of the *i-t* trace in **Figure 2.7a**.

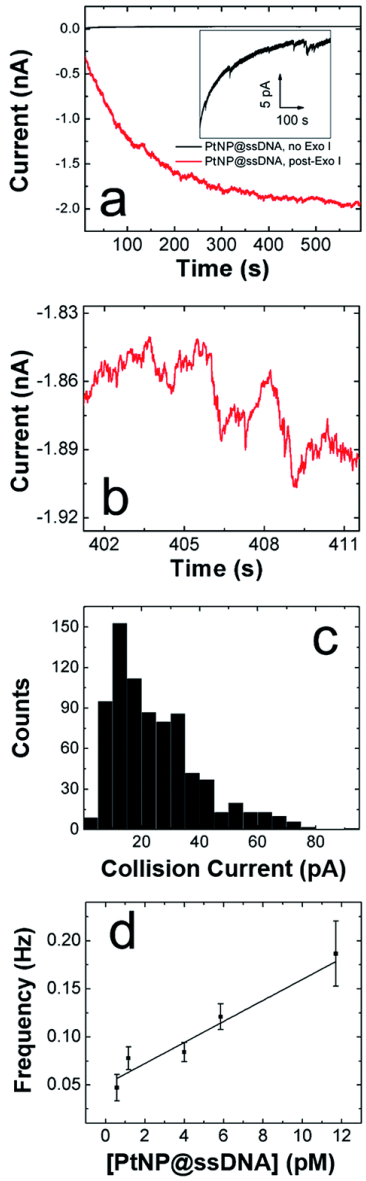

Figure 2.7: (a) *i-t* curves obtained at E = -50.0 mV for 11.7 pM PtNP@ssDNA before (black) and after (red) ssDNA digestion by Exo I. The inset shows an expanded view of the *i-t* trace before treatment with Exo I. (b) Expanded view of post-Exo I trace in frame a showing the step-shaped profile. (c) Histogram showing the distribution of currents for collisions of PtNP@ssDNA post-Exo I.(d) Plot of collision frequency as a function of the concentration of PtNP@ssDNA post-Exo I.

A histogram showing the frequency of collisions as a function of the ECA current is shown in **Figure 2.7c**. The average collision current for the post-Exo I PtNP-ssDNA is 24 ± 15 pA, which can be compared to the value for naked PtNPs: 51 + 41 pA. Because only about half of the original current is recovered after exposure to the enzyme, we conclude that only about that same fraction of the PtNP surface is available for N_2H_4 oxidation. The most likely scenario is that a substantial fraction of the ssDNA is reduced in length by Exo I, thereby providing access of N_2H_4 to the PtNP surface. We wish to emphasize that the ssDNA incorporates a 6-carbon alkylthiol on its 5′ (proximal) end. These alkyl chains will not be removed by Exo I, so it is unlikely that additional catalytic sites are exposed on the Pt surface. Rather, removal of some of bases reduces mass transfer hindrance of N_2H_4.

Exo I will only initiate cleavage in ssDNA having a free 3′-hydroxyl end. To confirm that the action of Exo I is responsible for the observation of collisions, we immobilized ssDNA on the PtNPs such that only the 5′-hydroxyl end was accessible. For this control experiment, only the orientation of the DNA on the PtNPs was reversed: the ssDNA sequence was unchanged. In this case, no collisions were observed after treatment with Exo I (**Figure 2.8**). This important finding confirms that the specific enzymatic activity of Exo I for

cleavage of 3′-hydroxyl DNA is responsible for the collision currents shown in **Figure 2.7.**

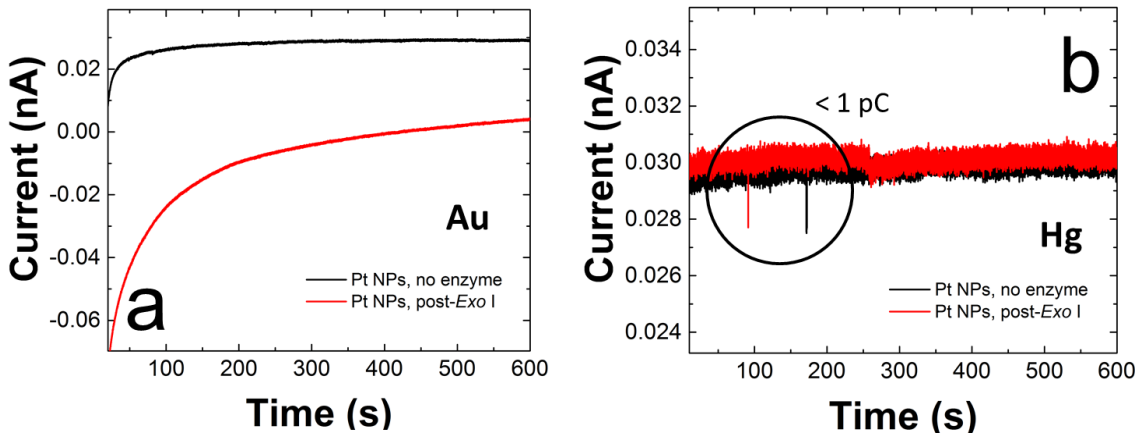

Figure 2.8: ECA results for collisions of PtNP@ssDNA modified with the thiol linkage on the 3′ end, post-Exo I digestion on Au (a) and Hg (b) UMEs. The solutions contained 50 mM PB + 10 mM N_2H_4 (pH 7). *i-t* traces in the absence (black traces) and presence (red traces) of 4 pM PtNPs@ssDNA, post-Exo I. No significant collision events were observed for either electrode material.

In addition to the collision current, we also studied the collision frequency for PtNP@ssDNA post-Exo I and found that it correlates linearly with concentration in the range of 0.58-11.7 pM (**Figure 2.7d**). This observation is consistent with previous findings for collisions of naked PtNPs at Au UMEs.[92] Here, we also found that the collision frequency is higher for PtNP@ssDNA post-Exo I than for naked PtNPs. For example, at a concentration of 11.7 pM, the frequency for PtNP@ssDNA post-Exo I was 0.190 ± 0.033 Hz, compared to 0.048 ± 0.006 Hz for naked PtNPs. We have observed this same trend

previously for ssDNA-modified PtNPs colliding with a Au microband electrode.[70]

The factor-of-three difference in collision frequency may be caused by the difference in the rates of mass transport between the slower diffusing aggregates of naked PtNPs and the smaller, more colloidally stable PtNP@ssDNA. Another observation worth considering is the high noise level observed for collisions arising from PtNP@ssDNA post-Exo I (**Figure 2.7b**). This might suggest that the ssDNA-modified NPs reside on or near the UME surface longer than naked PtNPs, and hence each particle may collide with the electrode multiple times.

ECA of PtNP@ssDNA at Hg UMEs

In an effort to better understand the difference in collision frequency between naked PtNPs and PtNP@ssDNA, we carried out additional ECA experiments using an Hg UME in place of the Au UME. We chose this comparison, because Hg has previously been shown to quickly deactivate, or ''poison'', PtNPs upon impact.[43] Therefore, each PtNP@ssDNA should only produce one collision signal. Collisions on Hg also provide the advantage of lower background noise, and each signal decays back to the original current baseline rather than producing a step-shaped response.[43]

Figure 2.9a shows *i-t* results for collisions of PtNP@ssDNA with an Hg UME before (black trace) and after (red trace) Exo I digestion of PtNP@ssDNA. The inset in this frame is an expanded view of the black trace over a limited time window. These data show that in the absence of Exo I exposure, PtNP collisions yield small and infrequent collisions having a magnitude of ~5 pC. Note that due to the spike-shaped *i-t* transients that occur at Hg UMEs, it is conventional to report their magnitude in terms of charge rather than current.[43] After enzymatic digestion, more frequent, spike-shaped collisions are observed as shown in the expanded view of the *i-t* trace in **Figure 2.9b**. Comparison of the red traces in **Figure 2.7a** (Au UME) and **2.9a** (Hg UME) also shows that the baseline current is much more stable for the latter after digestion.

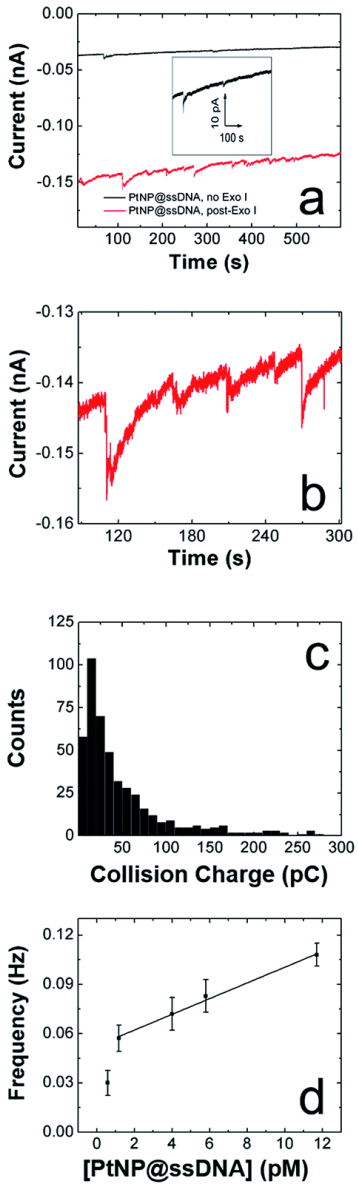

Figure 2.9: (a) *i-t* curves obtained at E = 5.0 mV for 1.17 pM PtNP@ssDNA before (black) and after (red) digestion by Exo I. The inset shows an expanded view of the i-t trace before treatment with Exo I. (b) Expanded view of post-Exo I trace in frame a showing the spike-shaped profile. (c) Histogram showing the distribution of charges for collisions of PtNP@ssDNA post-Exo I (d) Plot of collision frequency as a function of the concentration of PtNP@ssDNA post-Exo I.

Figure 2.9c is a histogram showing the frequency of collisions as a function of their magnitude for post-Exo I PtNP@ssDNA. The average collision charge for these experiments is 63 ± 98 pC, which is ~50% less than for naked PtNPs: 118 ± 128 pC. This trend of recovering roughly half the original collision signal is consistent with that observed for Au UMEs. Moreover, the broader distribution of collision charges (determined from the integrated current transients) on Hg is consistent with results reported by Stevenson and coworkers.[43]

The collision frequency of PtNP@ssDNA post-Exo I as a function of concentration at an Hg UME is shown in **Figure 2.9d**. As for the Au UME data (**Figure 2.7d**), this plot is linear over most of the concentration range studied. The interesting result, however, is that the collision frequencies are significantly lower at every concentration than for the Au UME results (**Table 2.2**). This finding is in contrast to previously reported observations in which the larger surface area of the hemispherical Hg UME led to higher collision frequencies.[95] It has been found previously that deposition of Hg on Pt yields a hemispherical Hg drop.[45] If we make that assumption here too, then the geometric surface area of the Hg electrode is 157 μm^2, compared to 123 μm^2 for the Au disk. In other words, the relative surface areas of the two electrodes do not account for the observation of

lower collision frequencies on the Hg UME. As suggested earlier, however, this difference might be due to specific interactions between the ssDNA-coated NPs and the Au UME that lead to multiple collisions per PtNP at the Au UME. In contrast, Hg deactivates every PtNP upon impact,[43] and thus each PtNP@ssDNA post-Exo I will only produce one current transient per collision event.

PtNP-ssDNA concentration (pM)	Frequency (Hz) Au UME	Frequency (Hz) Hg UME
0.5	0.047 ± 0.014	0.03 ± 0.08
1.17	0.077 ± 0.012	0.057 ± 0.008
4.0	0.084 ± 0.011	0.072 ± 0.010
5.8	0.12 ± 0.01	0.083 ± 0.010
11.7	0.19 ± 0.03	0.11 ± 0.01

Table 2.2: Collision frequency of post-Exo I PtNP@ssDNA conjugates at Au and Hg UMEs as a function of concentration

SUMMARY AND CONCLUSIONS

The method of ECA relies on access of a redox probe molecule, N_2H_4 in this study, to the surface of a catalytic NP. This fact has serious consequences for adaptation of ECA to biosensing applications, because in general the latter require surface modification with a recognition element such

as DNA or antibodies. In ECA, the presence of these recognition elements decreases the collision signal in proportion to their surface concentration.[70] To overcome this problem, we have introduced a new approach to ECA in which the colliding PtNP is pre-poisoned with the receptor (ssDNA in this case), but in the presence of an appropriate enzyme the catalytic properties of the PtNP are reactivated. In the present case, one can consider the target of this ''turn-on sensor'' to be either the ssDNA or the enzyme. As Corn and coworkers have shown,[96] there is a vast array of surface enzyme operations, and we believe that many of these could be adapted to the ECA methodology described herein. Hence, this approach could be quite general in resolving the apparent paradox of adapting ECA to biosensing applications.

Finally, there are three specific conclusions that can be drawn from the results presented here. First, PtNPs modified with ssDNA are not irreversibly passivated, and at least ~50% of the original current can be recovered after treatment with Exo I. Second, PtNP@ssDNA remain colloidally stable under the conditions required for enzymatic digestion (e.g., high salt concentration). Third, the lower collision frequency observed at Hg UMEs, compared to Au UMEs, may be indicative of single NPs producing more than one signal per collision event at Au electrodes. This is an important point, because practical applications of ECA require quantitative

correlation of the concentration of a target with the collision frequency and/or signal magnitude. These findings set the stage for biosensing applications of ECA, which will be explored in Chapter 3.

Chapter 3: Detection of microRNA by Electrocatalytic Amplification[2]

INTRODUCTION

Here we report electrochemical detection of microRNA (miRNA) using the method of electrocatalytic amplification (ECA).[3,29] ECA occurs when an electrocatalytic nanoparticle (NP) strikes a non-catalytic electrode surface in the presence of an appropriate redox-active molecule like N_2H_4. In this case, individual current steps[9] or peak-shaped[43] transients arise each time there is a collision.

The target in the present case is miRNA, and **Illustration 3.1** illustrates how we have adapted ECA to detect it. **Illustration 3.1a** shows a PtNP that has been surface modified with a monolayer of single-strand DNA (ssDNA). Due to the presence of the ssDNA coating, collisions between these PtNPs and the electrode surface do not result in current transients.[70] In **Illustration 3.1b**, miRNA, which is complementary to the immobilized DNA, is introduced to a solution containing the PtNP@ssDNA conjugate. This results in hybridization. Next, the PtNP@ssDNA:miRNA conjugate is incubated with duplex specific nuclease (DSN). DSN cuts ssDNA only when it is hybridized to complementary nucleic acids

[2] Castaneda, A.D.; Brenes, N.J.; Kondajii, A.; Crooks, R.M., Submitted for publication in *J. Am. Chem. Soc*. ADC was the primary author. NJB assisted with preliminary experiments, AK assisted with experiments on Hg electrodes, and RMC was the research advisor.

(**Illustration 3.1c**), and if the conjugate is a DNA:RNA hybrid it leaves the original RNA intact so that it can bind to another immobilized ssDNA (**Illustration 3.1d**). This process continues until sufficient ssDNA is removed from the PtNP that current transients are observed when the particles strike the electrode (**Illustration 3.1e**).

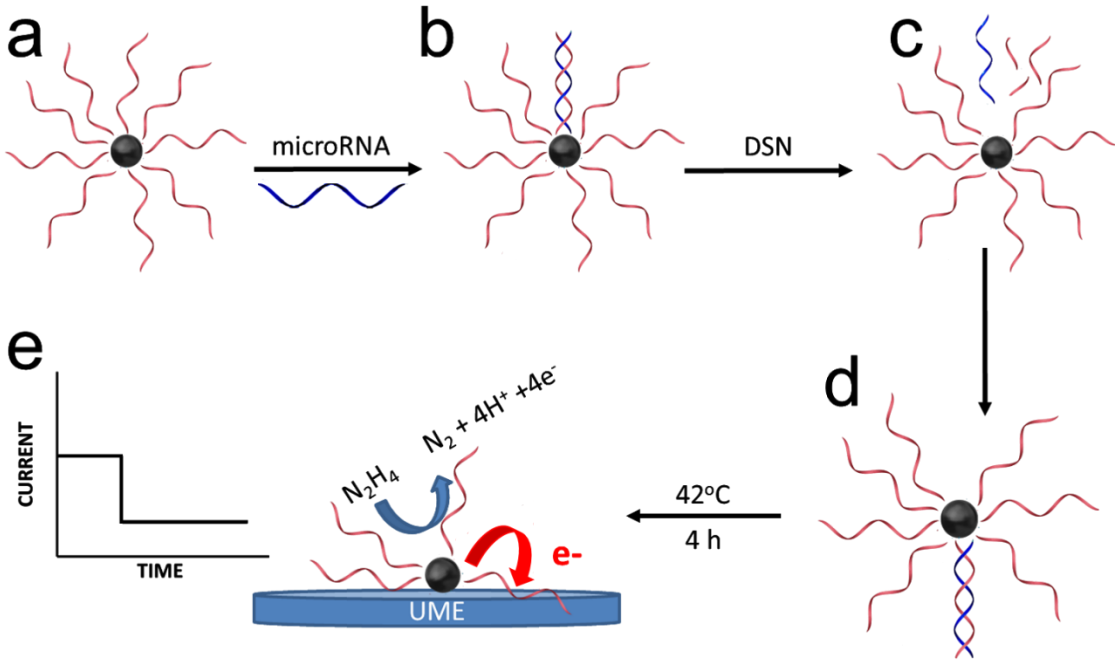

Illustration 3.1: Scheme demonstrating miRNA detection via ECA and DSN Cleavage

As alluded to earlier, NP-DNA conjugates do not exhibit current transients like those commonly observed for naked NPs. We have previously shown that when short ssDNA (5 nucleotides) are immobilized on PtNPs, small current

transients are observed, but longer ssDNA (25 nucleotides) nearly completely shuts off the electrocatalytic properties of the Pt surface completely.[42,70] Accordingly, we believe that the DNA coating prevents the NP from getting within electron tunneling distance of the electrode, or it prevents the required redox-active molecule (N_2H_4 in **Illustration 3.1**) from accessing the electrocatalytic Pt surface. Note, however, that it is unlikely that Pt sites specifically blocked by ssDNA attachment are responsible for the observed attenuated current. This is because only a fraction of the Pt atoms on the PtNP surface are in direct contact with a sulfur group (used for ssDNA immobilization). Additionally, much of the electrocatalytic activity of the PtNPs returns when DNA is removed, even though the hydrocarbon attachment linker is left behind after enzyme digestion.[42]

miRNA is noncoding RNA that typically has a length of 21-23 nucleotides. These short sequences are regulatory factors in various biological processes, and they play an active role in mRNA repression as well as in regulation of post-transcriptional gene expression regulation.[97] Dysregulation of the expression levels of one or more miRNAs is associated with various pathological diseases, including cancer, and therefore certain miRNAs may serve as important diagnostic biomarkers.[98] A few strategies in which NP-based assays were employed to detect miRNA levels have been

reported previously. For example, the Corn group developed an array platform for miRNA detection using universal DNA-functionalized AuNPs.[99] Similarly, Mirkin and co-workers developed a universal DNA-functionalized AuNP for detection of miRNA hybridization in an array.[100]

Here, we were particularly inspired by an assay reported by the Fiammengo group, in which they used AuNP-DNA probes and fluorescence spectroscopy for absolute miRNA quantification.[101] Specifically, they modified AuNPs with FAM-labeled probe ssDNA complementary to the miRNA of interest. In this configuration, the AuNP effectively quenched the fluorescence of FAM. After hybridization with target miRNA and subsequent incubation with DSN, however, the ssDNA was cleaved (as shown in **Illustration 3.1c**). This frees FAM from the proximity of the AuNP and eliminates quenching. The magnitude of the fluorescence signal was found to be correlated to the original concentration of miRNA. The limit of detection (LOD) of this assay was found to be 5 pM.

The specific miRNA target used by the Fiammengo group, and adopted by us, is hsa-miR-203 (miRNA-203). This is a low-abundance miRNA that is absent in nearly all organs except for the skin and esophagus, where it is expressed at relatively high levels. Up-regulation of miRNA-203 is found in psoriasis,[102] and it is differentially expressed in some cancers.[103,104] To cleave the ssDNA:miRNA conjugate we used DSN,

which is an endonuclease extracted from the red king (Kamchatka) crab hepatopancreas. It selectively cleaves double-stranded DNA and DNA in DNA:RNA duplexes. It is essentially inactive towards ssDNA and single- or double-stranded RNA.[105]

The general approach we have used for detection of DNA[42] and RNA by ECA has some attractive features. First, it is highly generalizable and applicable to many nucleic acid sensing tasks. Second, there is an intrinsic amplification step associated with using DSN to cleave the DNA:RNA duplex. Specifically, DSN will only digest DNA in DNA:DNA or DNA:RNA duplexes, and therefore (as shown in **Illustration 3.1d**) the liberated miRNA strand is free to bind with additional ssDNA on the same or different PtNPs. Due to the close proximity of DNA on a particular PtNP, this process is probably efficient. Third, the colloidal stability of the PtNP@ssDNA conjugates is much better than that of naked PtNPs, particularly in high-salt buffers.[89] Fourth, the method illustrated in **Illustration 3.1** is a "turn-on" sensor, because the original PtNP@ssDNA conjugates are electrocatalytically inactive. There are intrinsic advantages of turn-on sensors over turn-off sensors.[106]

In the present study, a 26-nucleotide ssDNA oligomer was immobilized on PtNPs through a linker consisting of a thiol group and a short alkyl chain. After hybridization with

target miRNA, current vs time (*i*-*t*) transients were recorded using either Au ultramicroelectrodes (UMEs) or Hg-modified Au[107] UMEs before and after exposure of the PtNP@ssDNA:miRNA conjugates to DSN. Prior to DSN exposure the NP conjugates produced insignificant collision signals, but after digestion the signals were recovered. Importantly, and as alluded to earlier, the PtNP@ssDNA:miRNA conjugates remained colloidally stable in both the N_2H_4 test solutions and the DSN reaction buffer. In contrast, nominally naked PtNPs rapidly agglomerated under these conditions, which is a major problem in normal ECA experiments.[88,89,108]

EXPERIMENTAL

Chemicals and Materials

$MgCl_2$, $(NH_4)_2SO_4$, Tris-HCl, $ZnCl_2$, glycerol, L-ascorbic acid, citric acid, $NaBH_4$, and $N_2H_4oH_2O$ were obtained from Sigma-Aldrich (St. Louis, MO). Sodium citrate and sodium phosphate monohydrate were from EM Science (Billerica, MA). $H_2PtCl_6o6H_2O$ (99.9%) was purchased from Strem Chemicals (Newburyport, MA). Tween 20 and NaCl were obtained from Fisher Scientific (Pittsburgh, PA). All reagents were used as received.

ssDNA (5′-CTA GTG GTC CTA AAC ATT TCA CTT T-(CH2)3-SH-3′, 5′-TAMRA-CTA GTG GTC CTA AAC ATT TCA CTT T-(CH2)3-SH-3′,

and 5′-TCA ACA TCA GTC TGA TAA GCT ATT T-(CH2)3-SH-3′), miRNA-203 (GUG AAA UGU UUA GGA CCA CUA G), miRNA-21 (UAG CUU AUC AGA CUG AUG UUG A, miRNA-203 single mismatch (GUG AAA UGU UUU GGA CCA CUA G), and miRNA-203 5-base mismatch (GUG AAA UGU AAU CCA CCA CUA G) were from Integrated DNA Technologies (Coralville, IA) and received as lyophilized pellets in microcentrifuge tubes. The excitation and emission wavelengths used for analysis of the TAMRA label were 546 nm and 579 nm, respectively. The pellets were centrifuged to ensure no residue on the walls or cap remained and then suspended in H_2O. DSN was purchased from Evrogen and received as a lyophilized enzyme. The pellet was diluted in the DSN storage buffer provided (5 µL of buffer for each 10 U DSN), gently vortexed, and incubated at 25 °C for 5 min. An equal volume of glycerol (for a final concentration of 50% glycerol) was added before the tube was gently vortexed and stored at -20 °C. Deionized (DI) water having a resistivity of 18.2 MΩocm was used for all experiments (Milli-Q gradient water purification system, Millipore, Bedford, MA). Experiments were conducted at room temperature (23 ± 2 °C). Unless otherwise stated, the phosphate buffer was adjusted to pH 7.0.

Synthesis and Characterization of PtNPs

PtNPs were synthesized following a previously reported seed-mediated method.[83] Briefly, 7.76 mL of 0.2% (w/v) H_2PtCl_6 were added to 100 mL of boiling H_2O and reacted for 1.0 min. Next, 2.37 mL of a 1% (w/v) sodium citrate and 0.05% (w/v) citric acid solution were added, and the Pt solution was boiled for 30 s. Finally, 1.18 mL of a solution containing 0.08% (w/v) $NaBH_4$, 1% (w/v) sodium citrate, and 0.05% (w/v) citric acid solution was added, and the solution was boiled for 10 min. After cooling to R. T. (25 °C), 3-4 nm Pt seed NPs were obtained.

Larger PtNPs were synthesized by adding 1.0 mL of the PtNP seed solution to 29.0 mL of H_2O at 25 °C. While stirring, 0.023 mL of 0.40 mL H_2PtCl_6 solution, 0.5 mL of 1% sodium citrate, and 1.25% L-ascorbic acid solution were added. The solution was then heated to boiling at the rate of 10 °C min^{-1}, with the total reaction time being 30 min. After cooling to ~25 °C, the solution was transferred to a 35 mm dialysis sack (12,000 Da MWCO, Sigma-Aldrich), where it was submerged in DI water for 24 h to remove excess salts. The PtNP size distribution was characterized by transmission electron microscopy (TEM, FEI Tecnai TEM). The average diameter was found to be 23 ± 3 nm. A representative image and size distribution histogram can be found in **Figure 3.1**.

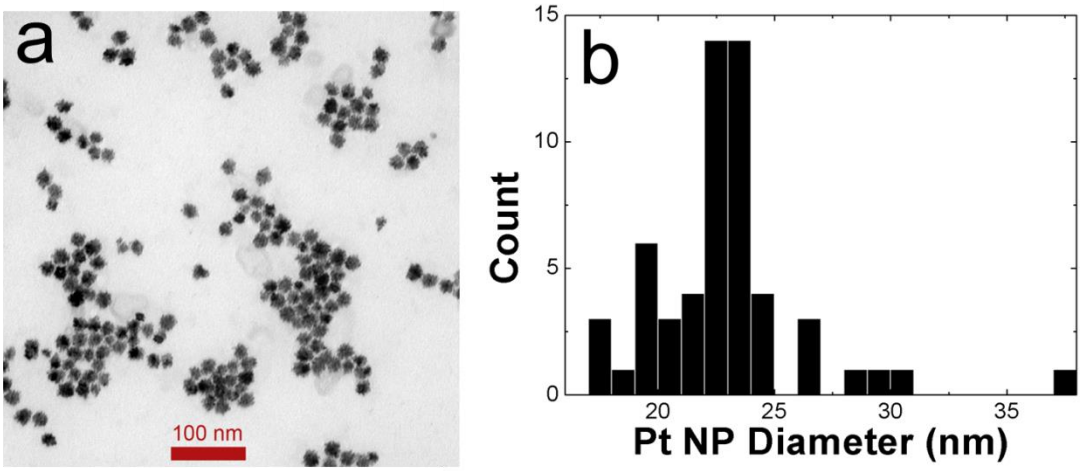

Figure 3.1: Transmission electron microscopy of PtNPs. (a) Representative TEM micrograph of the PtNPs used for the experiments described in Chapter 3. (b) Histogram showing that the size distribution of the PtNPs is 23 ± 2 nm.

Preparation of PtNP@ssDNA:miRNA Conjugates

PtNP@ssDNA conjugates were prepared using a pH-assisted conjugation method that was previously reported for AgNPs and AuNPs.[84,85] Specifically, 400 µL of the 445 pM PtNP solution were mixed with 5.0 µL of 100 µM ssDNA. After an incubation time of 5 min at 25 °C, 25.0 µL of 100 mM citrate-HCl buffer (pH 3) were added, the solution was mixed, and then it was allowed to rest for 5 min. Next, an additional 25.0 µL of citrate buffer were added, and the solution was incubated at 25 °C for 25 min, after which 400 µL of 100 mM HEPES buffer (pH 7.4) were added. The solution was then vortexed for ~5

s, centrifuged at 16.6 G for 20 min, washed 3 times, and resuspended in Taq buffer (75 mM Tris-HCl (pH 8.8), 2 mM $MgCl_2$, 0.01% Tween 20, and 20 mM $(NH_4)_2SO_4$). The miRNA strand of interest was then added at varying concentrations and allowed to incubate at 25 °C for 20 min.

DSN Cleavage of the PtNP@ssDNA:miRNA Conjugates

4 U of DSN were combined with 400 µL of the PtNP@ssDNA:miRNA solution in Taq buffer and the solution was vortexed for 5 s. The solution was then incubated at 42 °C for 4 h with gentle mixing at 200 rpm. Before carrying out electrochemical experiments, the assay solution was centrifuged at 16.6 G for 20 min, washed 3 times, and resuspended in H_2O. For all ECA experiments, 10 pM PtNP@ssDNA:miRNA were injected into N_2H_4 solutions.

Fluorescence Analysis

Fluorescence experiments using TAMRA-labeled PtNP@ssDNA were performed using a Fluorolog3 fluorimeter (Horiba, Kyoto, Japan) having a 450 W Xenon arc lamp excitation source. Samples were excited at 546 nm and emission was recorded at 579 nm.

UME Preparation

Au UMEs having a diameter of 12.5 μm were obtained from CH Instruments (Austin, TX). Au UMEs were polished by wet sanding for 1 min and then electrochemically cleaned by cycling 25 times between -0.35 V and 1.35 V vs Ag/AgCl (3.4 M KCl) in 0.5 M H_2SO_4 at 0.10 V s^{-1}. The Au UMEs were rinsed with H_2O and dried under a gentle stream of N_2 before use.

Au/Hg UMEs were prepared by electrodepositing Hg onto a Au UME according to a previous report.[107] Following the electrochemical cleaning procedure detailed above, Au UMEs were immersed in a Hg deposition solution consisting of 0.1 M $Hg(NO_3)_2$ acidified to pH 1.5 with HNO_3. Hg was then deposited by applying 0 V vs SCE for 3 min. The UME was removed from solution under potential control, rinsed with H_2O, and used immediately.

Electrochemistry

Chronoamperometric *i-t* curves were obtained in a two-electrode cell using a Chem-Clamp voltammeter-amperometer (Dagan Corp., Minneapolis, MN) potentiostat coupled to a PAR 175 Universal Function Generator (Princeton Applied Research, Oak Ridge, TN) to apply the voltage. The function generator and potentiostat were interfaced to a Dell Optiplex 380 computer using a PCI-6251 data acquisition board and BNC-2090A analog breakout accessory (National Instruments,

Austin, TX). The data were obtained using a custom LabView program (National Instruments). Data obtained using Au UMEs were obtained using a 15 ms sampling time, while for the Au/Hg UMEs the sampling time was 3 ms. All electrochemistry experiments were shielded from environmental noise by using a homemade Faraday cage constructed from copper plate and mesh. For *i-t* experiments, the potential was held at -50 mV and 0 mV vs SCE for the Au and Au/Hg UMEs, respectively. Unless otherwise stated, all potentials are reported vs SCE in sat'd KCl (CH Instruments, Austin, TX). The SCE reference electrode was fitted with a custom-made glass frit to prevent contamination of the electrolyte solution.

Nanoparticle Tracking Analysis

The colloidal stability of PtNP@ssDNA@miRNA pre- and post-DSN incubation was analyzed using nanoparticle tracking analysis (NTA, Malvern Instruments, Malvern, United Kingdom). NTA is a technique that uses the properties of particle Brownian motion and light scattering to measure the size distribution and concentration of colloid solutions.[109] Due to the low working concentration range of the instrument (< 1 pM), NP solutions were diluted to a final concentration of in the range of 0.5-1 pM. To account for the differences in

these concentrations, the data are normalized to the highest concentration observed for each species.

Results and Discussion

Synthesis and Characterzation of PtNP@ssDNA and PtNP@ssDNA:miRNA

As discussed in the Experimental Section, the PtNP@ssDNA conjugates were prepared using a fast, pH-assisted conjugation procedure.[84] To estimate the average number of ssDNA attached to each PtNP, we used a previously reported method.[42,87] Specifically, ssDNA functionalized on the 5' end with a TAMRA fluorescent label (ssDNA-TAMRA) was immobilized on PtNPs through a thiol group on the 3' end. The close proximity of TAMRA to the PtNPs following DNA immobilization is sufficient to quench its fluorescence. Therefore, following modification of PtNPs with ssDNA-TAMRA, any residual fluorescence in solution arises primarily from free ssDNA-TAMRA.

To determine the ssDNA-TAMRA coverage on PtNPs, a solution containing PtNP@ssDNA-TAMRA was prepared, and then it was centrifuged to leave only free ssDNA-TAMRA in the supernatant. The fluorescence of the supernatant was then compared to a calibration curve (**Figure 3.2**) to determine its concentration. Knowing the original concentrations of ssDNA-

TAMRA and PtNPs (determined by NTA), and the concentration of free ssDNA-TAMRA, a rough estimate of the average number of ssDNA-TAMRA on each PtNP can be determined by difference. The result is that there are ~10^3 ssDNA-TAMRA strands per 23 ± 3 nm PtNP.

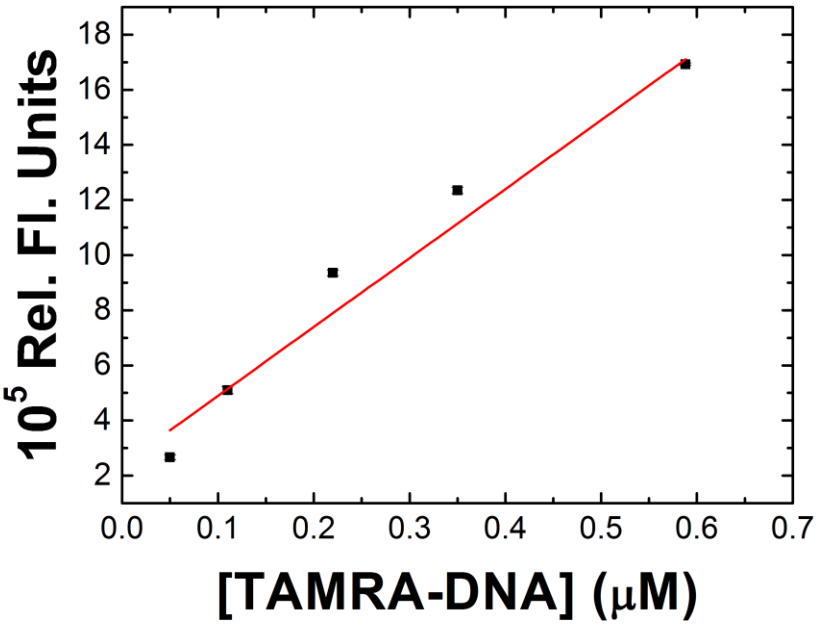

Figure 3.2: Fluorescence calibration curve for estimation of ssDNA coverage. Calibration solutions of ssDNA-TAMRA were prepared in Taq buffer at concentrations ranging from 0.05 - 0.59 μM. After PtNP@ssDNA-TAMRA conjugates were prepared, the fluorescence of the supernatant was measured, and linear regression was used to calculate the concentration of unbound ssDNA. The DNA coverage per PtNP was estimated to be ~10^3 DNA per PtNP.

It has previously been shown that aggregation of NPs is the most serious drawback of the ECA method.[89] Accordingly,

we assessed the colloidal stability of the PtNPs and PtNP conjugates under reaction conditions using NTA. These results are shown in **Figure 3.3a**. The NTA diameter for nominally naked PtNPs in H_2O is 26 ± 43 nm (black), compared to 23 ± 3 nm by TEM (**Figure 3.1a**). Results obtained in Taq buffer indicate a size distribution of 93 ± 69 nm for naked PtNPs (red), indicating that the higher ionic strength of the Taq buffer leads to aggregation.[89] After modification with ssDNA, however, the NTA size of the PtNP@ssDNA conjugates in Taq buffer is just 37 ± 56 nm (blue). This value is in good agreement with the calculated maximum size of a 23 nm PtNP core surrounded by a ssDNA shell (~39 nm), indicating a substantial reduction in NP aggregation.

Figure 3.3b shows that solutions containing PtNP@ssDNA:miRNA-203 are also stable before ("pre-DSN, Taq buffer", black trace) and after ("post-DSN, Taq buffer'', red trace) incubation with DSN for 4 h at 42 °C. The NTA sizes under these conditions are 32 ± 36 nm and 32 ± 120 nm, respectively. Following incubation with DSN, the PtNP@ssDNA:miRNA-203 conjugates were centrifuged and then resuspended in DI water ("post-DSN, H_2O'', blue trace), yielding colloidally stable solutions (NTA size = 34 ± 76 nm). The important point is that the average size of the PtNP conjugates is around 34 nm, regardless of the solution into which they are immersed, and they remain stable for

periods of hours. However, when the PtNP@ssDNA:miRNA-203 conjugates are suspended in 10 mM N_2H_4 + 50 mM PB after incubation with DSN (‘‘post-DSN, N_2H_4 + PB’’, green trace), which is the solution used for ECA measurements, the size increases slightly to 50 ± 29 nm, indicating some aggregation.[88]

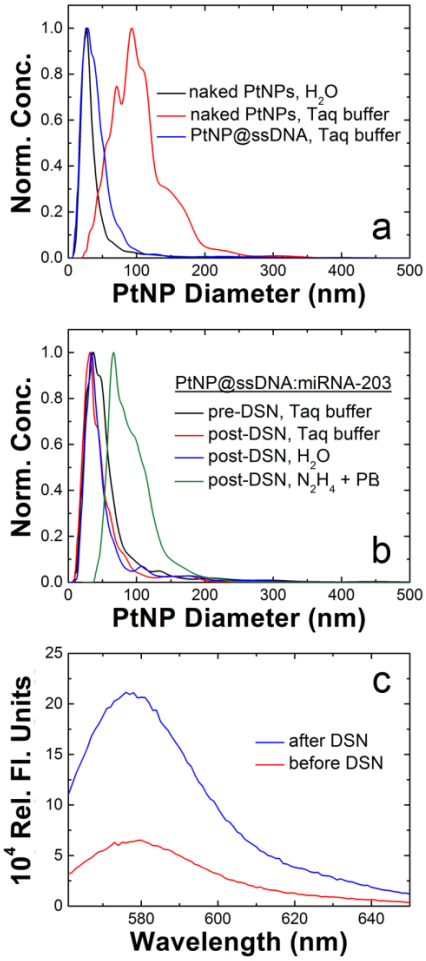

Figure 3.3: (a) Nanoparticle tracking analysis (NTA) showing the normalized concentration of PtNPs as a function of their diameter for naked PtNPs in water (black), naked PtNPs in Taq buffer (red), and PtNP@ssDNA in Taq buffer (blue). (b) NTA showing the normalized concentration of PtNP@ssDNA:miRNA-203 as a function of their diameter before exposure to DSN in Taq buffer (black), after exposure to DSN in Taq buffer (red), after exposure to DSN and then resuspension in DI water (blue), and after exposure to DSN in 10 mM N_2H_4 + 50 mM PB (green). (c) Fluorescence emission recorded at 579 nm for PtNP@ssDNA:miRNA-203 assay for TAMRA-labeled PtNP@ssDNA before (red) and after (blue) incubation with DSN.

Fluorescence Detection of miRNA-203

As previously mentioned, our DSN-based ECA assay is somewhat analogous to the fluorescence-based method reported by Fiammengo and coworkers.[101] There are, however, three significant differences: (1) the present work uses PtNPs rather than Au; (2) the PtNPs do not have a poly(ethylene glycol) (PEG) layer to increase their colloidal stability (a PEG layer would hinder ECA detection of PtNP collisions); and (3) the DSN reaction was performed in Taq buffer rather than DSN buffer. Taq buffer was preferable in this case because DSN buffer (50 mM Tris-HCl, pH 8.0, plus 5 mM $MgCl_2$, 1 mM DTT) rapidly induces aggregation and precipitation of the PtNP@ssDNA. The likely reason for this instability is the presence of DTT, which has been shown to undergo ligand exchange with thiolated DNA on metal NPs.[110] We have, however, shown previously that Taq buffer, which is free of DTT, is an appropriate reaction buffer for ECA experiments.[42]

A fluorescence-based assay was performed to test the viability of the aforementioned reaction conditions for miRNA detection. Specifically, PtNPs were modified with ssDNA-TAMRA, hybridized with 10 nM miRNA-203, and then incubated with DSN in Taq buffer. The results of this study are shown in **Figure 3.3c**. Here, the red and blue traces correspond to PtNP@ssDNA-TAMRA:miRNA-203 before and after incubation with DSN, respectively. After incubation, the fluorescence at 579

nm increases by 220%. As mentioned earlier in relationship to the work of the Fiammengo group,[101] this indicates that DSN cleaves DNA in the presence of miRNA and under the conditions used in the ECA experiments described next.

ECA Analysis on Au UMEs

Figure 3.4a shows typical *i-t* responses obtained when PtNPs are used for ECA experiments on Au UMEs. The black trace represents a control experiment and was obtained in a solution containing 10 mM N_2H_4 and 50 mM PB. In this case no PtNPs were present and no collision events (current transients) are observed. The red trace was obtained under identical conditions, but in this case 10 pM naked PtNPs were added to the solution. Each of the current transients here corresponds to a single PtNP (or most frequently an agglomerate of PtNPs) colliding with the electrode surface. These collisions produce step-shaped responses, indicative of NPs adsorbing to the electrode surface immediately after impact.[9] The average magnitude of the current steps is 69 ± 64 pA. This is consistent with previous findings wherein 22 nm PtNPs yielded collision currents of 51 ± 41 pA.[42] The blue trace was obtained using a solution containing 10 pM PtNP@ssDNA. The absence of current transients indicates that the ssDNA shell completely passivates the catalytic PtNP

surface. The green *i-t* trace shows that no collisions are observed when 10 pM PtNP@ssDNA are incubated in Taq buffer for 4 h at 42 °C in the absence of miRNA-203. This result indicates that the conjugate is stable in Taq buffer.

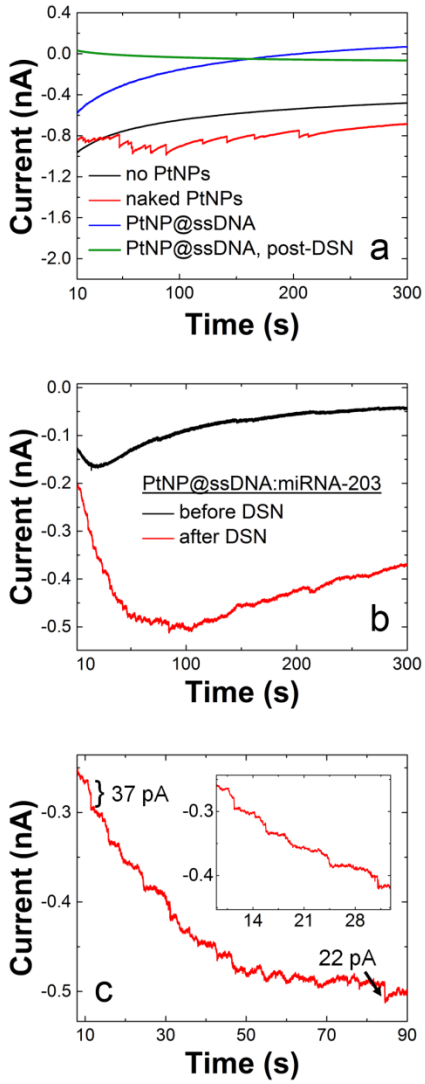

Figure 3.4: Au UMEs: (a) Current response before addition of PtNPs (black), after addition of 10.0 pM naked PtNPs (red), after addition of 10 pM PtNP@ssDNA (blue), and after addition of 10 pM PtNP@ssDNA that were incubated with DSN (green). (b) Current responses for 10 pM PtNP@ssDNA:miRNA-203 before (black) and after digestion by DSN (red). The PtNP@ssDNA:miRNA-203 conjugate was prepared using 1.0 µM miRNA-203. Digestion was carried out in Taq buffer at 42 °C for 4 h. (c) Expanded view of a section of the red trace in (b). The inset shows an even more expanded section.

We now turn our attention to collisions between PtNP@ssDNA:miRNA-203 and Au UMEs before and after exposure of the NPs to DSN. The black *i-t* trace in **Figure 3.4b** shows the response obtained for 10 pM PtNP@ssDNA:miRNA-203 that have been incubated in Taq buffer for 4 h at 42 °C, but in the absence of the DSN cleavage enzyme. No collision events are detected, indicating that the ssDNA:miRNA-203 shell is stable under the incubation conditions required for DSN activity. The red trace was obtained after adding 10 pM PtNP@ssDNA:miRNA-203 to the solution, but after incubation with DSN. In contrast to the black trace and the control experiments shown in **Figure 3.4a**, this *i-t* trace exhibits a rapid increase in anodic current during the first ~50 s of the experiment followed by a slow decrease. Additionally, small current transients, corresponding to collision events, are superimposed onto this slowly varying current.

An expanded view of the red trace in **Figure 3.4b** is presented in **Figure 3.4c**. Here, the step-shaped current transients, which have magnitudes of ~20-40 pA, are clearly apparent. These data confirm that hybridization of miRNA-203 to PtNP-ssDNA, followed by exposure to DSN, removes sufficient ssDNA from the surface of the PtNPs to reactivate electrocatalytic oxidation of N_2H_4. The magnitude of the current steps in **Figure 3.4c** is 28 ± 4 pA, which is about half that of nominally naked PtNPs (69 ± 64 pA). This recovery

of ~50% of the original current is consistent with that observed previously when Exonuclease I was used to remove ssDNA from PtNP-ssDNA.[42] Taken together, **Figures 3.4a-3.4c** conclusively prove that collision-induced current transients are only observed when all the conditions illustrated in **Illustration 3.1** are met.

ECA Analysis on Au/Hg UMEs

It is difficult to extract quantitative data from results like those shown in **Figure 3.4c** due to the steplike shapes of the current transients, their close spacing, and the sloping background current. To address these issues, we followed an approach previously reported by Stevenson and co-workers.[43] They showed that collisions at Hg-coated Pt UMEs yield sharp, peak-shaped current transients that quickly decay to baseline. This behavior has been attributed to rapid deactivation and poisoning of the Pt surface by Hg. Accordingly, we followed a literature procedure to prepare Au/Hg UMEs,[107] and then used them to detect miRNA.

Figure 3.5a shows typical *i-t* traces obtained using the same solution conditions as in **Figure 3.4** (10 mM N_2H_4 plus 50 mM PB), but in this case the UME is Au/Hg. The black trace are data for a control experiment in which PtNPs are absent. A key point here is that the background current is lower than

that observed using Au UMEs (compare to the black trace in **Figure 3.4a**), and the baseline current remains constant throughout the 300 s duration of the experiment. These observations are consistent with previous reports of ECA using Pt/Hg UMEs.[43-45]

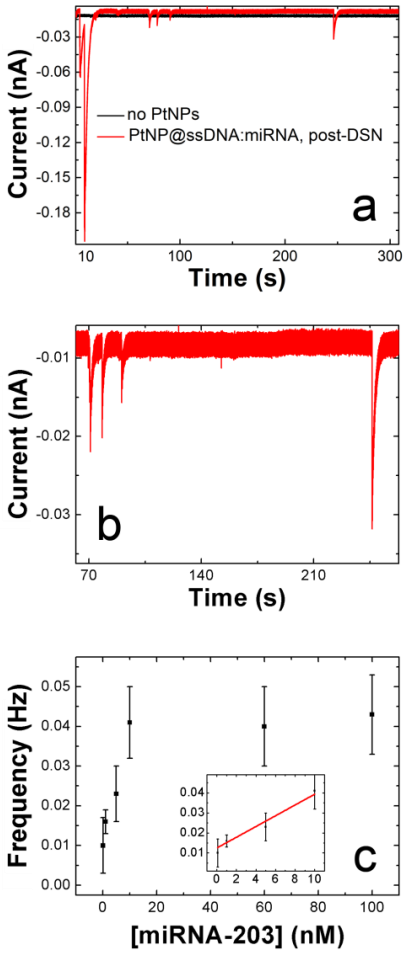

Figure 3.5: Hg UMEs: (a) Current response prior to the addition of PtNPs (black) and after addition of 10.0 pM PtNP@ssDNA:miRNA-203 after digestion with DSN (red). The PtNP@ssDNA:miRNA-203 conjugate was prepared by incubating PtNP@ssDNA with 10.0 nM miRNA-203. Digestion was carried out in Taq buffer at 42°C for 4 h. (b) Expanded view of a section of the red trace in (a). (c) Plot of collision frequency as a function of the concentration of miRNA-203 used to prepare the PtNP@ssDNA:miRNA-203 conjugate. All experiments were carried out after digestion of the conjugate with DSN using the same conditions as in (a). The inset is an expanded view of the linear part of this plot.

To demonstrate detection of miRNA using an Au/Hg UME, 10 pM PtNP@ssDNA were hybridized to miRNA using a 10 nM solution of miRNA-203, and then the resulting PtNP@ssDNA:miRNA-203 conjugate was incubated with DSN for 4 h. The resulting NPs were used to obtain the ECA results shown by the red trace in **Figure 3.5a**. Distinct current transients corresponding to N_2H_4 oxidation are present. An expanded view of a portion of this *i-t* trace is shown in **Figure 3.5b**, and it reveals that the current transients are spike-shaped rather than the stepped features observed using Au UMEs (compare to the inset in **Figure 3.4c**). These spike-shaped current transients are resolvable and their frequency is easily analyzed. For example, the collision frequency is 0.043 ± 0.01 Hz for the case when PtNP@ssDNA was incubated with 100 nM miRNA-203. This is a little more than half the collision frequency observed for naked PtNPs (0.07 ± 0.02 Hz) using Au/Hg UMEs. At the lowest detectable concentration of miRNA-203, 100 pM, the frequency drops to 0.010 ± 0.007 Hz. The magnitudes of the charge under the current transients for PtNP@ssDNA:miRNA-203 after DSN incubation is 54 ± 73 pC (for Hg-coated electrodes, it is customary to characterize current transients using the integrated charge under each peak)[43], which is comparable to that observed for naked PtNPs under identical conditions (127 ± 140 pC).

Figure 3.5c is a plot of the collision frequency of PtNP@ssDNA:miRNA-203 (after incubation with DSN) vs the concentration of the miRNA-203 concentration used for hybridization with PtNP-ssDNA. There are three interesting conclusions that can be derived from this plot. First, the collision frequency is a linear function of concentration over the range 0.10 - 10.0 nM miRNA-203 (inset of **Figure 3.5c**), and the lowest detectable concentration is 100 pM. Second, at concentrations of miRNA-203 above 10.0 nM the collision frequency is independent of concentration. This may be because we used less-than-optimal digestion conditions for the PtNP@ssDNA:miRNA-203 conjugate with DSN to ensure colloidal stability. Specifically, digestion was carried out in Taq buffer at 42 °C rather than DSN buffer at 60 °C,[111] and under these conditions the lower DSN activity may not be sufficient to cleave the higher concentration of conjugates present at elevated DNA:miRNA-203 concentrations. Third, the error bars, which represent the standard deviation from the mean for three independent experiments, are rather large, particularly at the higher concentrations. We believe this level of variation is intrinsic to collision measurements obtained over the limited time scale (typically 300 s) used in such experiments.

To test the specificity of this ECA-based miRNA sensor, we conducted studies using miRNA-203 analogs having one and

five mismatched nucleotides (**Figure 3.6**). The single mismatch nucleotide was placed in the middle of the miRNA strand; specifically, adenine was replaced with uracil at position 12 from the 5′ end. For this experiment, a 10.0 nM solution of the mismatched miRNA-203 was incubated with PtNP@ssDNA, followed by cleavage with DSN for 4 h at 42 °C. Except for the mismatch, these conditions are identical to those used to obtain the data shown in **Figure 3.5**. The results (**Figure 3.6a**) indicated no collision signatures in the *i*-*t* trace. We also tested a five-base mismatched analog of miRNA-203 and found the same result (**Figure 3.6b**). These key control experiments demonstrate the high degree of specificity of this ECA biosensing strategy.

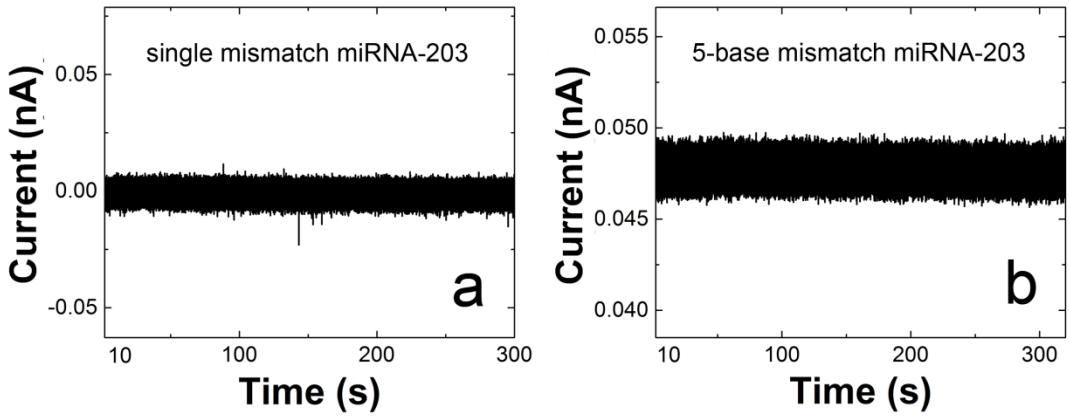

Figure 3.6: ECA results for miRNA-203 mismatch studies. The concentration of the mismatch strands used for conjugation to PtNP@ssDNA was 10 nM. The *i-t* curves were obtained at 0 mV using a Au/Hg UME in a solution containing 50 mM PB + 10 mM N_2H_4. Current responses for (a) one mismatch (GUG AAA UGU UUU GGA CCA CUA G) and (b) five mismatches (GUG AAA UGU AAU CCA CCA CUA G) following exposure of the conjugates to DSN. No collisions are observed.

Detection of miRNA-21

We confirmed the generality of this ECA detection method using a second target: miRNA-21, which is one of the most frequently over-expressed miRNAs in solid tumors including non-small cell lung,[112] breast,[113] and pancreatic cancers.[114] The miRNA-21 detection process was analogous to that used for miRNA-203: PtNPs were modified with ssDNA complementary to miRNA-21, the resulting conjugates were hybridized to varying concentrations of miRNA-21, and then the complex was exposed

to DSN for 4 h at 42 °C. The resulting ECA current transients obtained using Au/Hg UMEs are shown in **Figure 3.7.**

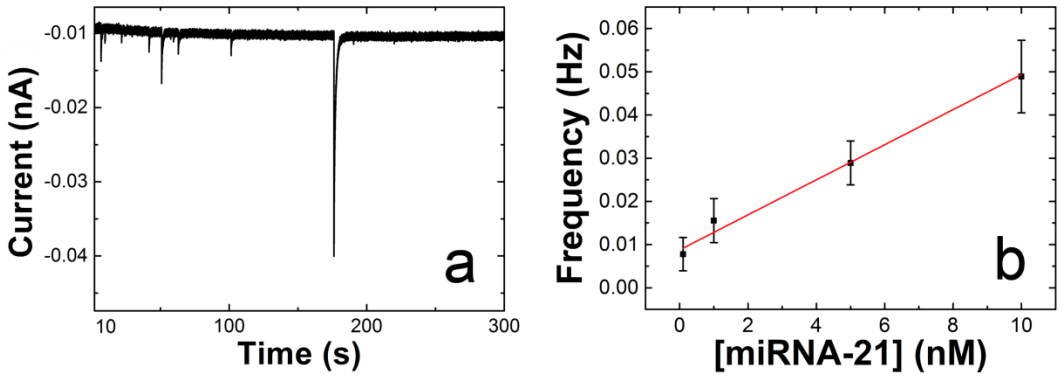

Figure 3.7: ECA results (*i-t* plots) obtained using Au/Hg UMEs and a solution containing 50 mM PB + 10 mM N_2H_4. The electrode potential was set to 0 mV. The data were obtained for the PtNP@ssDNA:miRNA-21 conjugate after digestion with DSN. The conjugate was prepared by incubating PtNP@ssDNA with miRNA-21, followed by digestion in Taq buffer with 4 U DSN at 42 °C. (a) Current responses obtained for the PtNP@ssDNA:miRNA-21 prepared by incubation with 10 nM miRNA-21 followed by DSN digestion. (b) Plot of collision frequency as a function of the concentration of miRNA-21 used to prepare the conjugate. The error bars represent the standard deviation from the mean for current transients obtained from three independent experiments at each concentration. Note that the range of concentrations here is more limited than in **Figure 3.5c.**

Figure 3.7a is an example of an *i-t* trace for 10.0 nM miRNA-21 revealing discrete current transients. **Figure 3.7b** is a compilation of data derived from experiments like that shown in **Figure 3.7a** but using several different miRNA-21

concentrations. The results are very similar to those obtained for miRNA-203 in that the linear range extends from 0.10 to 10.0 nM miRNA-21 and the lowest detectable concentration is 100 pM. For both miRNA sequences, the average number of collision events at 100 pM was ~3. The similarity of the frequency-vs-concentration results for miRNA-201 and miRNA-203 suggest that these detection levels are characteristic for this methodology.

Summary and Conclusions

We have reported an ECA-based approach for detection of miRNA. The results are for a specific application (detection of miRNA), but the method seems to be rather general. Accordingly, there are a number of key lessons learned from the present results, and our earlier ECA study involving DNA detection,[42] that are worth summarizing. For example, as has been extensively reported,[88,89,115] ECA suffers from uncontrollable aggregation of NPs. This unfortunate situation is a consequence of two factors that are mutually exclusive. First, collisions are only observed if the NP surface is accessible to the redox probe. Second, ECA requires the presence of buffer solutions to control pH and provide a conductive medium for electrochemical measurements. The requirements of using solutions having a significant ionic

strength and nominally naked metallic NPs inevitably leads to aggregation. In the present study, we showed that addition of a ssDNA shell to the NP eliminates aggregation. Catalytic sites on the NP surface are then rendered accessible by partial removal of this shell.

The second innovation is closely related to the first. It is well known in analytical chemistry that "turn-on" sensors are preferable to "turn-off" sensors.[106,116,117] The ECA approach we report is a "turn-on" method in that the collision signatures are initially silenced by the presence of the DNA shell, and only in the presence of the target are current transients manifest. The third key point is that in the particular case reported here, there is an intrinsic form of signal amplification. That is, each miRNA enables cleavage of many ssDNA oligonucleotides from the PtNP surface. Moreover, an individual miRNA probably has an extended residence time in the vicinity of a particular PtNP due to the high local surface concentration of ssDNA. This minimizes the time required for each hybridization/cleavage step (**Illustration 3.1**).

The fourth outcome of this study is perhaps the most important: this ECA method is robust, fairly simple to implement, and probably applicable to any biosensing method in which enzymes can be used to selectively cleave DNA in the presence of a target. As Corn has demonstrated over a period

of many years,[71,72,96,99,118-120] there is a seemingly endless number combinations of nucleic acids and enzymes that can be used to identify targets. Many of these should be useful for ECA biosensing.

The present findings set the stage for future biomolecule sensing applications of ECA. It may be possible, for example, to extend this general approach to detection of peptides or proteins.

Chapter 4: Electrocatalytic Amplification of Nanoparticle Collisions at Electrodes Modified with Polyelectrolyte Multilayer Films[3]

INTRODUCTION

We report electrochemical detection of collisions between individual Pt nanoparticles (PtNPs) and Au ultramicroelectrodes (Au UMEs) modified with passivating polyelectrolyte multilayer (PEM) films prepared using the layer-by-layer deposition method.[121,122] The important new result reported here is that, in addition to naked electrode surfaces, these collisions can be detected through PEM films having thicknesses of up to ~5.3 nm, which is well beyond normal electron tunneling distance. Interestingly, electrocatalytic reactions between negatively charged PtNPs and PEMs can be activated and deactivated by controlling the charge on the final layer of the film. Specifically, when the outermost layer is composed of cationic poly-l-lysine (pLL), current transients corresponding to collisions are observed, but when the charge is reversed by addition of a layer of poly-l-glutamic acid (pGA), current transients are effectively turned off. This observation of chemical control

[3] Castañeda, A. D.; Alligrant, T. M.; Loussaert, J. A.; Crooks, R. M. Electrocatalytic *Langmuir* **2015**, 31, 876-885. ADC was the primary author. TMA and JAL assisted with design of preliminary experiments. RMC was the research advisor.

over collisions may provide a means for developing chemical sensors based on ECA.

To date, most ECA experiments have involved naked electrode surfaces, but chemically modified electrodes have also been examined. For example, Bard and co-workers[14] demonstrated that the amplitude of current transients arising from collisions is attenuated when a Au electrode is modified with a carboxyl-terminated n-alkylthiol self-assembled monolayer (SAM). Specifically, they observed a negative logarithmic correlation between catalytic current and the number of carbons in the alkyl chain. For example, a 12-mercaptodecanoic acid-modified UME yielded current steps of just ~5 pA, which can be compared to a naked Au surface where current transients were on the order of ~60 pA. More recently, the Bard group also reported on collisions between Pt NPs and Pt UMEs modified with a thin, insulating film of TiO_2.[18]

The studies reported here were motivated by the work of the Allongue[123] and Fermín groups.[124] Specifically, the Fermín group used the LbL deposition method to prepare pinhole-free films containing pLL and pGA on Au electrodes.[124] These polymer layers were sufficiently thick that little or no electron transfer was observed between the electrode and a molecular redox probe in solution. However, when the surface of the film was modified with Au NPs, facile electron transfer was turned on even through films as thick as 6.5 nm. They

interpreted this result in terms of the increased tunneling probability between the electrode and the high density of states of the adsorbed NPs (compared to that of molecules), as previously predicted by Allongue and co-workers.[123] These results have since been confirmed by other groups using a variety of intervening organic materials and conductive NPs.[125-130]

In the present work, we modified 12.5 µm diameter Au UMEs with an 11-mercaptoundecanoic acid (MUA) SAM, followed by immobilization of alternating layers of pLL (positively charged) and pGA (negatively charged) (**Illustration 4.1**). Because the citrate capping agent on the PtNPs is deprotonated at pH 7, the NPs can be electrostatically adsorbed to films having a pLL terminating layer.[124] Accordingly, collisions between the PtNPs and the polymer layer result in transients in current-time (*i*-*t*) traces for the SAM-pLL- and SAM-pLL-pGA-pLL-modified UMEs. In contrast, no collisions resulting in significant current transients are observed on the SAM-pLL-pGA-modified UMEs, likely due to electrostatic repulsion between negatively charged groups in the films and the citrate capping agent on the PtNPs. The important point is that collisions can be switched on and off using chemical interactions, and we believe this will form the basis for chemical sensing using the ECA approach.

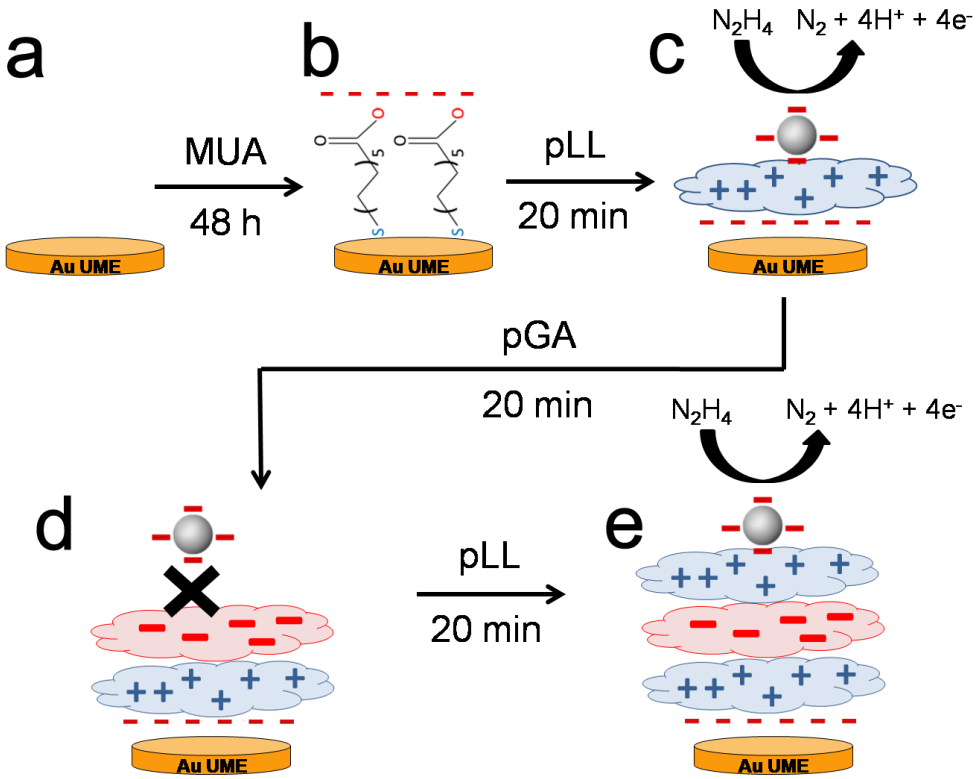

Illustration 4.1: Scheme showing ECA on PEM-modified Au UMEs

EXPERIMENTAL

Chemicals and Materials

1-Mercaptoundecanoic acid (95%), pGA (MW 100 000–150 000), l-ascorbic acid, citric acid, $NaBH_4$, and $N_2H_4 \cdot H_2O$ were purchased from Sigma-Aldrich (St. Louis, MO). pLL (MW 30 000–70 000) was purchased from MP Biomedicals (Santa Ana, CA). Sodium citrate and sodium phosphate monohydrate were purchased from EM Science (Billerica, MA). $H_2PtCl_6 \cdot 6H_2O$

(99.9%) was purchased from Strem Chemicals (Newburyport, MA). Au-coated glass slides were purchased from Evaporated Metal Films (Ithaca, NY). Deionized water having a resistivity of 18.2 MΩcm was used for all experiments (Milli-Q gradient water purification system, Millipore, Bedford, MA). All reagents were used as received. Experiments were conducted at room temperature (23 ± 2 °C). Unless otherwise stated, the phosphate buffer was adjusted to pH 7.

Synthesis of PtNPs

PtNPs were synthesized using a previously reported seed-mediated procedure.[83] Briefly, 7.76 mL of a 0.2% (w/v) solution of H_2PtCl_6 was added to 100 mL of boiling H_2O. The solution was boiled for 1 min before addition of 2.37 mL of a solution containing 1% (w/v) sodium citrate and 0.05% (w/v) citric acid. After 30 s, 1.18 mL of a solution containing 0.08% (w/v) $NaBH_4$, 1% (w/v) sodium citrate, and 0.05% (w/v) citric acid was quickly injected. The solution was boiled for 10 min and subsequently cooled to ~25°C to yield 3.6 nm diameter Pt seed NPs. To synthesize larger NPs, 1.0 mL of the Pt seed solution was added to 29.0 mL of H_2O at ~25°C. While the solution was being stirred, 0.023 mL of a 0.40 M H_2PtCl_6 solution and 0.50 mL of a solution containing 1% sodium citrate and 1.25% l-ascorbic acid were added. The temperature

of the solution was increased to the boiling point (100 °C) at a rate of 10 °C min-1. The total reaction time was 30 min. Next, the solution was transferred to a 35 mm dialysis sack (12 000 Da MWCO, Sigma-Aldrich) and submerged in 4 L of H_2O for 24 h to remove excess salts. Lastly, the resulting NPs were characterized by transmission electron microscopy (TEM, FEI Tecnai Spirit BioTwin, 80 kV). The average particle diameter was 57 ± 10 nm. A representative TEM image and a histogram showing the NP size distribution are shown in **Figure 4.1**.

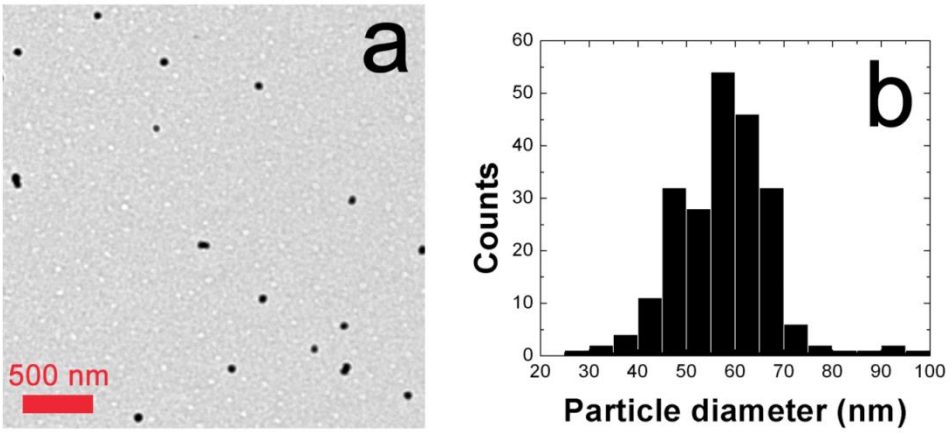

Figure 4.1: (a) Representative TEM image of the citrate-capped PtNPs used in this study. (b) Histogram showing the size distribution of the Pt NPs. The average size is 57 ± 10 nm.

A ζ-potential analysis is shown in **Figure 4.2**.

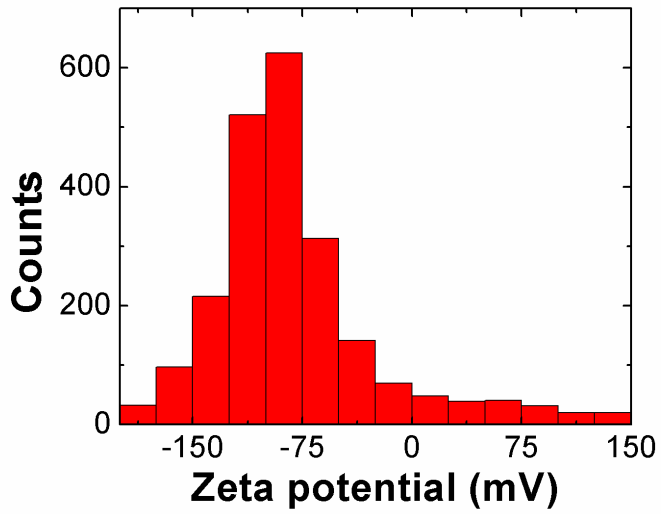

Figure 4.2: Histogram showing the zeta potential of the PtNPs as determined by Nanosight particle tracking analysis (Nanosight Model NS500, Malvern Instruments Ltd., United Kingdom). The average zeta potential is -59 ± 20 mV. The measurement was obtained in an aqueous solution containing ~1.28 pM PtNPs.

Electrode Modification with MUA

Au UMEs (12.5 µm) were polished via wet sanding for 1 min. The UMEs were then immersed in piranha solution (1:3 30% H_2O_2/H_2SO_4) for 30 s and thoroughly rinsed with water. ***Caution!*** *Piranha solution can react violently with organic compounds and should be handled with care.* Next, electrochemical cleaning of the polished Au UME was performed by cycling the potential between −0.35 and 1.35 V versus Ag/AgCl (3.4 M KCl) for 25 cycles at 0.3 V s^{-1} (CH potentiostat model CH 700D, CH Instruments, Austin, TX). The electrodes were then rinsed

with water and dried with a gentle stream of N_2. Lastly, the UMEs were immersed in a 10 mM ethanolic solution of MUA for 48 h and then rinsed with ethanol and water.

LbL Deposition of PEM Films

The first layer of pLL was deposited on a MUA-modified UME by incubating the electrode in a 0.5 M NaCl solution containing 2 mg$\cdot$mL^{-1} of pLL for 20 min, followed by rinsing with water. To deposit a second layer of pGA, the UME was incubated in a 0.5 M NaCl solution containing 2 mg$\cdot$mL^{-1} of pGA for 20 min. The deposition of the two oppositely charged polymers was repeated until the desired number of layers was obtained. The terminating polymer determined the net charge on the surface of the LbL-modified UMEs.[121,131] The thicknesses of the polymer layers were determined using spectroscopic ellipsometry (J.A. Woollam M2000 model, Lincoln, NE). Because of the small size of the electrodes, ellipsometric measurements were made on Au-coated glass slides.

Electrochemistry

Au UMEs having a diameter of 12.5 µm were purchased from CH Instruments (Austin, TX). Cyclic voltammograms (CVs) and *i-t* curves were obtained in a two-electrode cell, contained within a Faraday cage, and using a Chem-Clamp voltammeter-

amperometer (Dagan Corp., Minneapolis, MN) as the potentiostat. The applied voltage was generated by a PAR 175 Universal Function Generator (Princeton Applied Research, Oak Ridge, TN). The potentiostat and function generator were interfaced to a Dell Optiplex 380 computer through a PCI-6251 data acquisition board (National Instruments, Austin, TX) using a BNC-2090A analog breakout accessory (National Instruments, Austin, TX). The voltammetric and *i-t* measurements were performed using a custom LabView program (National Instruments), and the sampling time was 0.015 s. The Faraday cage was constructed from copper plate and mesh. Square wave voltammetry (SWV) was performed using a CH Instruments Model 650c potentiostat in a 3-electrode cell with a Pt wire serving as the counter electrode. SWV parameters: frequency, 390 Hz; incremental voltage, 5 mV; amplitude, 50 mV; and quiet time, 2 s. All potentials reported in this paper are referenced to a Ag/AgCl ''leakless'' reference electrode (3.4 M KCl, model 66-EE009, Dionex, Bannockburn, IL).

RESULTS AND DISCUSSION

UME Modification

The objective of this study is to better understand the nature of collisions between negatively charged PtNPs and

electrode surfaces modified with coatings having permanent positive and negative charges. The electrode modification process used to achieve the necessary experimental construct is outlined in **Illustration 4.1** and described in detail in the Experimental Section. The insulating layer is formed by immersing a 12.5 µm diameter Au UME (**Illustration 4.1a**) in 10 mM MUA to yield a SAM (**Illustration 4.1b**). The terminal carboxylic acid group of the MUA monolayer is deprotonated and negatively charged at neutral pH (MUA surface pKa, 5.7),[132] providing a foundation on which to deposit the first layer of positively charged pLL (**Illustration 4.1c**). Addition of a layer of negatively charged pGA reverses the net charge on the electrode surface (**Illustration 4.1d**), and the charge on the outermost layer can be reversed again by addition of a second pLL layer atop the pLL-pGA-modified UME (**Illustration 4.1e**).

SAM-Modified Au UMEs

Figure 4.3a presents CVs recorded at a naked Au UME (black trace) and the same UME after modification with MUA (red trace) in a solution containing 10 mM N_2H_4 and 50 mM PB (pH 7.0). In the presence of N_2H_4, the characteristic behavior of the N_2H_4 oxidation reaction on Au is apparent (onset potential, ~−0.15 V).[9] After modification with MUA, however,

the decrease in the limiting current from ~80 to ~0.6 nA (inset, **Figure 4.3a**) indicates that the electrode surface is passivated. This decrease corresponds to a faradaic current suppression of ~99%. The onset potential for the oxidation reaction also shifts in the positive direction by ~200 mV, indicating increased resistance due to the presence of the SAM. Although a high level of passivation is achieved after deposition of MUA, the shape of the red CV remains sigmoidal (inset), indicating the presence of pinholes in the film.[133,134] The thickness of the SAM was determined to be ~1.7 nm using ellipsometry on Au-coated glass slides (used as surrogates for the UMEs, which are too small for ellipsometric measurements), which corresponds well to literature values.[135-137]

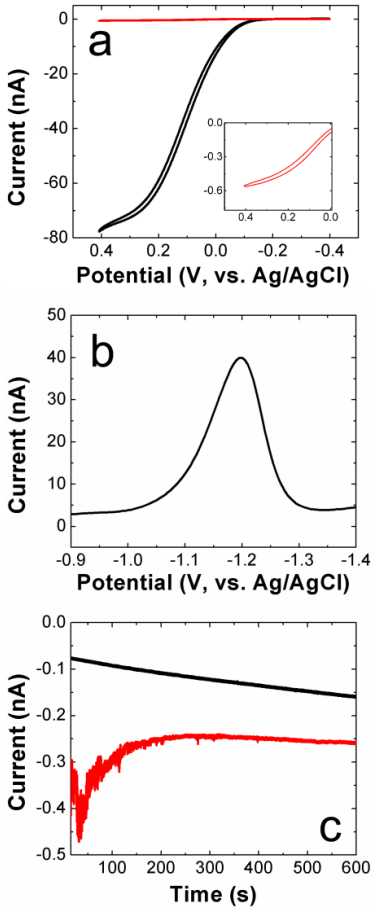

Figure 4.3: (a) CVs showing N_2H_4 oxidation at naked (black) and MUA-modified (red) 12.5 µm Au UMEs (no PtNPs present). The inset shows an expanded view of the limiting current at the MUA-modified UME. CVs recorded at 50 mV s^{-1}; 10.0 mM N_2H_4 in 50 mM PB (pH 7). (b) Square wave voltammetry (SWV) characteristic of electrochemical removal of MUA from the electrode surface. SWV parameters: 0.5 M KOH, 390 Hz frequency, 5.0 mV step increments, and 50 mV amplitude. (c) *i-t* curves obtained at +400 mV for a MUA-modified UME recorded in a solution containing 10.0 mM N_2H_4 and 50 mM PB (pH 7) in the absence (black) and presence (red) of 2.5 pM PtNPs.

Square wave voltammetry (SWV) was used to estimate the surface coverage of the SAM (**Figure 4.3b**). The thiol desorption wave is centered at −1.2 V, which is consistent with previous findings.[138] The surface coverage can be calculated from the peak current in **Figure 4.3b** using **equation 4.1**.[139]

$$i_p = 500A\alpha n^2 Faf\Delta E\Gamma \quad (4.1)$$

Here, i_p is the current amplitude, A the area of the electrode, α the transfer coefficient (α = ~0.5, values for thiol desorption on Au range from 0.4 to 0.84),[140,141] n the number of electrons (n = 1), F Faraday's constant (96485 C mol-1), a the square wave amplitude (0.05 V), f the applied frequency (390 Hz), ΔE the potential scan increment (5.0 mV), and Γ the surface coverage. On the basis of this analysis, Γ = 6.1 ± 2.0 × 10-10 mol cm^{-2}, which is consistent with previous reports.[142,143]

After modification with MUA, collision experiments were performed in solutions containing 10 mM N_2H_4, 50 mM PB (pH 7), and Pt NP concentrations of 2.5, 5.0, 7.5, 10.0, and 12.5 pM. These experiments were carried out with the working electrode potential set to E = 400 mV because this value was determined to yield the largest current steps for the pLL and pLL-pGA-pLL systems discussed later. **Figure 4.3c** shows a representative *i-t* curve in the absence (black) and presence (red) of 2.5 pM Pt NPs. The current response in the absence

of Pt NPs remains essentially constant at around −0.1 nA. Addition of Pt NPs to the system yields the appearance of small (<10 pA), spike-shaped current transients, indicating that the NPs may not be residing near the electrode long enough to stick to the exposed surface. This is in contrast to the result obtained for a naked Au UME, where NPs colliding and adsorbing to the surface yield step-like current transients.[9] The small amplitude of the transients is consistent with previous results obtained using an acid-terminated SAM.[14] Because the current transients for this system are very small, further analysis of their size and frequency were not conducted. Results similar to **Figure 4.3c** were also observed for Pt NP concentrations of 5.0, 7.5, 10.0, and 12.5 pM, and are shown in **Figure 4.4**.

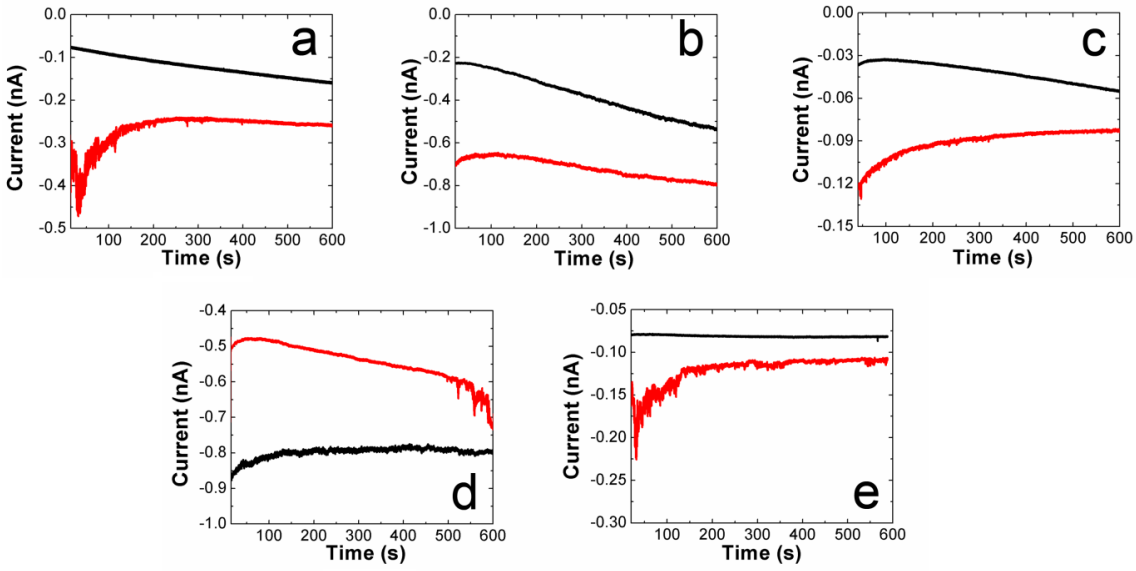

Figure 4.4: *i-t* traces showing current transients resulting from collisions between Pt NPs and MUA-modified UMEs. The solution contained 10.0 mM N_2H_4 and 50 mM PB (pH 7). Plots show the change in current in the absence (black) and presence (red) of (a) 2.5 (a), 5 (b), 7.5 (c), 10 (d), and 12.5 (e) pM PtNPs.

Characterization of PEM Films

The thicknesses and permeability of PEM film layers depends on a number of parameters, including the molecular weight of the polymers, pH, deposition time, and the type and concentration of electrolyte used in the LbL deposition solutions.[144] Although the generally accepted model for films formed via LbL is that the charge of the deposited polyelectrolyte overcompensates the charge of the previous layer,[121] the Schlenoff group has recently reported that this charge reversal is likely asymmetrical.[145] High salt concentrations have been shown to stabilize alternately

charged layers, resulting in thicker films;[146] therefore, 0.50 M NaCl was chosen for deposition of the LbL films used here. The growth of the LbL films on Au was monitored by ellipsometry up to n = 10, where n is an individual layer of either pLL or pGA (at n = 10, the terminating layer is pGA). The resulting total thicknesses are given in **Figure 4.5**. The thicknesses of the pLL, pLL-pGA, and pLL-pGA-pLL films used for collision studies were 0.5, 1.7, and 3.3 nm, respectively. These values do not include the MUA underlayer, which was previously found to be 1.7 nm in height. Notably, the thickness of each successive layer increases with n. This behavior is characteristic of the LbL process.[147] The total thickness at n = 10 (23.3 nm) is consistent with that of a similar pLL-pGA system studied by Corn and co-workers.[148]

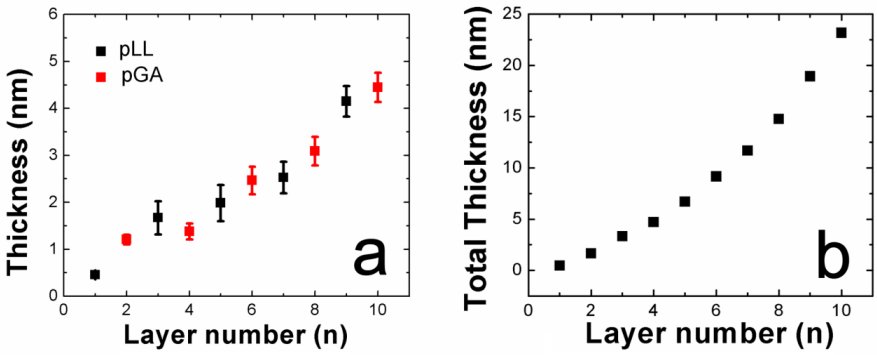

Figure 4.5: Ellipsometric thicknesses of the PEM films obtained using MUA-modified Au-on-glass slides. These thicknesses do not include MUA, which has a height of ~1.7 nm on Au. (a) Individual thicknesses of PEM films terminated in either pLL (black) or pGA (red). (b) Total thicknesses of the films with increasing *n*.

PtNP Collisions at pLL-Modified Au UMEs

Collision experiments were performed for each of the following three types of polymer thin films: pLL, pLL-pGA, and pLL-pGA-pLL. After modification via LbL deposition, each electrode was rinsed with H_2O and used immediately.

CVs were obtained before each experiment, and the average limiting current for N_2H_4 oxidation, determined using 15 independently prepared pLL-modified UMEs, was −0.4 ± 0.2 nA. UMEs yielding a limiting current higher than −0.7 nA were deemed too defective and not used for collision experiments. **Figure 4.6a** presents a typical CV (black trace) of a pLL-modified UME before introduction of PtNPs. After obtaining the CV, a background *i*-*t* curve was collected (**Figure 4.6b**,

black trace). No current transients are observed, and the steady-state current is ~–0.4 nA. After injection of 5.0 pM Pt NPs, however (**Figure 4.6b**, red trace), several large current steps characteristic of Pt NP collisions at naked Au electrodes are apparent.[9] These step-shaped transients (**Figure 4.6b**, inset) are likely due to electrostatic adsorption of the negatively charged Pt NPs (zeta potential (ζ), –59 mV, **Figure 4.2**) to the positively charged pLL film. Recall that such large and easily discernible collision events were not observed for the MUA-only UMEs (**Figure 4.4**), suggesting that collisions are not occurring at defect sites in the pLL film (more about defects later). In addition to the step-shaped current transients, spike-shaped collision signatures are also observed for the pLL films, especially at concentrations of Pt NPs greater than 7.5 pM (**Figure 4.7**). These spike-shaped transients likely arise from rapid deactivation of the Pt NP surface, as has been previously shown by the Stevenson group for Hg electrodes.[43]

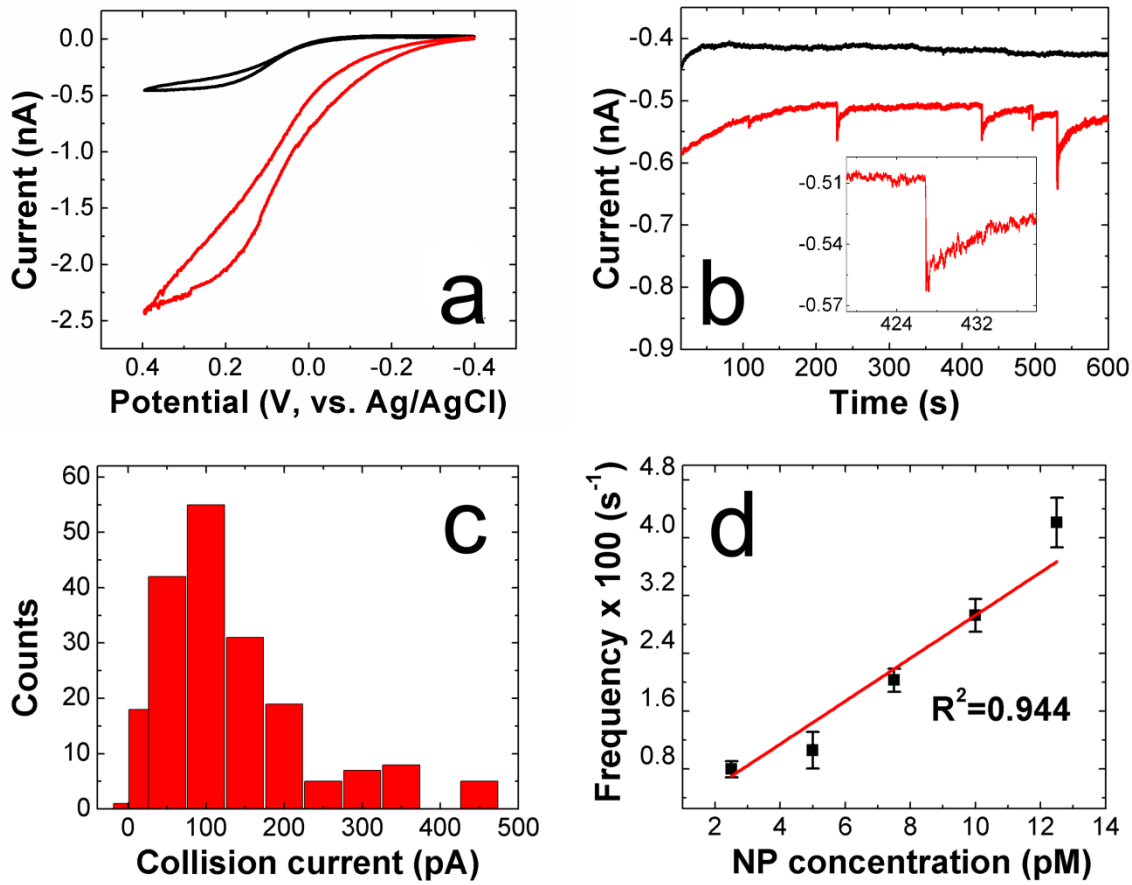

Figure 4.6: Electrochemical results obtained using a pLL-modified Au UME. For all experiments, the solution contained 10.0 mM N_2H_4 and 50 mM PB (pH 7). (a) CVs for a pLL-modified UME before (black) and after (red) a 600 s collision experiment using 5.0 pM PtNPs. (b) *i-t* curves recorded at +400 mV in the absence (black) and presence (red) of 5.0 pM PtNPs. The inset shows an expanded view of a current transient exhibiting a step-like profile. (c) Histogram showing the distribution of current amplitudes for individual collisions. The average collision size is 140 ± 200 pA. (d) Plot of current-transient frequency (steps and peaks) as a function of the concentration of PtNPs. The error bars represent the standard deviation of current signals obtained from three separate experiments at each concentration.

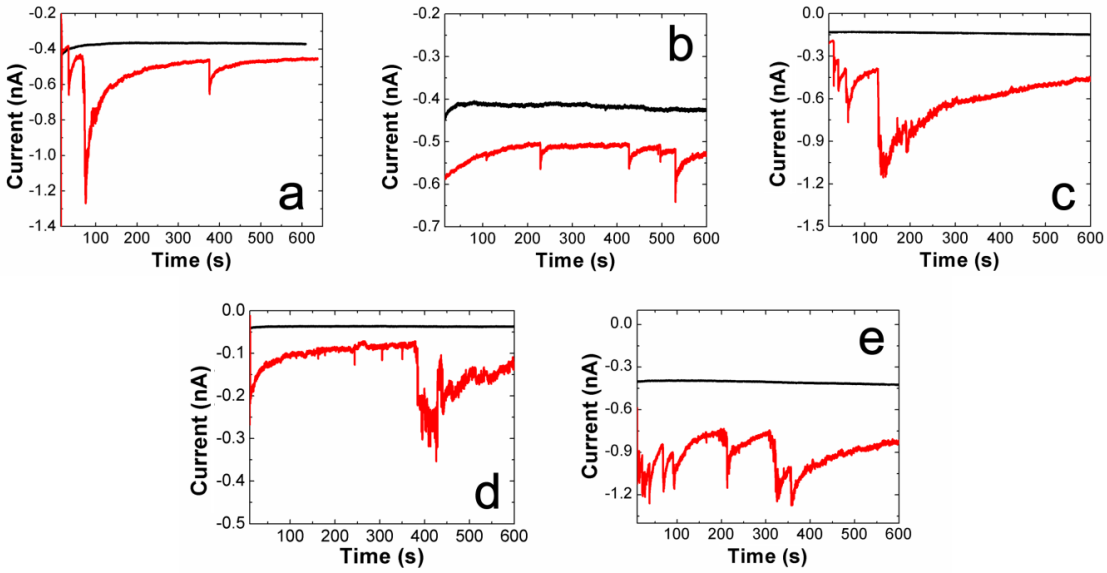

Figure 4.7: *i-t* traces showing current transients resulting from collisions between PtNPs and pLL-modified UMEs. The solution contained 10.0mM N_2H_4 and 50 mM PB (pH 7). Plots show the change in current in the absence (black) and presence (red) of (a) 2.5, (b) 5.0, (c) 7.5, (d) 10.0, and (e) 12.5 pM PtNPs.

A histogram showing the collision current amplitudes for all of the pLL-modified UMEs (at all PtNP concentrations) is shown in **Figure 4.6c**. Collision sizes larger than 500 pA, which accounted for <5% of all events, were excluded from this distribution as these large sizes are likely due to aggregated PtNPs rather than individual particles. The average collision size across all of the pLL experiments performed is 140 ± 200 pA. Although the standard deviation for this average is large, it is comparable to the average collision size experimentally obtained at naked Au UMEs (185 ± 177 pA) for the same batch of Pt NPs. Note, however, that

both of these values are smaller than the collision current of 613 pA calculated using **equation 1.1**, which has previously been shown to provide reasonable agreement with experimental results for collisions using ~4 nm NPs.[9] We do not know why the currents calculated using this equation do not agree with the experimental results. One possibility is that the majority of observed collisions originate from a small subset of PtNPs at the low end of the size distribution, and another possibility is that this empirical equation is simply not appropriate for the relatively large NPs (57 ± 10 nm) used in this study. **Figure 4.6d** presents collision frequencies over the full range of PtNP concentrations examined. As has been found previously using naked Au UMEs, the frequency is linearly related to NP concentration.[21]

After each collision experiment, the UME was removed from solution, rinsed with H_2O, and then reimmersed in a fresh solution containing 10 mM N_2H_4 and 50 mM PB. **Figure 4.6a** (red trace) compares a CV of a pLL-modified UME after a collision experiment using 5.0 pM PtNPs with the CV obtained prior to the collision experiments. The limiting current arising from N_2H_4 oxidation is much larger than it was before the collision experiment (black trace). This observation is consistent with previous reports that adsorption of NPs onto LbL films leads to an enhanced current response compared to that of the passivating LbL film alone.[124,126,127] Accordingly, we conclude

that the data in **Figure 4.6a** confirm that at least some of the colliding Pt NPs remain on the pLL surface and are active for electrocatalytic oxidation of N_2H_4. Further evidence of adsorbed PtNPs on the pLL film comes from the negative shift of the onset potential for N_2H_4 oxidation, from ~0 V to ~−0.25 V. This is a consequence of the electrocatalytic properties of Pt relative to Au. Similar behavior is observed for CVs obtained after pLL-modified Au UMEs are immersed in a 128 pM PtNP solution for 20 min (**Figure 4.8**), which is known to result in electrostatic adsorption of Pt NPs.[124,125]

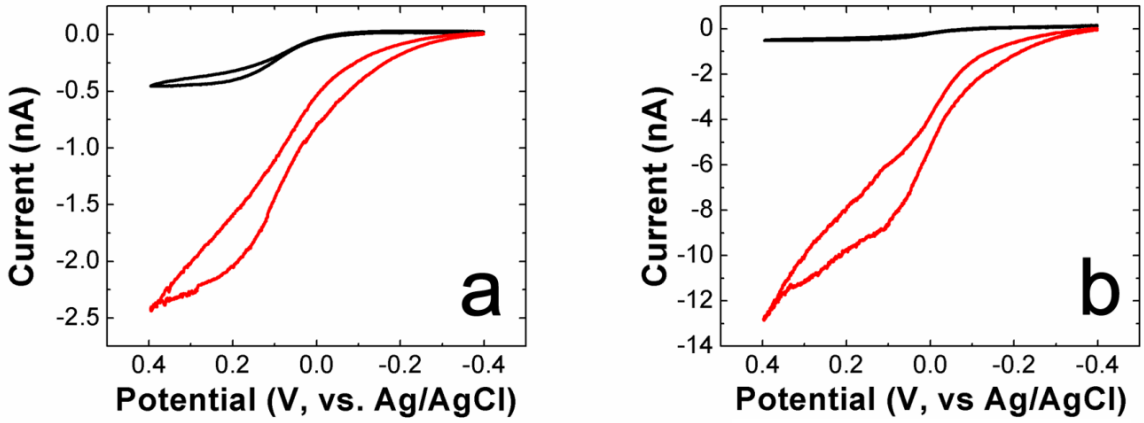

Figure 4.8: CVs obtained using pLL-modified Au UMEs. (a) before (black trace) and after (red trace) introduction of 5.0pM PtNPs in a solution containing 10 mM N_2H_4 and 50 mM PB (pH 7). Immediately after a CV of the pLL-modified UME was taken, PtNPs were introduced into solution, and an *i-t* curve was recorded for 600 s at +400 mV. Subsequently, the UME was rinsed and re-immersed in fresh N_2H_4 solution, and the red trace was obtained. (b) CVs obtained before (black trace) and after (red trace) incubation of the pLL-modified UME in a solution containing 128 pM PtNPs for 20 min. Scan rate = 50 mV/s.

Indeed, **Figure 4.9** is an SEM image showing PtNPs adsorbed onto the surface of a pLL-modified Au UME.

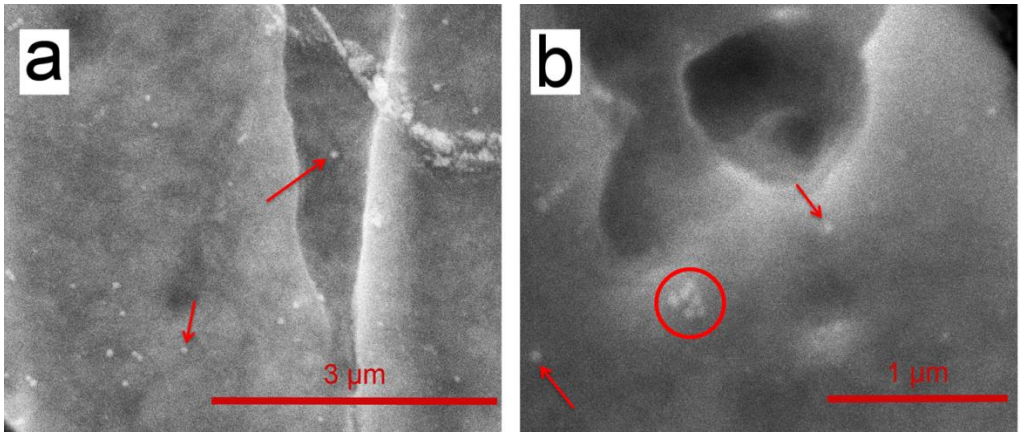

Figure 4.9: (a) SEM image of the pLL-modified Au UME surface after exposure to 12.5 pM PtNPs for 10 min. Arrows designate the adsorption of single PtNPs. (b) Higher magnification SEM image of the same electrode. The circle indicates the presence of NP aggregates on the film.

To reduce the likelihood of collisions occurring at defect sites within the LbL films, we used relatively large Pt NPs (57 ± 10 nm). Nevertheless, the question of whether these collisions are occurring on top of the polyelectrolyte film or within defects is both crucial and difficult to answer directly. We can, however, indirectly address this question in two ways. First, if collisions are occurring at defect sites, then a correlation should exist between the limiting current for N_2H_4 oxidation measured at pLL-modified UMEs (no PtNPs) and the collision current amplitude.[133] That is, larger defects will permit direct collisions by larger PtNPs (recall that because of aggregation, there is a broad distribution of PtNPs in these experiments, **Figure 4.6c**), and this will

in turn result in larger collision currents. **Figure 4.10a** is a histogram showing the average current due to PtNP collisions versus the limiting current measured in the same solution (10 mM N_2H_4 plus 50 mM PB) and the same pLL-coated electrode prior to introduction of the PtNPs. There is clearly no correlation between these parameters. For example, the UME with the highest limiting current (–0.7 nA), which should have the most defective pLL film, yields an average current amplitude value of ~146 pA. However, this value is about half that observed at a more passivated UME (limiting current of –0.1 nA).

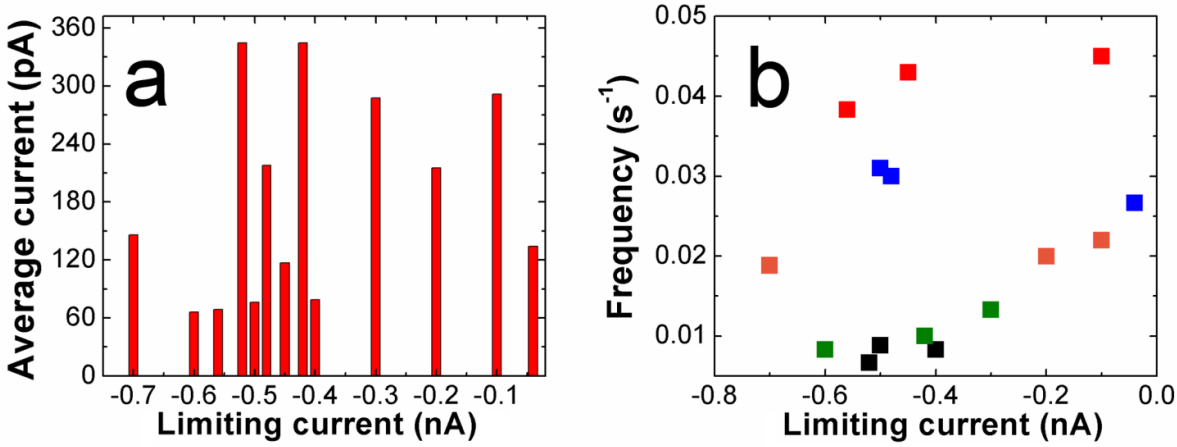

Figure 4.10: (a) Plot of average collision current for each pLL-modified Au UME versus the limiting current for N_2H_4 oxidation. The experiments were carried out in solutions containing 10.0 mM N_2H_4 and 50 mM PB (pH 7). The limiting current was determined from CVs obtained immediately after UME modification but prior to recording *i-t* curves in the presence of PtNPs. (b) Scatterplot of collision frequency versus the limiting current for N_2H_4 oxidation for each pLL-modified Au UME. The limiting current was determined from CVs obtained immediately after UME modification but prior to recording *i-t* curves in the presence of PtNPs. Three individual experiments are shown for each of five PtNP concentrations: 2.5 (black), 5.0 (green), 7.5 (orange), 10.0 (blue), and 12.5 (red) pM.

The second indirect evidence for collisions not occurring at defect sites within the pLL film is the following. A higher density of defect sites would provide more opportunities for direct collisions between Pt NPs and the naked Au surface. In other words, a positive correlation

should exist between the frequency of PtNP collisions and the limiting current because of direct oxidation of N_2H_4 at the Au surface. As shown in **Figure 4.10b**, no such correlation is observed. For example, consider the results obtained using 5.0 pM PtNPs (green data points). In this case, the UME with the highest limiting current (−0.6 nA) yields the lowest collision frequency (0.0083 s^{-1}).

The absence of correlations between the limiting current resulting from N_2H_4 oxidation at the Au UME and the current amplitude and collision frequency suggests that NP collisions are occurring at the solution-pLL interface rather than at naked regions of the Au surface.

PtNP Collisions at MUA-pLL-pGA-Modified Au UMEs

On the basis of the results observed using the negatively charged MUA SAM surface and the positively charged pLL surface, we surmised that addition of a negatively charged pGA polymer layer would suppress the collision amplitude and frequency of negatively charged PtNPs. Results confirming this hypothesis are shown in **Figure 4.11**. For example, **Figure 4.11a** shows *i*-*t* traces in the absence (black) and presence (red) of 2.5 pM PtNPs. In contrast to *i*-*t* traces for the pLL system (**Figure 4.7**), no current transients are observed after addition of pGA, effectively shutting down

electrocatalytic activity. This is likely due to electrostatic repulsion between the outermost pGA film and the negatively charged PtNPs.

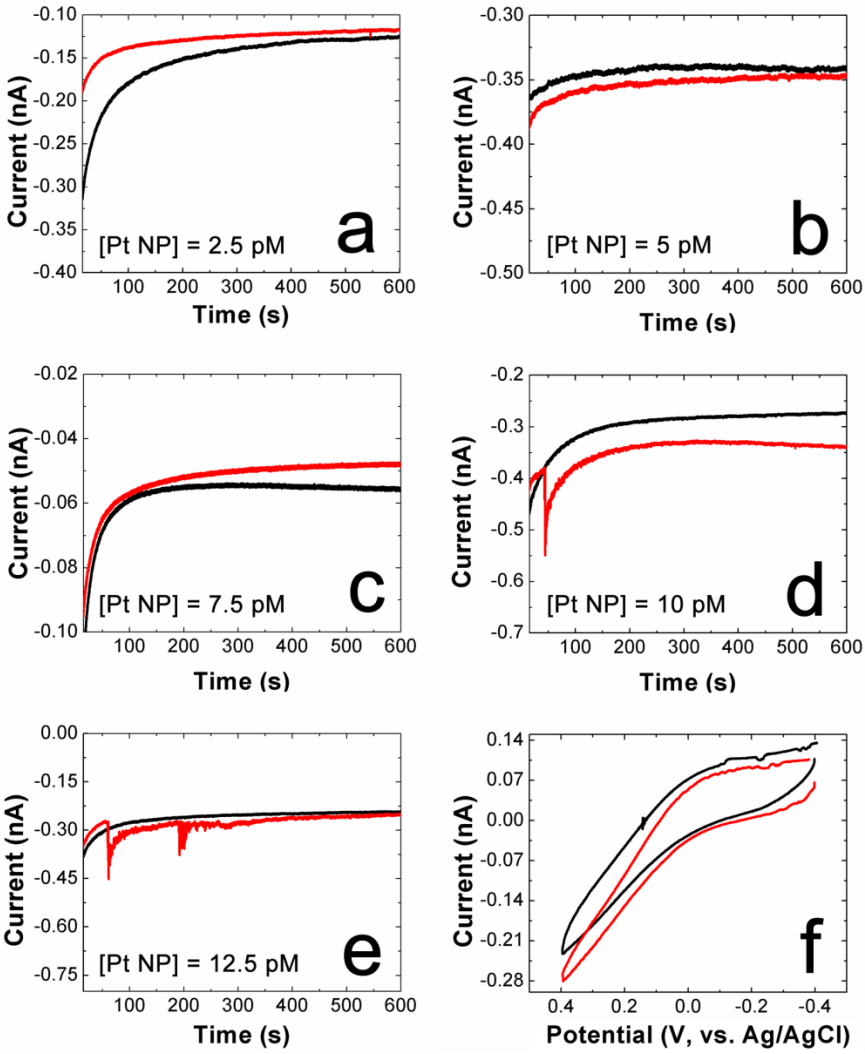

Figure 4.11: Electrochemical results obtained using a Au UME coated with a pLL-pGA PEM film. (a-e) *i-t* plots obtained at +400 mV in the absence (black) and presence (red) of Pt NPs at the indicated concentrations. (f) CVs obtained before (black) and after (red) a 600 s collision experiment using a 5.0 pM Pt NP solution. Scan rate: 50 $mV\,s^{-1}$. Solutions for all experiments contained 10.0 mM N_2H_4 and 50 mM PB (pH 7).

Similar results are obtained for 5.0 and 7.5 pM PtNP concentrations at pLL-pGA electrodes, as shown in **Figure 4.11b,c**. After addition of PtNPs to the solution, no current transients arising from PtNP collisions are observed. When the PtNP concentration is 10 pM, one current transient is observed at ~50 s. This may be due to a nonuniform distribution of the pGA film on top of the pLL layer. Although polyelectrolyte films formed by LbL deposition are generally thought to reverse the surface charge with each subsequent layer, polyelectrolytes are deposited as islands of varying thickness rather than as uniform layers.[146] Small exposed areas of the previous pLL layer may provide enough electrostatic attraction to allow a small number of current transients at this higher concentration. At the highest concentration of PtNPs (12.5 pM), ~4-5 collision events are observed per 600 s, but this number is much lower than that observed at pLL-modified UMEs (~24 transients for the same PtNP concentration and the same duration experiment).

Figure 4.11f shows CVs obtained before (black) and after (red) addition of 5.0 pM Pt NPs. The onset potential for N_2H_4 oxidation does not shift significantly, as was demonstrated for the pLL system (**Figure 4.6a**), and there is no increase in current after addition of PtNPs. This is evidence that an insignificant number of PtNPs collide and adsorb onto the film during the *i-t* experiment. It is likely that the overall

negative charge of pGA electrostatically repels the PtNPs and hinders ECA on the Pt surface. To summarize, the addition of the pGA layer shuts off collisions between PtNPs and the UME.

PtNP Collisions at pLL-pGA-pLL-Modified Au UMEs

To confirm the importance of electrostatics in these types of collision experiments, and also to show that collisions can be detected through relatively thick LbL polymer films, we obtained *i-t* plots for Au UMEs modified with a second layer of positively charged pLL. **Figure 4.12a** shows representative *i-t* curves in the absence (black trace) and presence (red trace) of 5.0 pM PtNPs for a MUA-pLL-pGA-pLL film. No current transients are observed in the absence of PtNPs. In the presence of PtNPs, however, collisions are observed, indicating reactivation of the UME. This reactivation of the electrode by addition of a second positively charged layer atop negatively charged pGA clearly points to the importance of electrostatics in these experiments. It also provides additional confidence that collisions are not occurring at pinholes in the LbL films because surely this thicker 3-layer film would contain fewer defects than the 2-layer, pGA-capped surface. Results similar to those shown in **Figure 4.12a** are provided in **Figure 4.13** for Pt NP concentrations ranging from 2.5-12.5 pM.

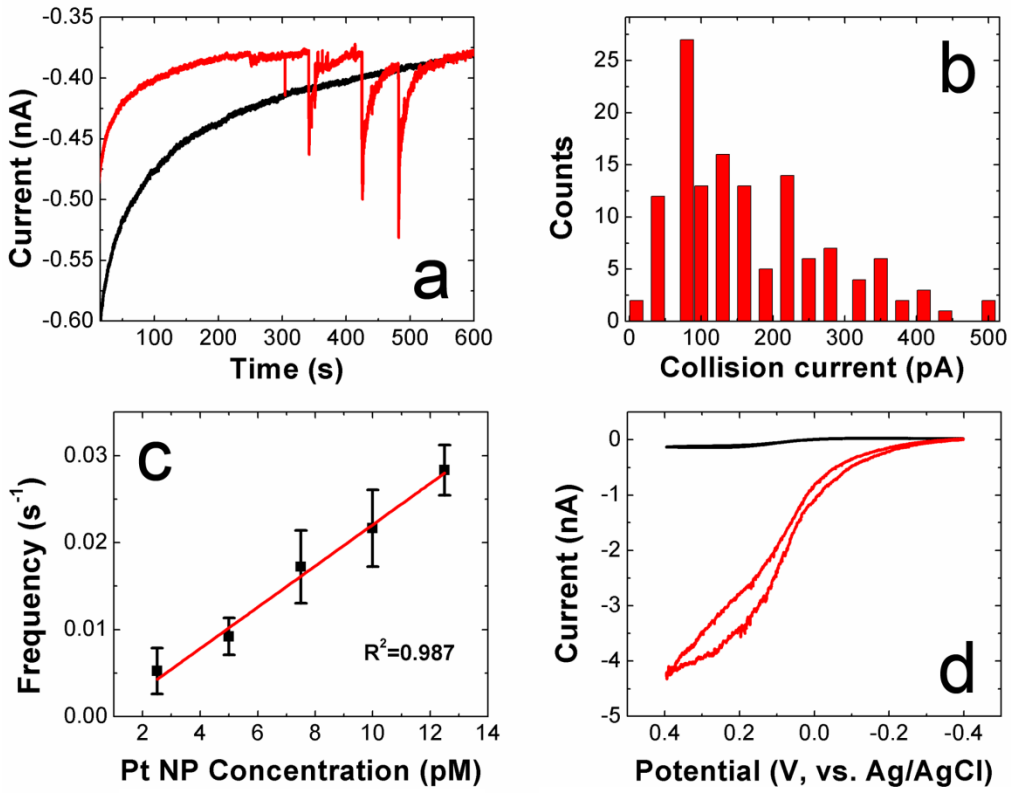

Figure 4.12: Electrochemical results obtained using a pLL-pGA-pLL-modified Au UME. For all experiments, the solution contained 10.0 mM N_2H_4 and 50 mM PB (pH 7). (a) *i-t* curves obtained at +400 mV recorded in the absence (black) and presence (red) of 5.0 pM PtNPs. (b) Histogram showing the distribution of current amplitudes for individual collisions. The average collision amplitude is 157 ± 114 pA. (c) Plot of the frequency of current transients (steps and peaks) as a function of the concentration of PtNPs. The error bars represent the standard deviation of current signals obtained from three separate experiments at each concentration. (d) CVs for a pLL-pGA-pLL-modified UME before (black) and after (red) a 600 s collision experiment using 5.0 pM PtNPs.

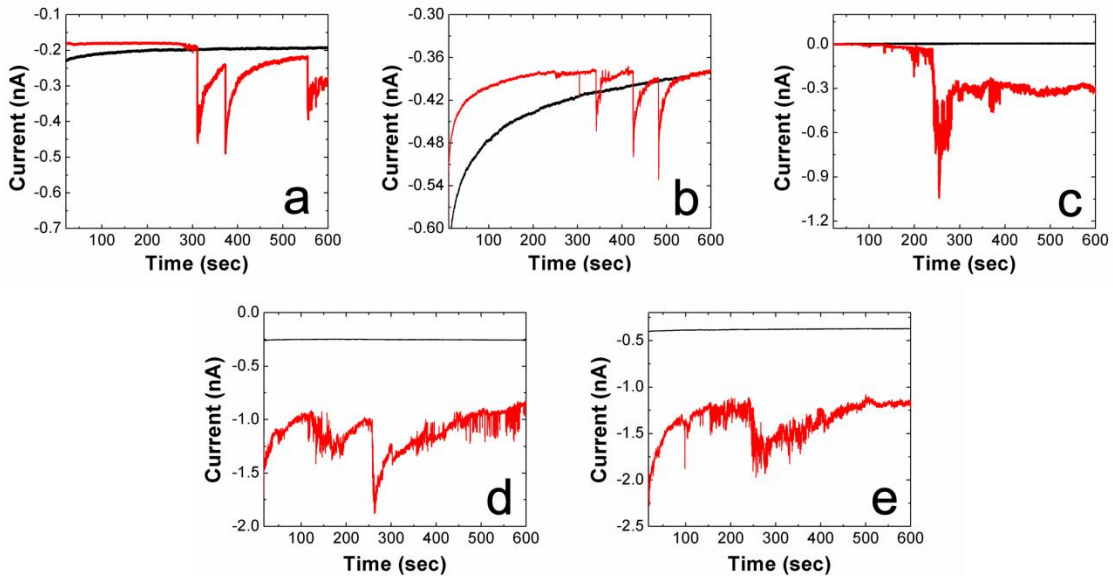

Figure 4.13: *i-t* traces showing current transients resulting from collisions between PtNPs and pLL-pGA-pLL-modified UMEs. The solution contained 10.0 mM N_2H_4 and 50 mM PB (pH 7). Plots show the change in current in the absence (black) and presence (red) of (a) 2.5, (b) 5.0, (c) 7.5, (d) 10.0, and (e) 12.5 pM PtNPs.

A histogram showing the distribution of collision amplitudes obtained using 15 independently prepared UMEs is shown in **Figure 4.12b**. The average collision size for this system is 157 ± 114 pA, which is similar to that obtained for Au UMEs modified with a single pLL layer (140 ± 200 pA). This means that within the context of the relatively large standard deviations, the collision currents are independent of film thickness. This observation is consistent with reactivation trends observed by Gooding and co-workers.[149]

Figure 4.12c shows that the frequency of collisions is a linear function of NP concentration for the three-layer polymer film. An indication that electrons are tunneling from the PtNP to the underlying electrode can be found in the CVs measured before and after collision experiments (**Figure 4.12d**). As for the MUA-pLL film (**Figure 4.6a**), an increase in the limiting current and a negative shift in the onset potential for N_2H_4 oxidation are observed. An analysis of limiting current, average collision size, and frequency of collisions similar to that carried out for the pLL-modified UMEs (**Figure 4.10**) can be found in **Figure 4.14**. As alluded to earlier, the absence of a correlation between these three variables suggests that collisions occur on top of the PEM films rather than at defects penetrating through the film to the underlying UME surface.

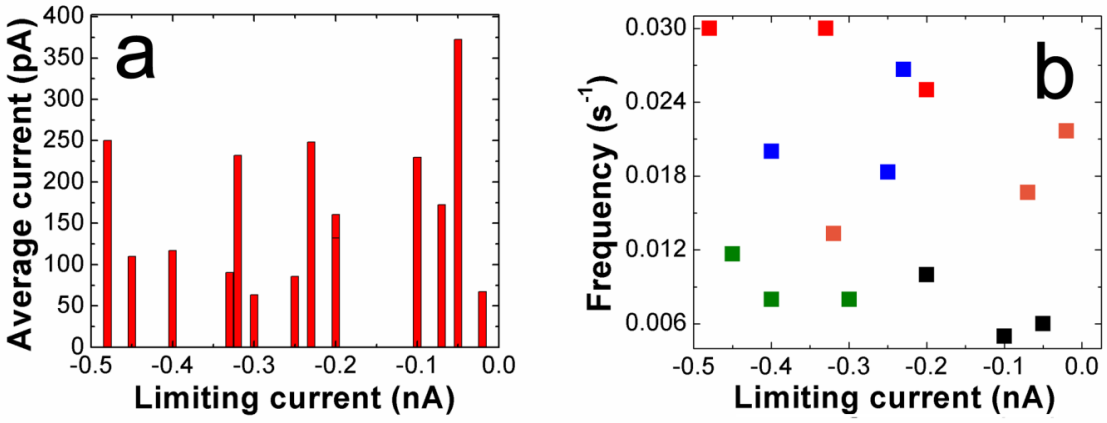

Figure 4.14: (a) Plot of average collision size for each pLL-pGA-pLL-modified UME versus the limiting oxidative current for collision experiments performed in 10.0 mM N_2H_4 + 50 mM PB (pH 7). The limiting current was determined from CVs obtained immediately after UME modification and prior to recording *i-t* curves. There is no correlation between collision size and limiting current. (b) Scatterplot of frequency of collision events as a function of the limiting oxidative current of each pLL-pGA-pLL-modified electrode. The limiting current was determined from CVs obtained immediately after UME modification and prior to recording *i-t* curves. Three experiments at five concentrations of PtNPs are shown: 2.5 (black), 5.0 (green), 7.5 (orange), 10.0 (blue), and 12.5 (red) pM. There is no correlation between frequency and limiting current.

Summary and Conclusions

We have shown that collisions between PtNPs and PEM films result in easily measurable currents. There are two interesting conclusions that can be drawn from this study. First, despite the thickness of the insulating PEM films (the

3-layer film, including the SAM layer, has an ellipsometric thickness of ~5 nm) electrons are able to tunnel from the PtNPs to the electrode resulting in electrocatalytic N_2H_4 oxidation at the PEM film–solution interface. These single-particle measurements are in accord with prior reports showing that the electrochemical activity of passive LbL films can be reactivated by adsorption of metallic NPs.[124,150-158] Second, it is possible to control the collisions by manipulating the net electrostatic charge present on the outer surface of the PEM thin film. These results, which demonstrate that chemistry can be used to control ECA, set the stage for future sensing applications.

Chapter 5: Conclusions and Outlook

The results presented in this dissertation demonstrate the applicability of ECA collisions for biosensing applications, specifically oligonucleotides such as microRNA. One of the common goals of the chapters presented here has been to develop biosensing platforms for the ECA technique. ECA offers an attractive method of detection for nanoparticles, and now, biological targets, due to its ability to detect biological events in a discrete, real-time fashion. It offers ultra-low levels of detection, such as attomolar or lower, and high sensitivity. The ECA methods presented in this dissertation are robust and fairly simple to implement. They utilize the versatility that metallic NPs offer in terms of sensor labels, either by reactivating DNA-passivated PtNPs via enzymatic cleavage (Chapters 2 and 3) or turning the electrochemical signal via electrostatics.

The N_2H_4/PtNP system has been extensively studied, but this work was unique due to the introduction of enzymatic digestion as a means of oligonucleotide detection. Although N_2H_4 solutions have been demonstrated to be problematic for PtNP colloid aggregation, we showed that modification with a DNA shell increases colloidal stability in these solutions. Furthermore, this approach has the potential to be generally applied to other systems, such as the detection of peptides

or proteins. This work also demonstrated that it is possible to observe N_2H_4 collisions through tunneling electron-transfer of up to ~5 nm from the electrode surface, and that collisions can be controlled by manipulating the net electrostatic charge present on the outer surface of polyelectrolyte films.

Although the N_2H_4/PtNP system has proven to be robust and reproducible for sensing applications, there are still problems and fundamental questions that must be addressed. In particular, integration of magnetic pre-concentration into a viable biosensor is of great interest. Nanoelectrodes, which generate significantly lower background current when compared to microelectrodes, have also been the subject of recent investigations. These nanoelectrodes bring the possibility of detecting even smaller NPs, as well as offering a platform for electrocatalytic studies for a single NP adsorbed on the surface. The use of fast scan cyclic voltammetry to glean information about individual NPs colliding in real-time has also been explored, with promising results of their electrocatalytic nature.

References

(1) Moerner, W. E.; Kador, L. Optical Detection and Spectroscopy of Single Molecules in a Solid. *Phys. Rev. Lett.* **1989**, *62*, 2535-2538.

(2) Orrit, M.; Bernard, J. Single Pentacene Molecules Detected by Fluorescence Excitation in a *P* -Terphenyl Crystal. *Phys. Rev. Lett.* **1990**, *65*, 2716-2719.

(3) Bard, A. J.; Zhou, H.; Kwon, S. J. Electrochemistry of Single Nanoparticles via Electrocatalytic Amplification. *Isr. J. Chem.* **2010**, *50*, 267-276.

(4) Hellberg, D.; Scholz, F.; Schauer, F.; Weitschies, W. Bursting and Spreading of Liposomes on the Surface of a Static Mercury Drop Electrode. *Electrochem. commun.* **2002**, *4*, 305-309.

(5) Scholz, F.; Hellberg, D.; Schubert, F.; Lovrić, M.; Omanović, D.; Hernández, V. A.; Thede, R. Kinetics of Liposome Adhesion on a Mercury Electrode. *J. Phys. Chem. B* **2005**, *109*, 14715-14726.

(6) Scholz, F.; Hellberg, D.; Harnisch, F.; Hummel, A.; Hasse, U. Detection of the Adhesion Events of Dispersed Single Montmorillonite Particles at a Static Mercury Drop Electrode. *Electrochem. commun.* **2004**, *6*, 929-933.

(7) Quinn, B. M.; Van 't Hof, P. G.; Lemay, S. G. Time-Resolved Electrochemical Detection of Discrete Adsorption Events. *J. Am. Chem. Soc.* **2004**, *126*, 8360-8361.

(8) Xiao, X.; Bard, A. J. Observing Single Nanoparticle Collisions at an Ultramicroelectrode by Electrocatalytic Amplification. *J. Am. Chem. Soc.* **2007**, *129*, 9610-9612.

(9) Xiao, X.; Fan, F.-R. F.; Zhou, J.; Bard, A. J. Current Transients in Single Nanoparticle Collision Events. *J. Am. Chem. Soc.* **2008**, *130*, 16669-16677.

(10) Kwon, S. J.; Zhou, H.; Fan, F.-R. F.; Vorobyev, V.; Zhang, B.; Bard, A. J. Stochastic Electrochemistry with Electrocatalytic Nanoparticles at Inert Ultramicroelectrodes--Theory and Experiments. *Phys. Chem. Chem. Phys.* **2011**, *13* (12), 5394-5402.

(11) Park, J. H.; Thorgaard, S. N.; Zhang, B.; Bard, A. J. Single Particle Detection by Area Amplification: Single

Wall Carbon Nanotube Attachment to a Nanoelectrode. *J. Am. Chem. Soc.* **2013**, *135*, 5258-5261.
(12) Park, J. H.; Boika, A.; Park, H. S.; Lee, H. C.; Bard, A. J. Single Collision Events of Conductive Nanoparticles Driven by Migration. *J. Phys. Chem. C* **2013**, *117*, 6651-6657.
(13) Zhou, H.; Fan, F.-R. F.; Bard, A. J. Observation of Discrete Au Nanoparticle Collisions by Electrocatalytic Amplification Using Pt Ultramicroelectrode Surface Modification. *J. Phys. Chem. Lett.* **2010**, *1*, 2671-2674.
(14) Xiao, X.; Pan, S.; Jang, J. S.; Fan, F.-R. F.; Bard, A. J. Single Nanoparticle Electrocatalysis: Effect of Monolayers on Particle and Electrode on Electron Transfer. *J. Phys. Chem. C* **2009**, *113*, 14978-14982.
(15) Fan, F.-R. F.; Bard, A. J. Observing Single Nanoparticle Collisions by Electrogenerated Chemiluminescence Amplification. *Nano Lett.* **2008**, *8*, 1746-1749.
(16) Kwon, S. J.; Bard, A. J. DNA Analysis by Application of Pt Nanoparticle Electrochemical Amplification with Single Label Response. *J. Am. Chem. Soc.* **2012**, *134*, 10777-10779.
(17) Wakerley, D.; Güell, A. G.; Hutton, L. A.; Miller, T. S.; Bard, A. J.; Macpherson, J. V. Boron Doped Diamond Ultramicroelectrodes: A Generic Platform for Sensing Single Nanoparticle Electrocatalytic Collisions. *Chem. Commun.* **2013**, *49*, 5657-5659.
(18) Ahn, H. S.; Bard, A. J. Single-Nanoparticle Collision Events: Tunneling Electron Transfer on a Titanium Dioxide Passivated N-Silicon Electrode. *Angew. Chem. Int. Ed.* **2015**, *54*, 13753-13757.
(19) Dick, J. E.; Bard, A. J. Recognizing Single Collisions of $PtCl_6^{2-}$ at Femtomolar Concentrations on Ultramicroelectrodes by Nucleating Electrocatalytic Clusters. *J. Am. Chem. Soc.* **2015**, *137*, 13752-13755.
(20) Zhou, H.; Park, J. H.; Fan, F.-R. F.; Bard, A. J. Observation of Single Metal Nanoparticle Collisions by Open Circuit (Mixed) Potential Changes at an Ultramicroelectrode. *J. Am. Chem. Soc.* **2012**, *134*, 13212-13215.
(21) Kwon, S. J.; Fan, F.-R. F.; Bard, A. J. Observing

Iridium Oxide (IrO(x)) Single Nanoparticle Collisions at Ultramicroelectrodes. *J. Am. Chem. Soc.* **2010**, *132*, 13165-13167.
(22) Bentley, C. L.; Kang, M.; Unwin, P. R. Time-Resolved Detection of Surface Oxide Formation at Individual Gold Nanoparticles: Role in Electrocatalysis and New Approach for Sizing by Electrochemical Impacts. *J. Am. Chem. Soc.* **2016**, *138*, 12755-12758.
(23) Rees, N. V; Zhou, Y.-G.; Compton, R. G. The Aggregation of Silver Nanoparticles in Aqueous Solution Investigated via Anodic Particle Coulometry. *Chemphyschem* **2011**, *12*, 1645-1647.
(24) Cutress, I. J.; Rees, N. V.; Zhou, Y.-G.; Compton, R. G. Nanoparticle-electrode Collision Processes: Investigating the Contact Time Required for the Diffusion-Controlled Monolayer Underpotential Deposition on Impacting Nanoparticles. *Chem. Phys. Lett.* **2011**, *514*, 58-61.
(25) Rees, N. V.; Zhou, Y.-G.; Compton, R. G. Making Contact: Charge Transfer during Particle-electrode Collisions. *RSC Adv.* **2012**, *2*, 379-384.
(26) Zhou, Y.-G.; Rees, N. V; Compton, R. G. Nanoparticle-Electrode Collision Processes: The Underpotential Deposition of Thallium on Silver Nanoparticles in Aqueous Solution. *Chemphyschem* **2011**, *12*, 2085-2087.
(27) Aldous, L.; Compton, R. G. The Mechanism of Hydrazine Electro-Oxidation Revealed by Platinum Microelectrodes: Role of Residual Oxides. *Phys. Chem. Chem. Phys.* **2011**, *13*, 5279-5287.
(28) Zhou, Y.-G.; Rees, N. V; Compton, R. G. The Electrochemical Detection of Tagged Nanoparticles via Particle-Electrode Collisions: Nanoelectroanalysis beyond Immobilisation. *Chem. Commun.* **2012**, *48*, 2510-2512.
(29) Sokolov, S. V.; Eloul, S.; Kätelhön, E.; Batchelor-McAuley, C.; Compton, R. G.; Compton, R. G.; Tessier, G.; Kanoufi, F.; Rumble, J. Electrode-particle Impacts: A Users Guide. *Phys. Chem. Chem. Phys.* **2017**, *19*, 28-43.
(30) Zhou, Y.-G.; Rees, N. V.; Compton, R. G. Nanoparticle-electrode Collision Processes: The Electroplating of Bulk Cadmium on Impacting Silver Nanoparticles. *Chem.*

Phys. Lett. **2011**, *511*, 183-186.
(31) Holt, L. R.; Plowman, B. J.; Young, N. P.; Tschulik, K.; Compton, R. G. The Electrochemical Characterization of Single Core-Shell Nanoparticles. *Angew. Chem. Int. Ed. Engl.* **2016**, *55*, 397-400.
(32) Zhou, Y.-G.; Rees, N. V; Compton, R. G. The Electrochemical Detection and Characterization of Silver Nanoparticles in Aqueous Solution. *Angew. Chem. Int. Ed. Engl.* **2011**, *50*, 4219-4221.
(33) Jiao, X.; Sokolov, S. V.; Tanner, E. E. L.; Young, N. P.; Compton, R. G.; Silien, C.; Mani, A. A.; Thiry, P. A.; Peremans, A.; Shao-Horn, Y. Exploring Nanoparticle Porosity Using Nano-Impacts: Platinum Nanoparticle Aggregates. *Phys. Chem. Chem. Phys.* **2017**, *19*, 64-68.
(34) Krause, K. J.; Yakushenko, A.; Wolfrum, B. Stochastic On-Chip Detection of Subpicomolar Concentrations of Silver Nanoparticles. *Anal. Chem.* **2015**, *87*, 7321-7325.
(35) Tanner, E. E. L.; Batchelor-McAuley, C.; Compton, R. G. Single Nanoparticle Detection in Ionic Liquids. *J. Phys. Chem. C* **2016**, *120*, 1959-1965.
(36) Oja, S. M.; Robinson, D. A.; Vitti, N. J.; Edwards, M. A.; Liu, Y.; White, H. S.; Zhang, B. Observation of Multipeak Collision Behavior during the Electro-Oxidation of Single Ag Nanoparticles. *J. Am. Chem. Soc.* **2017**, *139*, 708-718.
(37) Boika, A.; Thorgaard, S. N.; Bard, A. J. Monitoring the Electrophoretic Migration and Adsorption of Single Insulating Nanoparticles at Ultramicroelectrodes. *J. Phys. Chem. B* **2013**, *117*, 4371-4380.
(38) Fosdick, S. E.; Anderson, M. J.; Nettleton, E. G.; Crooks, R. M. Correlated Electrochemical and Optical Tracking of Discrete Collision Events. *J. Am. Chem. Soc.* **2013**, *135*, 5994-5997.
(39) Yoo, J. J.; Anderson, M. J.; Alligrant, T. M.; Crooks, R. M. Electrochemical Detection of Insulating Beads at Subattomolar Concentration via Magnetic Enrichment in a Microfluidic Device. *Anal. Chem.* **2014**, *86*, 4302-4307.
(40) Yoo, J. J.; Kim, J.; Crooks, R. M. Direct Electrochemical Detection of Individual Collisions between Magnetic Microbead/silver Nanoparticle Conjugates and a Magnetized Ultramicroelectrode. *Chem.*

Sci. **2015**, *6*, 6665-6671.
(41) Robinson, D. A.; Yoo, J. J.; Castañeda, A. D.; Gu, B.; Dasari, R.; Crooks, R. M.; Stevenson, K. J. Increasing the Collision Rate of Particle Impact Electroanalysis with Magnetically Guided Pt-Decorated Iron Oxide Nanoparticles. *ACS Nano* **2015**, *9*, 7583-7595.
(42) Castaneda, A. D.; Robinson, D. A.; Stevenson, K. J.; Crooks, R. M. Electrocatalytic Amplification of DNA-Modified Nanoparticle Collisions via Enzymatic Digestion. *Chem. Sci.* **2016**, *7*, 6450-6457.
(43) Dasari, R.; Robinson, D. A.; Stevenson, K. J. Ultrasensitive Electroanalytical Tool for Detecting, Sizing, and Evaluating the Catalytic Activity of Platinum Nanoparticles. *J. Am. Chem. Soc.* **2013**, *135*, 570-573.
(44) Dasari, R.; Walther, B.; Robinson, D. A.; Stevenson, K. J. Influence of the Redox Indicator Reaction on Single-Nanoparticle Collisions at Mercury- and Bismuth-Modified Pt Ultramicroelectrodes. *Langmuir* **2013**, *29*, 15100-15106.
(45) Dasari, R.; Tai, K.; Robinson, D. A.; Stevenson, K. J. Electrochemical Monitoring of Single Nanoparticle Collisions at Mercury-Modified Platinum Ultramicroelectrodes. *ACS Nano* **2014**, *8*, 4539-4546.
(46) Jung, A. R.; Lee, S.; Joo, J. W.; Shin, C.; Bae, H.; Moon, S. G.; Kwon, S. J. Potential-Controlled Current Responses from Staircase to Blip in Single Pt Nanoparticle Collisions on a Ni Ultramicroelectrode. *J. Am. Chem. Soc.* **2015**, *137*, 1762-1765.
(47) Hao, R.; Zhang, B. Nanopipette-Based Electroplated Nanoelectrodes. *Anal. Chem.* **2016**, *88*, 614-620.
(48) Zhou, M.; Yu, Y.; Hu, K.; Xin, H. L.; Mirkin, M. V. Collisions of Ir Oxide Nanoparticles with Carbon Nanopipettes: Experiments with One Nanoparticle. *Anal. Chem.* **2017**, *89*, 2880-2885.
(49) Chen, C.-H.; Ravenhill, E. R.; Momotenko, D.; Kim, Y.-R.; Lai, S. C. S.; Unwin, P. R. Impact of Surface Chemistry on Nanoparticle-Electrode Interactions in the Electrochemical Detection of Nanoparticle Collisions. *Langmuir* **2015**, *31*, 11932-11942.
(50) Jiao, X.; Lin, C.; Young, N. P.; Batchelor-McAuley,

C.; Compton, R. G. Hydrogen Oxidation Reaction on Platinum Nanoparticles: Understanding the Kinetics of Electrocatalytic Reactions via ‘‘Nano-Impacts.’’ *J. Phys. Chem. C* **2016**, *120*, 13148-13158.
(51) Zampardi, G.; Batchelor-McAuley, C.; Kätelhön, E.; Compton, R. G. Lithium-Ion-Transfer Kinetics of Single $LiMn_2O_4$ Particles. *Angew. Chem. Int. Ed.* **2017**, *129*, 656-659.
(52) Percival, S. J.; Zhang, B. Fast-Scan Cyclic Voltammetry Allows Determination of Electron-Transfer Kinetic Constants in Single Nanoparticle Collision. *J. Phys. Chem. C* **2016**, *120*, 20536-20546.
(53) Guo, Z.; Percival, S. J.; Zhang, B. Chemically Resolved Transient Collision Events of Single Electrocatalytic Nanoparticles. *J. Am. Chem. Soc.* **2014**, *136*, 8879-8882.
(54) Toh, H. S.; Compton, R. G. Electrochemical Detection of Single Micelles through ‘‘nano-Impacts.’’ *Chem. Sci.* **2015**, *6*, 5053-5058.
(55) Cheng, W.; Compton, R. G. Measuring the Content of a Single Liposome through Electrocatalytic Nanoimpact ‘‘Titrations.’’ *ChemElectroChem* **2016**, *3*, 2017-2020.
(56) Cheng, W.; Compton, R. G. Investigation of Single-Drug-Encapsulating Liposomes Using the Nano-Impact Method. *Angew. Chem. Int. Ed.* **2014**, *53*, 13928-13930.
(57) Kim, B.-K.; Boika, A.; Kim, J.; Dick, J. E.; Bard, A. J. Characterizing Emulsions by Observation of Single Droplet Collisions——Attoliter Electrochemical Reactors. *J. Am. Chem. Soc.* **2014**, *136*, 4849-4852.
(58) Kim, B.-K.; Kim, J.; Bard, A. J. Electrochemistry of a Single Attoliter Emulsion Droplet in Collisions. *J. Am. Chem. Soc.* **2015**, *137*, 2343-2349.
(59) Li, Y.; Deng, H.; Dick, J. E.; Bard, A. J. Analyzing Benzene and Cyclohexane Emulsion Droplet Collisions on Ultramicroelectrodes. *Anal. Chem.* **2015**, *87*, 11013-11021.
(60) Park, S.; Kim, H.; Chae, J.; Chang, J. Electrochemical Generation of Single Emulsion Droplets and In Situ Observation of Collisions on an Ultramicroelectrode. *J. Phys. Chem. C* **2016**, *120*, 3922-3928.
(61) Zhou, X.-F.; Cheng, W.; Batchelor-McAuley, C.;

Tschulik, K.; Compton, R. G. Electrochemical Detection and Characterisation of Polymer Nanoparticles. *Electroanalysis* **2014**, *26*, 248-253.
(62) Stuart, E. J. E.; Tschulik, K.; Batchelor-McAuley, C.; Compton, R. G. Electrochemical Observation of Single Collision Events: Fullerene Nanoparticles. *ACS Nano* **2014**, *8*, 7648-7654.
(63) Sepunaru, L.; Tschulik, K.; Batchelor-McAuley, C.; Gavish, R.; Compton, R. G. Electrochemical Detection of Single E. Coli Bacteria Labeled with Silver Nanoparticles. *Biomater. Sci.* **2015**, *3*, 816-820.
(64) Sepunaru, L.; Plowman, B. J.; Sokolov, S. V.; Young, N. P.; Compton, R. G. Rapid Electrochemical Detection of Single Influenza Viruses Tagged with Silver Nanoparticles. *Chem. Sci.* **2016**, *7*, 3892-3899.
(65) Sepunaru, L.; Sokolov, S. V.; Holter, J.; Young, N. P.; Compton, R. G. Electrochemical Red Blood Cell Counting: One at a Time. *Angew. Chem. Int. Ed.* **2016**, *128*, 9920-9923.
(66) Dick, J. E.; Renault, C.; Bard, A. J. Observation of Single-Protein and DNA Macromolecule Collisions on Ultramicroelectrodes. *J. Am. Chem. Soc.* **2015**, *137*, 8376-8379.
(67) Dick, J. E.; Hilterbrand, A. T.; Boika, A.; Upton, J. W.; Bard, A. J. Electrochemical Detection of a Single Cytomegalovirus at an Ultramicroelectrode and Its Antibody Anchoring. *Proc. Natl. Acad. Sci.* **2015**, *112*, 5303-5308.
(68) Dick, J. E.; Hilterbrand, A. T.; Strawsine, L. M.; Upton, J. W.; Bard, A. J. Enzymatically Enhanced Collisions on Ultramicroelectrodes for Specific and Rapid Detection of Individual Viruses. *Proc. Natl. Acad. Sci.* **2016**, *113*, 6403-6408.
(69) Alligrant, T. M.; Nettleton, E. G.; Crooks, R. M. Electrochemical Detection of Individual DNA Hybridization Events. *Lab Chip* **2013**, *13*, 349-354.
(70) Alligrant, T. M.; Dasari, R.; Stevenson, K. J.; Crooks, R. M. Electrocatalytic Amplification of Single Nanoparticle Collisions Using DNA-Modified Surfaces. *Langmuir* **2015**, *31*, 11724-11733.
(71) Fasoli, J. B.; Corn, R. M. Surface Enzyme Chemistries

for Ultrasensitive Microarray Biosensing with SPR Imaging. *Langmuir* **2015**, *31*, 9527-9536.
(72) Lee, H. J.; Wark, A. W.; Goodrich, T. T.; Fang, S.; Corn, R. M. Surface Enzyme Kinetics for Biopolymer Microarrays: A Combination of Langmuir and Michaelis-Menten Concepts. *Langmuir* **2005**, *21*, 4050-4057.
(73) Yang, W. Nucleases: Diversity of Structure, Function and Mechanism. *Q. Rev. Biophys.* **2011**, *44*, 1-93.
(74) Mishra, N. C. *Nucleases*; John Wiley & Sons, Inc.: Hoboken, NJ, **2002**.
(75) Kao, H.-I.; Bambara, R. A. The Protein Components and Mechanism of Eukaryotic Okazaki Fragment Maturation. *Crit. Rev. Biochem. Mol. Biol.* **2003**, *38*, 433-452.
(76) Shen, B.; Singh, P.; Liu, R.; Qiu, J.; Zheng, L.; Finger, L. D.; Alas, S. Multiple but Dissectible Functions of FEN-1 Nucleases in Nucleic Acid Processing, Genome Stability and Diseases. *Bioessays* **2005**, *27*, 717-729.
(77) Reha-Krantz, L. J. DNA Polymerase Proofreading: Multiple Roles Maintain Genome Stability. *Biochim. Biophys. Acta* **2010**, *1804*, 1049-1063.
(78) Xu, X.; Han, M. S.; Mirkin, C. A. A Gold-Nanoparticle-Based Real-Time Colorimetric Screening Method for Endonuclease Activity and Inhibition. *Angew. Chem. Int. Ed.* **2007**, *46*, 3468-3470.
(79) Liu, M.; Yuan, M.; Lou, X.; Mao, H.; Zheng, D.; Zou, R.; Zou, N.; Tang, X.; Zhao, J. Label-Free Optical Detection of Single-Base Mismatches by the Combination of Nuclease and Gold Nanoparticles. *Biosens. Bioelectron.* **2011**, *26*, 4294-4300.
(80) Prigodich, A. E.; Alhasan, A. H.; Mirkin, C. A. Selective Enhancement of Nucleases by Polyvalent DNA-Functionalized Gold Nanoparticles. *J. Am. Chem. Soc.* **2011**, *133*, 2120-2123.
(81) Li, X.-M.; Wang, L.-L.; Luo, J.; Wei, Q.-L. A Dual-Amplified Electrochemical Detection of mRNA Based on Duplex-Specific Nuclease and Bio-Bar-Code Conjugates. *Biosens. Bioelectron.* **2014**, *65C*, 245-250.
(82) Lehman, I. R.; Nussbaum, A. L. The Deoxyribonucleases of Escherichia Coli : V. ON THE SPECIFICITY OF EXONUCLEASE I (PHOSPHODIESTERASE) . *J. Biol. Chem.*

1964, *239*, 2628-2636.
(83) Bigall, N. C.; Härtling, T.; Klose, M.; Simon, P.; Eng, L. M.; Eychmüller, A. Monodisperse Platinum Nanospheres with Adjustable Diameters from 10 to 100 Nm: Synthesis and Distinct Optical Properties. *Nano Lett.* **2008**, *8*, 4588-4592.
(84) Zhang, X.; Servos, M. R.; Liu, J. Instantaneous and Quantitative Functionalization of Gold Nanoparticles with Thiolated DNA Using a pH-Assisted and Surfactant-Free Route. *J. Am. Chem. Soc.* **2012**, *134*, 7266-7269.
(85) Zhang, X.; Servos, M. R.; Liu, J. Fast pH-Assisted Functionalization of Silver Nanoparticles with Monothiolated DNA. *Chem. Commun.* **2012**, *48*, 10114-10116.
(86) Wehmeyer, K. R.; Wightman, R. M. Cyclic Voltammetry and Anodic Stripping Voltammetry with Mercury Ultramicroelectrodes. *Anal. Chem.* **1985**, *57*, 1989-1993.
(87) Li, H.; Rothberg, L. J. DNA Sequence Detection Using Selective Fluorescence Quenching of Tagged Oligonucleotide Probes by Gold Nanoparticles. *Anal. Chem.* **2004**, *76*, 5414-5417.
(88) Kleijn, S. E. F.; Serrano-Bou, B.; Yanson, A. I.; Koper, M. T. M. Influence of Hydrazine-Induced Aggregation on the Electrochemical Detection of Platinum Nanoparticles. *Langmuir* **2013**, *29*, 2054-2064.
(89) Robinson, D. A.; Kondajji, A. M.; Castañeda, A. D.; Dasari, R.; Crooks, R. M.; Stevenson, K. J. Addressing Colloidal Stability for Unambiguous Electroanalysis of Single Nanoparticle Impacts. *J. Phys. Chem. Lett.* **2016**, *7*, 2512-2517.
(90) Verwey, E. J. W.; Overbeek, J. T. G.; Overbeek, J. T. G. *Theory of the Stability of Lyophobic Colloids*; Dover Books in Science and Mathematics; Dover Publications, **1999**.
(91) Russel, W. B.; Saville, D. A.; Schowalter, W. R. *Colloidal Dispersions*; Cambridge University Press, **1992**.
(92) Castañeda, A. D.; Alligrant, T. M.; Loussaert, J. A.; Crooks, R. M. Electrocatalytic Amplification of Nanoparticle Collisions at Electrodes Modified with Polyelectrolyte Multilayer Films. *Langmuir* **2015**, *31*, 876-885.
(93) Aldous, L.; Compton, R. G. The Mechanism of Hydrazine

Electro-Oxidation Revealed by Platinum Microelectrodes: Role of Residual Oxides. *Phys. Chem. Chem. Phys.* **2011**, *13*, 5279-5287.
(94) ThermoFisher Scientific, modifying enzyme buffers. https://www.thermofisher.com/us/en/home/brands/thermo-scientific/molecular-biology/thermo-scientific-restriction-modifying-enzymes/modifying-enzymes-thermo-scientific/modifying-enzyme-buffers.html, accessed Feb 21, 2016..
(95) Alligrant, T. M.; Anderson, M. J.; Dasari, R.; Stevenson, K. J.; Crooks, R. M. Single Nanoparticle Collisions at Microfluidic Microband Electrodes: The Effect of Electrode Material and Mass Transfer. *Langmuir* **2014**, *30*, 13462-13469.
(96) Lee, H. J.; Wark, A. W.; Corn, R. M. Creating Advanced Multifunctional Biosensors with Surface Enzymatic Transformations. *Langmuir* **2006**, *22*, 5241-5250.
(97) Almeida, M. I.; Reis, R. M.; Calin, G. A. MicroRNA History: Discovery, Recent Applications, and next Frontiers. *Mutat. Res. Mol. Mech. Mutagen.* **2011**, *717*, 1-8.
(98) Farazi, T. A.; Spitzer, J. I.; Morozov, P.; Tuschl, T. miRNAs in Human Cancer. *J. Pathol.* **2011**, *223*, 102-115.
(99) Fang, S.; Lee, H. J.; Wark, A. W.; Corn, R. M. Attomole Microarray Detection of MicroRNAs by Nanoparticle-Amplified SPR Imaging Measurements of Surface Polyadenylation Reactions J. Am. Chem. Soc. **2006**, *128*, 14044-14046.
(100) Alhasan, A. H.; Kim, D. Y.; Daniel, W. L.; Watson, E.; Meeks, J. J.; Thaxton, C. S.; Mirkin, C. A. Scanometric MicroRNA Array Profiling of Prostate Cancer Markers Using Spherical Nucleic Acid-Gold Nanoparticle Conjugates. *Anal. Chem.* **2012**, *84*, 4153-4160.
(101) Degliangeli, F.; Kshirsagar, P.; Brunetti, V.; Pompa, P. P.; Fiammengo, R. Absolute and Direct MicroRNA Quantification Using DNA-Gold Nanoparticle Probes. *J. Am. Chem. Soc.* **2014**, *136*, 2264-2267.
(102) Bostjancic, E.; Glavac, D. Importance of microRNAs in Skin Morphogenesis and Diseases. *Acta dermatovenerologica Alpina, Pannonica, Adriat.* **2008**, *17*, 95-102.

(103) Ikenaga, N.; Ohuchida, K.; Mizumoto, K.; Yu, J.; Kayashima, T.; Sakai, H.; Fujita, H.; Nakata, K.; Tanaka, M. MicroRNA-203 Expression as a New Prognostic Marker of Pancreatic Adenocarcinoma. *Ann. Surg. Oncol.* **2010**, *17*, 3120-3128.
(104) Melar-New, M.; Laimins, L. A. Human Papillomaviruses Modulate Expression of MicroRNA 203 upon Epithelial Differentiation to Control Levels of p63 Proteins. *J. Virol.* **2010**, *84*, 5212-5221.
(105) Shagin, D. A. A Novel Method for SNP Detection Using a New Duplex-Specific Nuclease From Crab Hepatopancreas. *Genome Res.* **2002**, *12*, 1935-1942.
(106) Labuda, J.; Oliveira Brett, A. M.; Evtugyn, G.; Fojta, M.; Mascini, M.; Ozsoz, M.; Palchetti, I.; Paleček, E.; Wang, J. Electrochemical Nucleic Acid-Based Biosensors: Concepts, Terms, and Methodology (IUPAC Technical Report)*. *Pure Appl. Chem* **2010**, *82*, 1161-1187.
(107) Brendel, P. J.; Luther, G. W. I. Development of a Gold Amalgam Voltammetric Microelectrode for the Determination of Dissolved Fe, Mn, O2, and S(-II) in Porewaters of Marine and Freshwater Sediments. *Environ. Sci. Technol.* **1995**, *29*, 751-761.
(108) Crooks, R. M. Concluding Remarks: Single Entity Electrochemistry One Step at a Time. *Faraday Discuss.* **2016**, *193*, 533-547.
(109) Filipe, V.; Hawe, A.; Jiskoot, W. Critical Evaluation of Nanoparticle Tracking Analysis (NTA) by NanoSight for the Measurement of Nanoparticles and Protein Aggregates. *Pharm. Res.* **2010**, *27*, 796-810.
(110) Hurst, S. J.; Lytton-Jean, A. K. R.; Mirkin, C. A. Maximizing DNA Loading on a Range of Gold Nanoparticle Sizes Anal. Chem. **2006**, *78*, 8313-8318.
(111) Evrogen. Duplex-Specific Nuclease. http://evrogen.com/protein-descriptions/UM-DSN.pdf (accessed April 6, 2017).
(112) Wang, Z.-X.; Bian, H.-B.; Wang, J.-R.; Cheng, Z.-X.; Wang, K.-M.; De, W. Prognostic Significance of Serum miRNA-21 Expression in Human Non-Small Cell Lung Cancer. *J. Surg. Oncol.* **2011**, *104*, 847-851.
(113) Gao, S.; Tian, H.; Guo, Y.; Li, Y.; Guo, Z.; Zhu, X.;

Chen, X. miRNA Oligonucleotide and Sponge for miRNA-21 Inhibition Mediated by PEI-PLL in Breast Cancer Therapy. *Acta Biomater.* **2015**, *25*, 184-193.
(114) Alemar, B.; Izetti, P.; Gregório, C.; Macedo, G. S.; Castro, M. A. A.; Osvaldt, A. B.; Matte, U.; Ashton-Prolla, P. miRNA-21 and miRNA-34a Are Potential Minimally Invasive Biomarkers for the Diagnosis of Pancreatic Ductal Adenocarcinoma. *Pancreas* **2016**, *45*, 84-92.
(115) Robinson, D. A.; Duay, J.; Kondajji, A. M.; Stevenson, K. J. Mechanistic Aspects of Hydrazine-Induced Pt Colloid Instability and Monitoring Aggregation Kinetics with Nanoparticle Impact Electroanalysis. *Faraday Discuss.* **2016**, *193*, 293-312.
(116) Chen, A.; Chatterjee, S. Nanomaterials Based Electrochemical Sensors for Biomedical Applications. *Chem. Soc. Rev.* **2013**, *42*, 5425.
(117) Gong, L.; Zhao, Z.; Lv, Y.-F.; Huan, S.-Y.; Fu, T.; Zhang, X.-B.; Shen, G.-L.; Yu, R.-Q. DNAzyme-Based Biosensors and Nanodevices. *Chem. Commun.* **2015**, *51*, 979-995.
(118) Seefeld, T. H.; Zhou, W.-J.; Corn, R. M. Rapid Microarray Detection of DNA and Proteins in Microliter Volumes with Surface Plasmon Resonance Imaging Measurements. *Langmuir* **2011**, *27*, 6534-6540.
(119) Seefeld, T. H.; Halpern, A. R.; Corn, R. M. On-Chip Synthesis of Protein Microarrays from DNA Microarrays via Coupled *In Vitro* Transcription and Translation for Surface Plasmon Resonance Imaging Biosensor Applications. *J. Am. Chem. Soc.* **2012**, *134*, 12358-12361.
(120) Chen, Y.; Corn, R. M. DNAzyme Footprinting: Detecting Protein-Aptamer Complexation on Surfaces by Blocking DNAzyme Cleavage Activity. *J. Am. Chem. Soc.* **2013**, *135*, 2072-2075.
(121) Decher, G. Fuzzy Nanoassemblies: Toward Layered Polymeric Multicomposites. *Science* **1997**, *277*, 1232-1237.
(122) Hammond, P. T. Form and Function in Multilayer Assembly: New Applications at the Nanoscale. *Adv. Mater.* **2004**, *16*, 1271-1293.
(123) Chazalviel, J.-N.; Allongue, P. On the Origin of the

Efficient Nanoparticle Mediated Electron Transfer across a Self-Assembled Monolayer. *J. Am. Chem. Soc.* **2011**, *133*, 762-764.
(124) Zhao, J.; Bradbury, C. R.; Fermín, D. J.Long-Range Electronic Communication between Metal Nanoparticles and Electrode Surfaces Separated by Polyelectrolyte Multilayer Films *J. Phys. Chem. C* **2008**, *112*, 6832-6841.
(125) Liu, F.; Khan, K.; Liang, J.-H.; Yan, J.-W.; Wu, D.-Y.; Mao, B.-W.; Jensen, P. S.; Zhang, J.; Ulstrup, J. On the Hopping Efficiency of Nanoparticles in the Electron Transfer across Self-Assembled Monolayers. *ChemPhysChem* **2013**, *14*, 952-957.
(126) Dyne, J.; Lin, Y.-S.; Lai, L. M. H.; Ginges, J. Z.; Luais, E.; Peterson, J. R.; Goon, I. Y.; Amal, R.; Gooding, J. J. Some More Observations on the Unique Electrochemical Properties of Electrode-Monolayer-Nanoparticle Constructs. *ChemPhysChem* **2010**, *11*, 2807-2813.
(127) Barfidokht, A.; Ciampi, S.; Luais, E.; Darwish, N.; Gooding, J. J. Distance-Dependent Electron Transfer at Passivated Electrodes Decorated by Gold Nanoparticles. *Anal. Chem.* **2013**, *85*, 1073-1080.
(128) Su, L.; Gao, F.; Mao, L.Electrochemical Properties of Carbon Nanotube (CNT) Film Electrodes Prepared by Controllable Adsorption of CNTs onto an Alkanethiol Monolayer Self-Assembled on Gold Electrodes *Anal. Chem.* **2006**, *78*, 2651- 2657.
(129) Kissling, G. P.; Bünzli, C.; Fermín, D. J. Tuning Electrochemical Rectification via Quantum Dot Assemblies. *J. Am. Chem. Soc.* **2010**, *132*, 16855-16861.
(130) Zhang, B.; Fan, L.; Zhong, H.; Liu, Y.; Chen, S. Graphene Nanoelectrodes: Fabrication and Size-Dependent Electrochemistry. *J. Am. Chem. Soc.* **2013**, *135*, 10073-10080.
(131) Ferriz-Mañas, M.; Schlenoff, J. B. Zeta Potential of Polyelectrolyte Multilayers Using the Spinning Disk Method. *Langmuir* **2014**, *30*, 8776-8783.
(132) Smalley, J. F.; Chalfant, K.; Feldberg, S. W.; Nahir, T. M.; Bowden, E. F.An Indirect Laser-Induced Temperature Jump Determination of the Surface pKa of

11-Mercaptoundecanoic Acid Monolayers Self-Assembled on Gold *J. Phys. Chem. B* **1999**, *103*, 1676- 1685.
(133) Finklea, H. O.; Hanshew, D. D. Electron-Transfer Kinetics in Organized Thiol Monolayers with Attached Pentaammine(pyridine)ruthenium Redox Centers. *J. Am. Chem. Soc.* **1992**, *114*, 3173-3181.
(134) Sheffer, M.; Vivier, V.; Mandler, D.Self-assembled monolayers on Au microelectrodes *Electrochem. Commun.* **2007**, *9*, 2827- 2832.
(135) Bain, C. D.; Troughton, E. B.; Tao, Y. T.; Evall, J.; Whitesides, G. M.; Nuzzo, R. G. Formation of Monolayer Films by the Spontaneous Assembly of Organic Thiols from Solution onto Gold. *J. Am. Chem. Soc.* **1989**, *111*, 321-335.
(136) Smith, E. L.; Alves, C. A.; Anderegg, J. W.; Porter, M. D.; Siperko, L. M. Deposition of Metal Overlayers at End-Group-Functionalized Thiolate Monolayers Adsorbed at Gold. 1. Surface and Interfacial Chemical Characterization of Deposited Copper Overlayers at Carboxylic Acid-Terminated Structures. *Langmuir* **1992**, *8*, 2707-2714.
(137) Balevicius, Z.; Ramanaviciene, A.; Baleviciute, I.; Makaraviciute, A.; Mikoliunaite, L.; Ramanavicius, A. Evaluation of Intact- and Fragmented-Antibody Based Immunosensors by Total Internal Reflection Ellipsometry. *Sensors Actuators B* **2011**, *160*, 555-562.
(138) Zhong, C.-J.; Porter, M. D. Fine Structure in the Voltammetric Desorption Curves of Alkanethiolate Monolayers Chemisorbed at Gold. *J. Electroanal. Chem.* **1997**, *425*, 147-153.
(139) Lovrić, M.; Komorsky-Lovrić, Š.; Murray, R. W. Adsorption Effects in Square-Wave Voltammetry of Totally Irreversible Redox Reactions. *Electrochim. Acta* **1988**, *33*, 739-744.
(140) Aoki, K.; Kakiuchi, T. Probability Theory of Desorption Kinetics of Self-Assembled Alkanethiols Stabilized with Pair Interaction. *J. Electroanal. Chem.* **1998**, *452*, 187-192.
(141) Vinokurov, I. A.; Morin, M.; Kankare, J.Mechanism of Reductive Desorption of Self-Assembled Monolayers on the Basis of Avrami Theorem and Diffusion *J. Phys.*

Chem. B **2000**, *104*, 5790- 5796.
(142) Balasubramanian, S.; Revzin, A.; Simonian, A. Electrochemical Desorption of Proteins from Gold Electrode Surface. *Electroanalysis* **2006**, *18*, 1885-1892.
(143) Widrig, C. A.; Alves, C. A.; Porter, M. D. Scanning Tunneling Microscopy of Ethanethiolate and N-Octadecanethiolate Monolayers Spontaneously Absorbed at Gold Surfaces. *J. Am. Chem. Soc.* **1991**, *113*, 2805-2810.
(144) Farhat, T. R.; Schlenoff, J. B.Doping-Controlled Ion Diffusion in Polyelectrolyte Multilayers: Mass Transport in Reluctant Exchangers *J. Am. Chem. Soc.* **2003**, *125*, 4627- 4636.
(145) Ghostine, R. A.; Markarian, M. Z.; Schlenoff, J. B. Asymmetric Growth in Polyelectrolyte Multilayers. *J. Am. Chem. Soc.* **2013**, *135*, 7636-7646.
(146) Schlenoff, J. B.; Ly, H.; Li, M.Charge and Mass Balance in Polyelectrolyte Multilayers *J. Am. Chem. Soc.* **1998**, *120*, 7626- 7634.
(147) Harris, J. J.; Bruening, M. L.Electrochemical and in Situ Ellipsometric Investigation of the Permeability and Stability of Layered Polyelectrolyte Films *Langmuir* **2000**, *16*, 2006- 2013.
(148) Cheng, Y.; Corn, R. M.Ultrathin Polypeptide Multilayer Films for the Fabrication of Model Liquid/Liquid Electrochemical Interfaces *J. Phys. Chem. B* **1999**, *103*, 8726- 8731.
(149) Shein, J. B.; Lai, L. M. H.; Eggers, P. K.; Paddon-Row, M. N.; Gooding, J. J. Formation of Efficient Electron Transfer Pathways by Adsorbing Gold Nanoparticles to Self-Assembled Monolayer Modified Electrodes. *Langmuir* **2009**, *25*, 11121-11128.
(150) Chirea, M.; García-Morales, V.; Manzanares, J. A.; Pereira, C.; Gulaboski, R.; Silva, F.Electrochemical Characterization of Polyelectrolyte/Gold Nanoparticle Multilayers Self-Assembled on Gold Electrodes *J. Phys. Chem. B* **2005**, *109*, 21808- 21817.
(151) Bethell, D.; Brust, M.; Schiffrin, D. J.; Kiely, C. From Monolayers to Nanostructured Materials: An Organic Chemist's View of Self-Assembly. *J. Electroanal. Chem.* **1996**, *409*, 137-143.
(152) Lu, M.; Li, X. H.; Yu, B. Z.; Li, H. L.

Electrochemical Behavior of Au Colloidal Electrode through Layer-by-Layer Self-Assembly. *J. Colloid Interface Sci.* **2002**, *248*, 376-382.
(153) Chirea, M.; Pereira, C. M.; Silva, F.Catalytic Effect of Gold Nanoparticles Self-Assembled in Multilayered Polyelectrolyte Films *J. Phys. Chem. C* **2007**, *111*, 9255-9266.
(154) Santos, H. A.; Chirea, M.; García-Morales, V.; Silva, F.; Manzanares, J. A.; Kontturi, K.Electrochemical Study of Interfacial Composite Nanostructures: Polyelectrolyte/Gold Nanoparticle Multilayers Assembled on Phospholipid/Dextran Sulfate Monolayers at a Liquid-Liquid Interface *J. Phys. Chem. B* **2005**, *109*, 20105-20114.
(155) Dowdy, C. E.; Leopold, M. C. Enhanced Electrochemistry of Nanoparticle-Embedded Polyelectrolyte Films: Interfacial Electronic Coupling and Distance Dependence. *Thin Solid Films* **2010**, *519*, 790-796.
(156) Cortez, M. L.; Marmisollé, W.; Pallarola, D.; Pietrasanta, L. I.; Murgida, D. H.; Ceolín, M.; Azzaroni, O.; Battaglini, F. Effect of Gold Nanoparticles on the Structure and Electron-Transfer Characteristics of Glucose Oxidase Redox Polyelectrolyte-Surfactant Complexes. *Chem. - A Eur. J.* **2014**, *20*, 13366-13374.
(157) Schmidt, A. R.; Nguyen, N. D. T.; Leopold, M. C. Nanoparticle Film Assemblies as Platforms for Electrochemical Biosensing——Factors Affecting the Amperometric Signal Enhancement of Hydrogen Peroxide. *Langmuir* **2013**, *29*, 4574-4583.
(158) Ou, C.; Yuan, R.; Chai, Y.; Tang, M.; Chai, R.; He, X. A Novel Amperometric Immunosensor Based on Layer-by-Layer Assembly of Gold Nanoparticles-multi-Walled Carbon Nanotubes-Thionine Multilayer Films on Polyelectrolyte Surface. *Anal. Chim. Acta* **2007**, *603*, 205-213.